UNIVERSITA' DEGLI STUDI DI BOLOGNA

Facoltà di Ingegneria

Dottorato di Ricerca in
Ingegneria Elettronica, Informatica e
delle Telecomunicazioni

XIX CICLO

SSD: ING-INF/02 CAMPI ELETTROMAGNETICI

Microlaser in Rare Earths Doped Glasses

Dottorando: Simone Berneschi

Relatore: Coordinatore:

Prof. Ing. Paolo Bassi   Prof. Ing. Paolo Bassi

Correlatori:

Prof. Giancarlo Righini

Dr.Gualtiero Nunzi Conti

Anno Accademico 2005-2006

A Claudia

CONTENTS

INTRODUCTION

1. Integrated Optics for Telecommunications

Optical technologies have become more and more important in the present information era as they provide adequate answers to the ever increasing demand for high speed internet access and broadband communication services, necessary for both long distance communications and Metropolitan or Local Area Networks (MAN and LAN, respectively). In chronologic order, three were the key steps that contributed to the realization and development of optical communication systems [1] (see Fig. I): (i) the discovery of the laser, at the beginning of the 60s, as coherent source of optical signal; (ii) the fabrication, between the end of the 70s and beginning of 80s, of highly transparent single mode silica fibers with attenuation of 0.2÷0.3 dB/km in a wide range of wavelengths between 1450 nm and 1650 nm ($\approx$ 25 THz); (iii) the possibility to have, from the middle of the 80s, all-optical signal amplification, in order to regenerate light signals without any double opto-electronic conversion. This latter result was obtained doping silica fibers with erbium, a particular element of Rare-Earth (RE) group, having its optical emission wavelength accordable between the 1530 nm and 1570 nm, just inside the low-loss window of silica fiber (Erbium Doped Fiber Amplifier, EDFA) [2-3]. The idea which generated this innovative device was in effect not truly new as the possibility of using RE doped glass materials to produce laser emission was studied many years before (1961) by Snitzer [4].
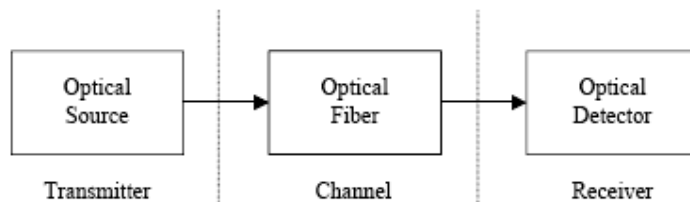
Fig. I: Scheme of an Optical Communication System [5].

These breakthroughs have generated and continue to push intensive research for new, more compact and reliable optical components and devices, able to respond both at the continuous demand of larger bandwidth and at the higher complexity of the net. This is

particularly true in the domain conventionally known as "Integrated Optics" (IO), which aims to integrate several functions in a single optical chip through guiding structures based on channel waveguides, with high performance and reduced costs. Typical examples of IO devices are passive devices, such as splitters and couplers, able to route the optical signal and guarantee a higher number of access points to the optical network, but also active ones, such as waveguide amplifiers (Erbium Doped Waveguide Amplifiers, EDWAs) for all-optic regeneration of signal in DWDM (Dense Wavelength Division Multiplexing) applications. The wish to reduce costs guaranteeing high performances and mass production has in fact made glass an interesting host material to fabricate RE doped IO devices [4, 6-7].

2. RE-doped materials and sources for integrated and micro optics

As mentioned before glasses have been known since long time as a convenient host for RE ions to be used for the fabrication of solid-state lasers, especially of those based on Er^{3+} ion doping [8,9]. We also pointed out that guided wave planar format adds several advantages, such as compact size, possibility of working with higher pump density and lower lasing threshold, and a larger flexibility in design and fabrication. However, the choice of the active glass matrix appears a crucial step for the performance of integrated optical amplifiers and lasers, because the short length of these devices generally imposes higher RE concentrations than in fiber amplifiers. This fact gives rise to deleterious non-radiative processes which worsen the device performances. Co-doping with Yb^{3+} (ytterbium) ions is generally used to improve the pump absorption but also to partially reduce these parasitic effects [9,10]. In any case, an optimization of the dopant-matrix system is necessary. Silicate glasses remain very attractive materials for the development of IO devices, due to their chemical durability and adaptability to different waveguide fabrication processes. Nevertheless, the fabrication of optical amplifiers and lasers in these glasses may be limited by the reduced solubility of rare-earth ions and the relative narrower fluorescence bandwidth as compared to other oxide-glass hosts largely used as active materials, like phosphate glasses [10,11]. The ability to fabricate channel waveguide with low insertion losses is a fundamental requisite to the final performance of the device. In this sense, the choice of silicate glasses appears quite good because the refractive index is close to that of telecommunication silica fiber. Various technologies

have been proposed to fabricate active glass IO components. They include ion-exchange [12,13], sol-gel [14-15], sputtering [16,17], UV writing or photo-imprinting [18,P.II], femtosecond laser writing [19,20], ion-implantation [20,21]. The choice of the best method is still not obvious and depends also on the application one has in mind. So, the first part of this thesis work will concern the investigation of new glass materials able to hosts high RE concentrations, with particular attention to their spectroscopic characterization, and the development of the most convenient fabrication process for the integration of channel waveguides in these glasses.

Then, more recently, micro-optical devices microcavities or resonators able to confine light in small volumes have gained growing interest not only as a basic research topic but also in view of new interesting applications in sensing and photonics [23]. In particular, in dielectric microspheres light can be guided through whispering-gallery-modes (WGMs) with a strong temporal and spatial confinement [24]. These features allow the implementation of very low threshold, small size, high performance narrowband laser microsources in active glasses, without any structure (mirrors or gratings) to feedback the amplified signal [25]. This suggested to extend the investigation on Er^{3+} doped glass to include also the study of possible developments of these new devices with particular reference to the implementation of the fiber-resonator coupling system and the development of microlaser sources based on Er^{3+} doped glass microspheres.

3. Outline of the Thesis

This thesis is organized as follows.

In Chapter 1 the basic formalism to describe laser behavior will be recalled.

In Chapter 2 Rare-Earths doped glasses as active materials for laser devices will be described. The fundamentals of Rare-Earths theory in amorphous materials will be presented with particular attention to the Er^{3+} ion for its interesting applications in optical communication. The pump mechanism in a Er^{3+} system and the effect of a Yb^{3+} co-doping on the pump efficiency will also be presented. Spectroscopic characterization

of different experimental silicate and commercial phosphate glasses [P.II-VIII], used in our experiments to fabricate laser devices, will close this chapter.

In Chapter 3, after a brief overview on modeling of electromagnetic propagation in planar guiding structures, preliminary results on the development of new channel waveguide laser will be presented. These waveguides are fabricated using: i) ion-exchange process in experimental Er^{3+}/Yb^{3+} silicate glasses [P.IV-V,P.VII,P.IX]; ii) UV photo-imprinting technique in SiO_2-GeO_2 binary system activated by Er^{3+}/Yb^{3+} ions [P.II-III]; iii) ion beam irradiation in Er^{3+}-doped tungsten-tellurite glasses [P.I].

In Chapter 4 we will present an analytical model for electromagnetic propagation in dielectric spherical resonators (DSRs), based on the resolution of Maxwell equations by means of vector and Debye's scalar potentials. Numerical simulations, developed in MATLAB code, will be also performed. Fabrication and characterization of microsphere lasers in different modified silica glasses and phosphate glasses will be discussed and results on lasing action and resonances will be reported and discussed as well [P.VI, P.VIII].

The experimental work presented in this thesis was mainly done at the Institute of Applied Physics "Nello Carrara" I.F.A.C.-C.N.R., Sesto Fiorentino (Florence, Italy), also in the framework of the FIRB project "Sistemi Miniaturizzati per Elettronica e Fotonica".

CHAPTER 1 *The Laser: Principles and Typologies*

1.1 Introduction

The word *LASER* is the acronym of "*Light Amplification by Stimulated Emission of Radiation*". A laser is an optical device able to produce an high-intensity and directional beam that typically has a well-defined wavelength. In 1960 T. H. Maiman demonstrated the first realization of a solid state laser (ruby laser) [26] extending, to the optical frequencies, the principle of *MASER* (*Microwave Amplification by Stimulated Emission of Radiation*) obtained six years before by C. H. Townes [27] and, independently, by N. G. Bosov and A. M. Prokhorov [28]. However, seminal ideas on lasers were proposed in 1915 when Albert Einstein, in his work on emission and absorption of light by atoms and molecules [29], introduced for the first time the concept of *stimulated emission* that has a fundamental importance for laser working After showing that the state of thermodynamic equilibrium between radiation and matter could be explained in terms of three basic processes: spontaneous and stimulated emissions and absorption.

A detailed description on the laser working principles, structure and materials can be found in many textbooks [30-34] and is beyond the scope of this thesis. In this chapter the basic principles of laser theory will then be reminded simply to introduce the formalism and the symbols used in the next chapters. As attention will be focused on lasers realized using Rare Earths doped glasses, only the so called three level systems will be illustrated.

1.2 The three level laser equations

A schematic of the so called three level laser system [35] is shown in Fig. 1.1.
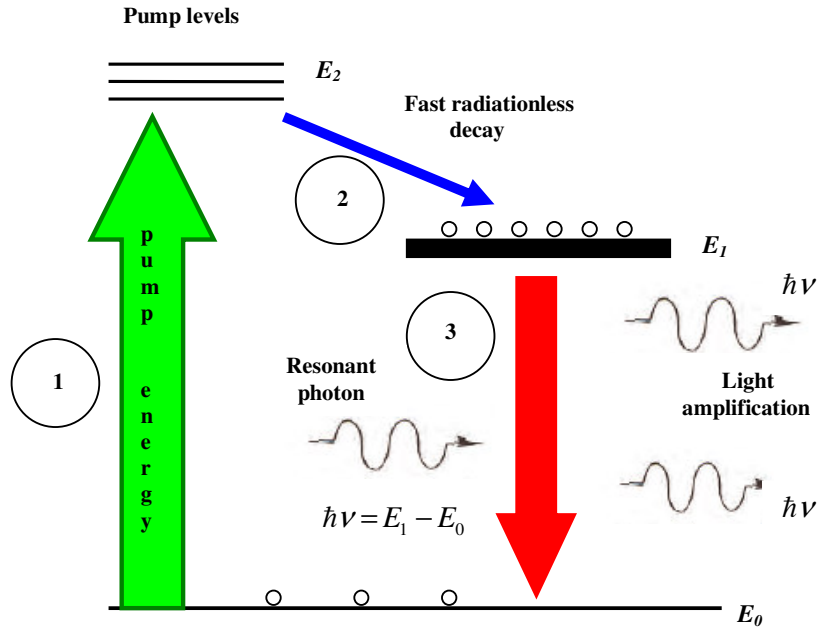
Fig. 1.1: Three-level Laser scheme

Electrons at the lower energy level E_0 may absorb, with some probability, the so called pump energy (carried, for the lasers we are considering, by another photon) and are excited to an upper energy level, E_2. This level is unstable and then the electron rapidly decays (decay time in the order of 1 ms in silicate glasses), emitting the corresponding radiation in mechanical form (phonon, or mechanical vibration), to another energy level, E_1, which is said metastable as its decay time is not so short (decay time in the order of around 10 ms in silicate glasses).

If the upper pump level is empty, the rate at which the upper laser level 2 becomes populated by pumping is given by

$$\frac{d N_0}{d t}\bigg|_{pump,abs} = -W_p N_0 = -\frac{d N_2}{d t}\bigg|_{pump,abs} \tag{1.1}$$

where N_i ($i = 0,2$) is the number of atoms (per unit of volume) at energy level E_i and W_p is a coefficient called *pump rate* [30]. W_p is basically the *pump absorption probability* and can then be expressed as:

$$W_p = \sigma_p \, F_p = \sigma_p \, \frac{I_p}{\hbar \nu_p}, \qquad with \;\; \hbar \nu_p = E_2 - E_0 \qquad (1.2)$$

where $F = I_p / \hbar \nu_p$ is the photon flux of the optical pump, with light intensity I_p, and σ_p is the *pump absorption cross section*. Dimensionally it is an area and depends only on the characteristics of the considered transition.

When a further photon arrives, with energy

$$\hbar \nu = E_1 - E_0 \qquad (1.3)$$

($\hbar = 6.63 \cdot 10^{-34} \, [J \cdot s]$ is the Plank's constant), it may stimulate the decay of the electron from the excited level E_1 to the ground level E_0. Such a decay occurs with a finite probability and corresponds to the emission of another photon with the same ν of the incident one. The generated secondary photon has not only the same energy but is also in phase with the principal one: a *coherent* emission is then obtained. The radiation process can be described by an equation similar to (1.1) [30,36]:

$$\left. \frac{d N_1}{d t} \right|_{st} = - W_{10} \, N_1 = - \left. \frac{d N_0}{d t} \right|_{st} \qquad (1.4)$$

where W_{10} is called *stimulated emission probability*. It depends not only on the particular transition but also on the intensity of the incident electromagnetic wave. As in eq.(1.2), also for the stimulated emission probability we can write:

$$W_{10} = \sigma_{10} \; F = \sigma_e \frac{I_s}{\hbar \nu} \tag{1.5}$$

where F is the photon flux of the incident wave (the signal) and $\sigma_{10} = \sigma_e$ is a quantity having the dimension of area (called *stimulated emission cross section*) depending only on the characteristics of the considered transition.

Note that the decay can may also occur in a non-radiative way. In this case the energy difference $E_1 - E_0$ is released to the material in the form of thermal energy through a multiphonon deactivation (see Chapter 2).

Together with the phenomena mentioned above, another physical process can occur.

It is the *spontaneous emission* in which an electron, in the metastable level E_1, spontaneously falls down to the ground level E_0 and emits a photon with a frequency given by eq. (1.3). The probability of spontaneous emission can be so expressed [30,36]:

$$\left. \frac{d N_1}{d t} \right|_{sp} = - A N_1 = - \left. \frac{d N_0}{d t} \right|_{sp} \tag{1.6}$$

where A is *spontaneous emission probability* or *Einstein A coefficient.*

This term contributes to the noise in a optical amplifying or lasing system.

Consequently, in order to make the stimulated emission process efficient, the so called *population inversion condition* should be satisfied:

$$N_1 - N_0 > 0 \tag{1.7}$$

In a three level system, the pump mechanism illustrated above guarantees this condition. The foregoing equations allow to determine a fundamental parameter of any laser, its so called **optical gain G**. This parameter depends on the material, the pump mode and varies also on the operating wavelength and the device geometrical features. To obtain its expression one must consider first the *gain per pass* in the active material, defined as

the ratio between the output and the input photon flux F of the signal to be amplyfied, which can be obtained solving the following differential equation [30]:

$$d F = \sigma F \left(N_1 - N_0 \right) d z \tag{1.8}$$

where σ is the emission cross section introduced in (1.3), and N_1 and N_0 are the two populations of to the upper and the lower laser levels. Solving eq. (1.8) one gets the explicit expression of the **gain** of the active medium:

$$G = \exp \left[\left(N_1 - N_0 \right) \sigma(v) L \right] = \exp \left(g L \right) \tag{1.9}$$

where L is the length of the active material and g is the gain coefficient.

To obtain a laser, a feedback is needed [30,36]. To do so a resonant cavity can be created putting the active material between two highly reflecting mirrors (plane-parallel mirror surfaces, for the so called Fabry Perot lasers, or Bragg gratings, for DFB and DBR lasers, as sketched in Fig. 1.2). Lasing can occur if the so called *threshold condition* is fulfilled [37]. This means that the optical gain G of the active material must at least compensate the absorption and transmission losses in the system.
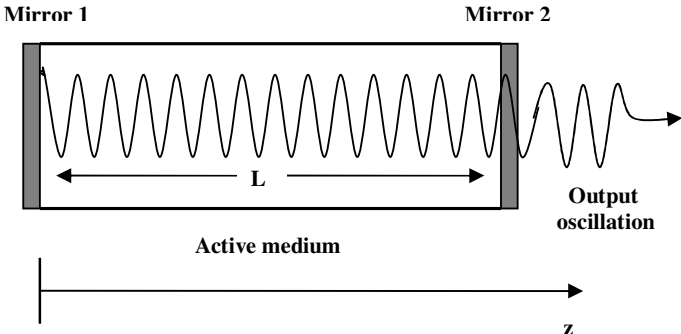
Fig. 1.2: Generic scheme of a Laser

In the reference frame shown in Fig. 1.2, such a condition can be written as:

$$\vec{E}_0 \exp\left[2(N_1 - N_0)\sigma(v)L\right]\exp\left(-2\alpha_{int}L\right)R_1 R_2 \exp\left(-j\,4\pi n L/\lambda\right) = \vec{E}_0 \qquad (1.10)$$

where

- $\vec{E}_0$ is the electric field valued in $z = 0^+$;

- $\exp\left[(N_1 - N_0)\sigma(v)L\right]$ is the amplification factor through the active medium given by eq.(1.20);

- $\exp(-\alpha_{int}L)$ is the attenuation factor due to the absorption of the material, where α_{int} is the internal absorption coefficient per unit length;

- R_1 and R_2 are the mirrors reflectivity coefficients for $z = 0$ and $z = L$, respectively;

- $\exp(-j\,4\pi nL/\lambda)$ is the difference in phase, for the electric field $\vec{E}_0$, after the second reflection on the first mirror.

Considering the amplitude contribution of the equation reported above, we can write the condition [30]:

$$\left(N_1 - N_0\right)_c = \frac{1}{2\sigma}\left[\alpha_{int} + \frac{1}{L}\ln\left(\frac{1}{R_1 R_2}\right)\right] \qquad . \qquad (1.11)$$

This relationship shows that the threshold corresponds to a particular value of the population inversion: $(N_1 - N_0)_c$. Once this *critical inversion* is achieved, the photons that are spontaneously emitted along the cavity start the amplification process and, consequently, the oscillation occurs. This is the basis of a laser oscillator. To get a threshold condition, the pump rate defined in eq. (1.2) must reach a critical value W_{cp}. Finally, remembering that $G = \exp(g\,L)$, eq. (1.10) can be rewritten as:

$$\vec{E}_0\, R_1 \exp\left(g\,L\right)\exp\left(-\alpha_{\text{int}}\, L\right)R_2 \exp\left(g\,L\right)\exp\left(-\alpha_{\text{int}}\, L\right)\exp\left(-\,j\,4\,\pi\,n\,L/\lambda\right)=\vec{E}_0 \,. \tag{1.12}$$

Considering once again the amplitude and phase contributions of this equation, we finally get [36]:

$$g = \alpha_{\text{int}} + \frac{1}{2\,L}\ln\!\left(\frac{1}{R_1\,R_2}\right) \tag{1.13}$$

Eq. (1.13) shows that the gain coefficient **g**, at the threshold condition, must be equal to the sum of internal (i.e., absorption of material) and external (i.e., transmission of cavity) losses.

The presence of a resonant cavity introduces a new concept, the so called *Free Spectral Range* (FSR), defined as [1]:

$$\Delta\nu = FSR = \nu_{m+1} - \nu_m = \frac{m+1}{2\,L\,n_{m+1}}c - \frac{m}{2\,L\,n_m}c \tag{1.14}$$

where m is an arbitrary integer and n_m is the effective refractive index of the m-th frequency resonating in the active medium. Only frequencies associated to cavity gains exceeding the losses at the same frequency will be present in the radiation spectrum of the laser. This allows to introduce also the Quality Factor Q of the cavity defined, generally, as

$$Q = \frac{2\,\pi\,\left(Energy\ Stored\right)}{Energy\ loss/cycle} = \frac{\nu}{d\nu} = \omega\,\tau \tag{1.15}$$

where τ is the photon lifetime in the cavity.

1.3 Studied Laser structures

In the following, attention will be focused on two types of optical resonators realized in such substrated: Fabry-Perot waveguides (Chapter 3) and microspherical cavities (Chapter 4) .

In the case of a Fabry-Perot resonator, the feedback is guaranteed by two high reflecting mirrors (or gratings) as sketched in Fig.1.2.

For the spherical resonators, the feedback at selected wavelengths is obtained taking advantage of the particular geometry of the structure that acts as a ring and confines the light in proximity of the spherical surface. This is the case of morphology-dependent resonances (also called **W**hispering **G**allery **M**odes, **WGM**s), shown in Fig.1.3:
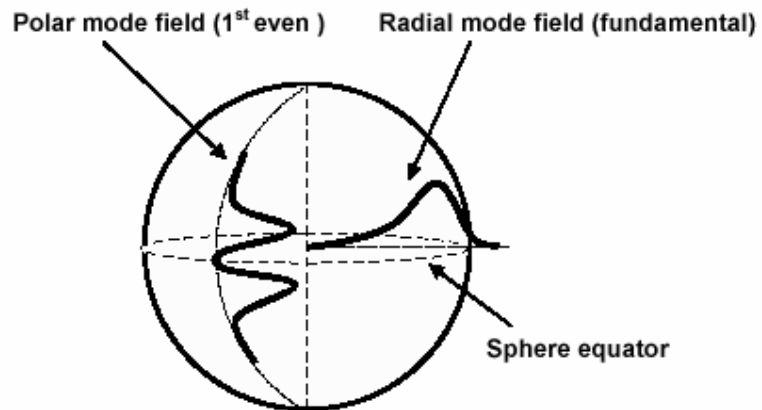
Fig. 1.3: Schematic of WGM field components in a microsphere resonator. Light trapped in the WGM propagates around the sphere equator in a narrow and thin band, constantly reflecting off the sphere surface.

CHAPTER 2 *Materials: Rare-Earth-doped glasses for microlasers*

In this chapter we discuss about the two elements constituting a laser device: the active medium and the pump mechanism. As mentioned above, in Integrated Optics different materials can be used as active medium for laser devices (i.e. semiconductor or dielectric materials). In optical amplification and laser operation, glasses activated by Rare-Earth ions are one of the most convenient choice in virtue of their high performances and low costs. In particular, among all the Rare-Earth elements, erbium (alone or together with ytterbium) has a relevant importance in telecommunication systems because its emission peak at 1.5 μm falls just inside the low-loss third window (also called C-band) of silica optical fiber as shown in Fig. 2.1.

(a)   (b)
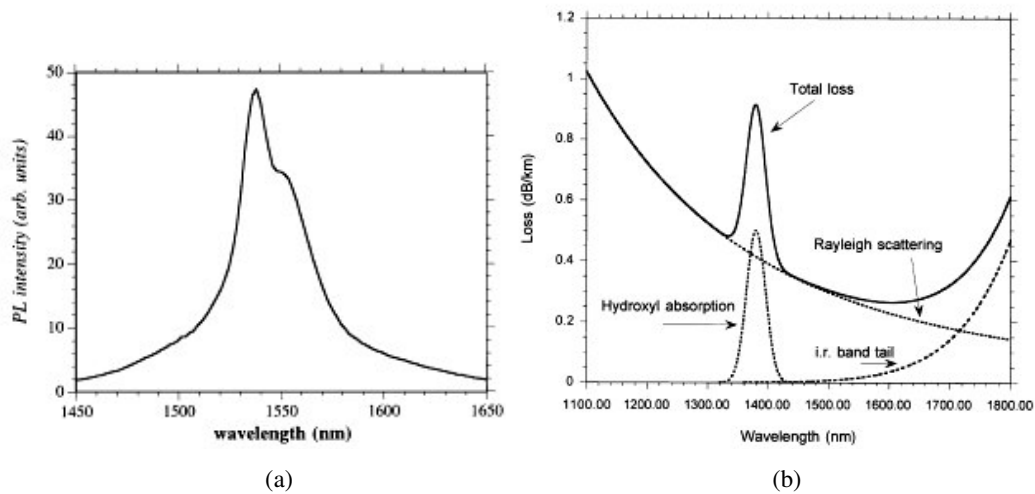
Fig. 2.1: (a) The photoluminescence spectrum of the $^4I_{13/2} \rightarrow {}^4I_{15/2}$ Er^{3+} transition in silica host (around 1.5 μm) falls inside the low-loss window of silica optical fibre near IR (InfraRed) region (b) [1].

Among the key parameters acting on the efficiency of lasers and amplifiers, the host glass composition plays a crucial role [2,11]. Even if phosphate glasses are recognized as an excellent host for erbium ions thanks to their possibility to guarantee higher dopant concentrations and weaker interactions among the same ions [38], silicate glasses still remain one of the more suitable host because of its chemical resistance and

compatibility with optical fiber. In addition to their high transparency around 1.5 μm, the long lifetime of the Er^{3+} $^4I_{13/2}$ metastable level permits to reach the high-population inversion needed to obtain a quite high gain [39]. In this chapter, we will examine optical and spectroscopic properties of six glass formulations: two classes of experimental soda-lime silicate glasses for the fabrication of waveguide lasers and amplifiers through ion-exchange process [P.IV-V,P.VII]; a SiO_2-GeO_2 thin glass film deposited by sputtering technique for the fabrication of waveguide lasers by UV photo-imprinting [P.II-III]; and a modified silicate Baccarat, commercial IOG10 Schott silicate glass and IOG2 Schott phosphate glass- used to obtain lasing action in optical microsphere [P.VI, P.VIII]. All these oxide-glasses are doped with different percentages of Er^{3+} and/or co-doped with Yb^{3+}.

The chapter is structured in two parts, A and B.

The first one is a theoretical part in which we report the fundamentals of Rare-Earth spectroscopy in vitreous materials and define the parameters useful for the spectroscopic characterization we performed. In Section 2.A.1 the electronic and optical properties of Rare Earth ions will be presented. In Section 2.A.2 we report on the effect of the glass matrix on the Rare-Earth ion properties while the Rate Equations model for a three-levels system concludes this theoretical part (Section 2.A.3).

In the second part, we will report on the spectroscopic characterization of active silicate and phosphate glasses used in this work. Their composition and fabrication process are described in Section 2.B.1. Absorption (Section 2.B.2), fluorescence (Section 2.B.3) and lifetime (Section 2.B.4) measurement set-ups and results are reported in the following sections. Finally, in Section 2.B.5, we will present preliminary results on the effect that the microspheres fabrication process has on the spectroscopic characteristics of the doped microcavity [P.VI].

2A Spectroscopic Properties of Rare-Earth elements: Fundamentals

2A.1 *Electronic configuration and optical properties for a Free-Rare-Earth ion*

The Rare-Earth (RE) ions, also called lanthanides, are a set of 15 elements that, occupying the sixth row of the periodic table, range from lanthanum (La), with an atomic number of 57, to lutetium (Lu), with an atomic number of 71. All the RE atoms are characterized by the same outer-shell electronic structure of $5s^2\ 5p^6\ 6s^2$. Table 2.1 lists the RE elements with their atomic numbers and electronic configurations in which [Xe] designates the configuration of Xenon [35,40].

Lanthanum	La [57]	[Xe] (6s2 5d)
Cerium	Ce [58]	[Xe] (6s2 4f 5d)
Praseodymium	Pr [59]	[Xe] (6s2 4f3)
Neodymium	Nd [60]	[Xe] (6s2 4f4)
Promethium	Pr [61]	[Xe] (6s2 4f5)
Samarium	Sm [62]	[Xe] (6s2 4f 5d)
Europium	Eu [63]	[Xe] (6s2 4f 5d)
Gadolinium	Gd [64]	[Xe] (6s2 4f7 5d)
Terbium	Tb [65]	[Xe] (6s2 4f9)
Dysprosium	Dy [66]	[Xe] (6s2 4f10)
Holmium	Ho [67]	[Xe] (6s2 4f11)
Erbium	**Er [68]**	**[Xe] (6s2 4f12)**
Thulium	Tm [69]	[Xe] (6s2 4f13)
Ytterbium	**Yb [70]**	**[Xe] (6s2 4f14)**
Lutetium	Lu [71]	[Xe] (6s2 4f14 5d)

Table 2.1 : RE elements with their atomic numbers and electronic configurations. [Xe] stands for the electronic configuration of Xenon.

The most stable ionization state for a rare-earth element is the trivalent one (i.e. Er^{3+}, Yb^{3+}, etc.). In this configuration, two of the $6s$ electrons and one of the $4f$ electrons are removed, but the outer $5s$ and $5p$ electrons remain untouched, shielding the other $4f$ electrons from the effect of external fields, such as those generated by the surrounding environment. The number of electrons occupying the inner $4f$ shell confers the spectroscopic properties to each element while optical absorption and emission

processes cause transitions within this level. In the choice of which RE element is better to use for amplification and laser applications, the strength and energy of emission/absorption processes play an important role. In particular the knowledge of absorption spectrum gives a important information on the pump wavelength necessary to excite the ions to higher energy levels. From these high levels, electrons relax to the ground level through different steps in which light radiation may or may not occur, with the modalities illustrated in Chapter 1. The energy levels of $4f$ electrons can be expressed starting from the Hamiltonian for a N-electron ion, written in the absence of external fields [41]:

$$H_{Free-Ion} = -\sum_{i=1}^{N} \frac{\hbar^2}{2m} \nabla_i^2 - \sum_{i=1}^{N} \frac{Ze^2}{r_i} + \sum_{i<j}^{N} \frac{e^2}{r_{ij}} + \sum_{i=1}^{N} \xi(r_i)\, l_i \cdot s_i = H_O + H_{el} + H_{S-O} \qquad (2.1)$$

In eq. (2.1) the first two terms represent the kinetic and potential energy of the N-electrons in the field of the nucleus, respectively. Z is the effective charge, m is the mass of the electron and r_i is the distance of i-th electron from nucleus. The third term, labelled H_{el}, takes in account the Coulomb interaction among $4f$ electrons pairs at a distance r_{ij}. The last term, H_{S-O}, is the spin-orbit interaction, where the constant $\xi(r_i)$ represents the spin-orbit coupling coefficient, and s_i and l_i are the angular and the orbital momentum of the i-th electron, respectively. If $H_{el} \gg H_{S-O}$, the energy level of each ion can be labelled using the Russell-Sounders notation $^{2S+1}L_J$, where S is the total spin quantum number, L is the orbital angular momentum quantum number, that can assume the values L= 0, 1, 2, 3, 4, 5, 6….corresponding to the letters S, P, D, F, G, H, I….., J is the total angular momentum quantum number, with J = L + S and, finally, 2J+1 is the degeneration of the level. The energy level diagrams for the Er^{3+} ion is shown in Fig. 2.2 .
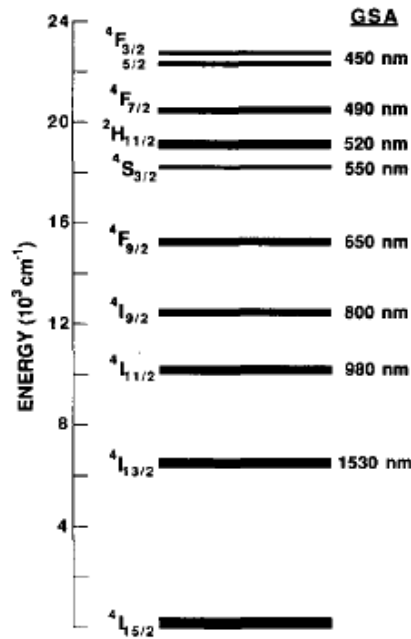
Fig. 2.2: Energy levels of Er^{3+} labelled with the dominant Russel-Saunders ^SL_J. For each state the ground state absorption transition GSA is also reported [2].

2A.2 Glass as host for RE ions: Judd-Ofelt theory and main spectroscopic parameters.

Glass is an amorphous material formed by different elements such as oxides and/or anhydrides, which, with their covalent bonds, form a disorder matrix during the cooling phase of the fabrication process [42]. The principle characteristics of an optical glass are:

- excellent transparency in visible and infrared spectral regions;
- very good homogeneity and isotropy;
- high threshold to optical damage;
- relative low costs.

When RE elements are incorporated in a glass matrix, they modify the network of the host material occupying interstitial positions inside it. Contemporary, a RE ion incurs in

different kinds of interaction that influence its energy levels distribution. Hence, the Hamiltonian function of eq. (2.1) becomes:

$$H_{TOT} = H_{Free-Ion} + H_{Perturbate d-Ion} \tag{2.2}$$

where

$$H_{Perturbate d-Ion} = V_{Ion-Matrix} + V_{Ion-Photon} + V_{Ion-Ion} \tag{2.3}$$

In the next paragraph we focus our attention on each term of eq. (2.3).

2A.2.a *Effects of glass matrix on the RE ions: the $V_{Ion-Matrix}$ contribution*

The $V_{Ion-Matrix}$ contribution expresses the effects of the glass matrix on the energy levels of RE ions with both static and dynamic interactions taking place. The former type is related to electric fields, known as crystal field contribution, due to the surrounding atoms that interact with the lanthanide ion in the host lattice. This interaction splits each energy level in Stark sublevels. For instance, as shown in Fig. 2.3, the ground state $^4I_{15/2}$ of an Er^{3+} ion in glass is a manifold of eight sublevels of energy E_{0j} and the $^4I_{13/2}$ excite state is a manifold of seven sublevels of energy E_{1j}. In general assuming for level 0 a g_0-fold degeneration and for the level 1 a g_1 degeneration, in case of thermal equilibrium we can write the following equation:

$$g_1 \sigma_{10} = g_0 \sigma_{01} \tag{2.4}$$

.

Let N_0 be the total population of the degenerate ground level $^4I_{15/2}$ and N_1 that of the excited state $^4I_{13/2}$. Applying eq. (2.4) to eq. (1.21) we obtain a new expression for the gain coefficient g:

$$g = N_1 \sigma_{10} - N_0 \sigma_{01} = \sigma_{10} \left(N_1 - N_0 \frac{g_1}{g_0} \right) \tag{2.5}$$

that shows how the degeneration of the energy levels influences the optical gain of the material [30].

Generally, the gap between two Stark sublevels depends on the intensity of the electric field generated by the atoms of the surrounding medium. Nevertheless this separation (the maximum energy gap ΔE is around 200 cm^{-1}) is much lower than that existing between two neighbouring J levels of a free RE ion as shown in Fig. 2.3. The reason of this behaviour is the shielding action of 5s and 5p electrons on those of the 4f shell, as mentioned above.
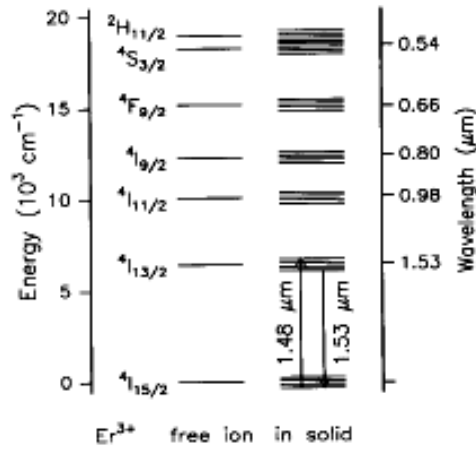
Fig. 2.3: The effect of the crystal field (right) with the splitting
of the energy levels of the free Er^{3+} ion (left) [21].

A dynamic interaction with the lattice is instead associated with non-radiative decays i.e when in the transition of a RE ion from an higher energy level to a lower one, there is no photon emission, and the energy is released to the host lattice through multiphonon relaxation. The probability that an ion at the higher energy level relaxes non-radiatively to the lower one is given by the following relation [43]:

$$W_{nr} = C\left[n(T)+1\right]^{p} e^{-\alpha\Delta E} \tag{2.6}$$

where $n(T) = \dfrac{1}{\exp(\hbar\omega/k_{B}T)-1}$ is the occupation number of a phonon level according to Bose-Einstein statistic. C and α are positive constants characteristic of the host, ω is

the phonon angular frequency, *p* is the number of phonon necessary to cover the energy gap ΔE. Thus, in a multi-phonon interactions, the transition probability quickly decreases with decreasing phonon energy. The large variation in vibrational spectra among different hosts make the non radiative relaxation rate strongly dependent on the glass matrix type.

2A.2.b *Radiative Transitions and Judd-Ofelt method: the $V_{Ion\text{-}Photon}$ contribution and main spectroscopic parameters*

This contribution refers to the electromagnetic interactions between a RE ion and a photon. A general approach in determining the transition probabilities between 4*f* states and radiative lifetime is based on the so-called Judd-Ofelt theory [44,45].

Refering to Fig. 2.4,
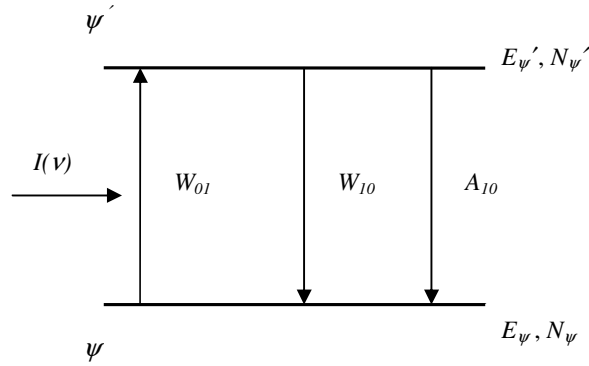
Fig. 2.4: Fundamental mechanism: absorption (W_{01}), spontaneous emission (A_{10}) and stimulated emission (W_{10}) occurring between two general state ψ and $\psi^{'}$.

let us assume with Ψ and $\Psi^{'}$ the initial and the final states of a transition, respectively. Under the approximation that the population of each energy level is uniformly distributed on its constituting Stark, it is possible to derive the theoretical strength associated to each absorption or emission transition of electric dipole f_{ed} between the two states Ψ and $\Psi^{'}$ as:

$$f_{ed} = \frac{8\pi^2 mc}{3\hbar\lambda(2J+1)} \frac{(n^2+1)^2}{9n} \sum_{k=2,4,6} \Omega_k \left\langle \Psi \left\| U_k \right\| \Psi^{'} \right\rangle^2 \qquad (2.7)$$

where λ is the mean wavelength of the transition, n is the refractive index, m is the mass of the electron and J is the total angular momentum of the initial state [46]. The terms $\left\langle \Psi \left\| U_k \right\| \Psi' \right\rangle$ are typical elements of each Rare-Earth, proportional to the reduced matrix elements $\left\langle \left\| U_k \right\| \right\rangle$ tabulated in the literature by Morrison [47], while the intensity parameters Ω_k ($k = 2, 4, 6$) take in account the interactions between vitreous matrix and RE ion.

The electric dipole strength is also directly linked to the absorption spectrum through the relationship:

$$f_{ed} = \frac{m\,c}{\pi\,e^2\,N} \int_\nu \alpha(\nu)\,d\nu \tag{2.8}$$

where $\alpha(\nu)$ is the absorption coefficient at the frequency ν and N is the number of RE ions per volume unit. Then, from a direct measurement of $\alpha(\nu)$ and using eq. (2.8) and (2.7) the values of the phenomenological parameters Ω_k can be calculated. The knowledge of these parameters is important because it allows the calculation of the transitions probabilities related to absorption or emission phenomena. The electric-dipole contribution is computed as follows [46]:

$$A_{ed}\left(\psi' \to \psi\right) = \frac{64\,\pi^4\,e^2}{3\,\hbar\,\lambda^3\,(2J+1)} \frac{n\left(n^2+2\right)^2}{9} \sum_{k=2,4,6} \Omega_k \left\langle \Psi \left\| U_k \right\| \Psi' \right\rangle^2 \tag{2.9}$$

In the same way, the magnetic-dipole contribution depends on the magnetic-dipole operator and is given by:

$$A_{md}\left(\psi' \to \psi\right) = \frac{4\,\pi^2\,e^2\,\hbar}{3\,\lambda^3\,m^2\,c^2\,(2J+1)} n^3 \sum_{k=2,4,6} \Omega_k \left\langle \Psi \left\| (L+2S) \right\| \Psi' \right\rangle^2 \tag{2.10}$$

where $\left\langle \left\| (L+2S) \right\| \right\rangle$ are the magnetic dipole matrix elements also tabulated by Morrison in the intermediate-coupled wave functions set.

Eq. (2.9) and (2.10) express the Einstein's coefficient A.

The radiative lifetime $\tau_{rad}(\psi')$ of a RE ion in an excited state ψ' is then given by:

$$\tau_{rad}(\psi') = \frac{1}{\sum_i A(\psi' \to \psi_i)} \tag{2.11}$$

where the sum is on all the states ψ_i below the excited state ψ' and $A(\psi' \to \psi) = A_{ed}(\psi' \to \psi) + A_{md}(\psi' \to \psi)$. The overall probability of relaxation from an excited state ψ' is:

$$W_T(\psi') = \sum_i A(\psi' \to \psi_i) + W_{nr}(\psi' \to \psi_i) \tag{2.12}$$

where $W_{nr}(\psi' \to \psi_i)$ is the non-radiative decay probability defined in eq. (2.6).

Then, defined the non-radiative lifetime τ_{nr} as:

$$\tau_{nr} = \frac{1}{\sum_i W_{nr}(\psi' \to \psi)} \tag{2.13}$$

the measurable lifetime parameter τ_{meas} can be expressed by:

$$W_T(\psi') = \frac{1}{\tau} = \frac{1}{\tau_{rad}} + \frac{1}{\tau_{nr}} = \frac{1}{\tau_{meas}} \tag{2.14}$$

From equations (2.14) and (2.11) we define the quantum efficiency η as the ratio between the measured and the radiative lifetimes:

$$\eta = \frac{\tau_{meas}}{\tau_{rad}} \tag{2.15}$$

Other important spectroscopic parameters are the absorption and emission cross sections. The former can be obtained directly from the measurement of absorption coefficient $\alpha(\lambda)$, as reported in the following relation [46]:

$$\sigma_a(\lambda) = \frac{\alpha(\lambda)}{N} \tag{2.16}$$

where N is the number of RE ions per volume unit. The latter, knowing the radiative lifetime τ_{rad} and the fluorescence spectrum $I_e(\lambda)$, can be expressed as follows:

$$\sigma_e(\lambda_p) = \frac{\lambda_p^{\,4}}{8\pi c n^2 \Delta\lambda_{eff}} A(\psi' \to \psi) = \frac{1}{8\pi c n^2} \frac{\lambda_p^{\,4}}{\tau_{rad}} \frac{I_{e,\max}}{\int I_e(\lambda) d\lambda} \tag{2.17}$$

where λ_p is the emission peak wavelength and $\Delta\lambda_{eff}$ is the effective bandwidth defined as

$$\Delta\lambda_{eff} = \frac{\int I_e(\lambda) d\lambda}{I_e(\lambda_p)} = \frac{\int I_e(\lambda) d\lambda}{I_{e,\max}} \tag{2.18}$$

with $I_{e,\max} = I_e(\lambda_p)$.

Alternatively, for transitions like the Er^{3+} $^4I_{15/2} \leftrightarrow {}^4I_{13/2}$ one, using the McCumber theory [48], it is possible to express the emission cross section as a function f the absorption cross section:

$$\sigma_e(\nu) = \sigma_a(\nu) \exp\left(\frac{\varepsilon - \hbar\nu}{k_B T}\right) \tag{2.19}$$

where ν is the frequency of the photon of energy $\hbar\nu$ involved in the process, and ε is the temperature-dependent excitation energy. The physical interpretation of ε is the net free energy required to excite one Er^{3+} ion from the ground state at temperature T. An

example of absorption and emission cross-sections of Er^{3+} ions at 1.5 μm, obtained using McCumber theory, is reported in Fig. 2.5 for a tellurite glasses [49].
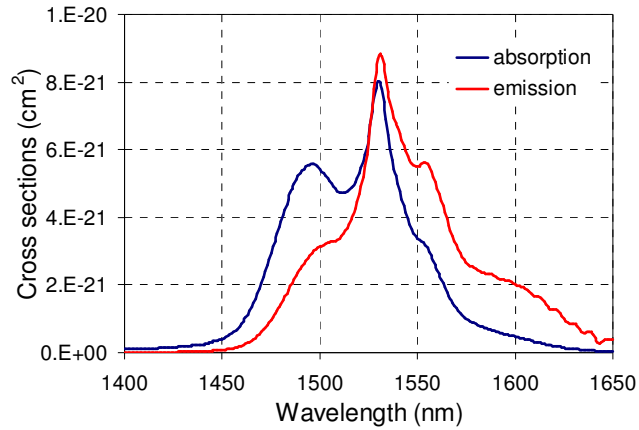
Fig. 2.5: Absorption and emission cross-section of Er^{3+} ion at 1.5 μm in a tellurite glass of molar composition 60 TeO_2 : 25 WO_3 : 15 NaO_2 : 0.5 Er_2O_3

From Fig. 2.5 it is easy to see that, at high frequencies (low wavelengths), the absorption cross-section is larger than the emission one, while, at low frequencies (high wavelengths), the contrary case occurs. Generally, the parameter $\Delta\lambda$, σ_e and σ_a strongly depend on the glass composition, which play a crucial role on the whole spectroscopic properties through the modification of the local environment of rare-earth ions.

The linewidths of the transition showed in fig. 2.5 appears quite broad and this is in part due to the stark splitting of the two multiplets. When the transitions between the different Stark levels are close in energy, the transition lines overlap and appear to form a single large transition.

In general the linewidth of a transition between two given energy levels contains both a homogeneous and inhomogeneous contribution [30]. The former is the natural, temperature dependent, broadening mainly due to nonradiative decay processes. The faster the lifetime, the broader the line. The latter is a measure of the various different sites in which RE ions can be situated within the glass host. In this case, the perturbation changes from one RE ion to another and, for this reason, it is called inhomogeneous broadening.

2.A.2.c Effects of RE ion-ion interaction in glass and pumping processes

The $V_{Ion-Ion}$ term of eq. 2.3 is related to the interaction between two RE ions and strongly depends on their concentration in the host material. This term plays a fundamental role on absorption and re-emission dynamics of light radiation. At low concentration of RE ions the signal amplification is limited by the availability of ions. It could seem, therefore, that simply increasing the doping level we can keep improving the optical gain of the active medium. Nevertheless at high RE concentrations some parasitic effects occur, such as up-conversion phenomena, which induce concentration quenching [2,11]. The result is a reduction in the amplification efficiency of the luminescent material. Let us consider the case of Er^{3+} ions. When the erbium concentration increases, the average distance between neighbouring Er^{3+} ions decreases and simultaneously the electric dipole-dipole interactions become more significant. In this case a non-radiative energy transfer can occur between two ions as shown in Fig. 2.6:
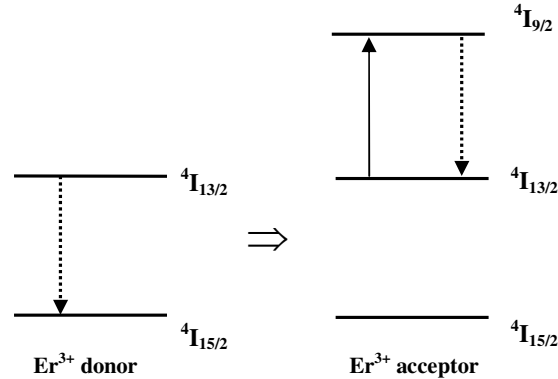
Fig. 2.6 Upconversion effect: energy transfer between two neighbouring Er^{3+} ions originally at the same excited energy level $^4I_{13/2}$.

An Er^{3+} ion (donor) in the excited state $^4I_{13/2}$ transfers its energy, with a non-radiative process, to another neighbouring Er^{3+} ion (acceptor) at the same energy level. Because in erbium the energy gap between the $^4I_{13/2}$ and $^4I_{9/2}$ levels is close to that between the $^4I_{13/2}$ and $^4I_{15/2}$, as result the donor ion falls down to the ground level $^4I_{15/2}$ without any photon emission (dot arrow), while the acceptor ion jumps to the higher energy level

^{4}I$_{9/2}$. From there, the acceptor ion can relax thought successive non-radiative transitions until it reaches again the ^{4}I$_{13/2}$ level. This is the so-called upconversion effect [2,11].

Other parasitic phenomena can involve the pumping mechanism necessary to guarantee the population inversion of Er^{3+} ions in the metastable level ^{4}I$_{13/2}$. The most important is the Excited State Absorption, better known with the acronym of E.S.A. This process is due to absorption of a pump photon from an Er^{3+} ion in the excited state and its working principle is illustrated if Fig. 2.7.
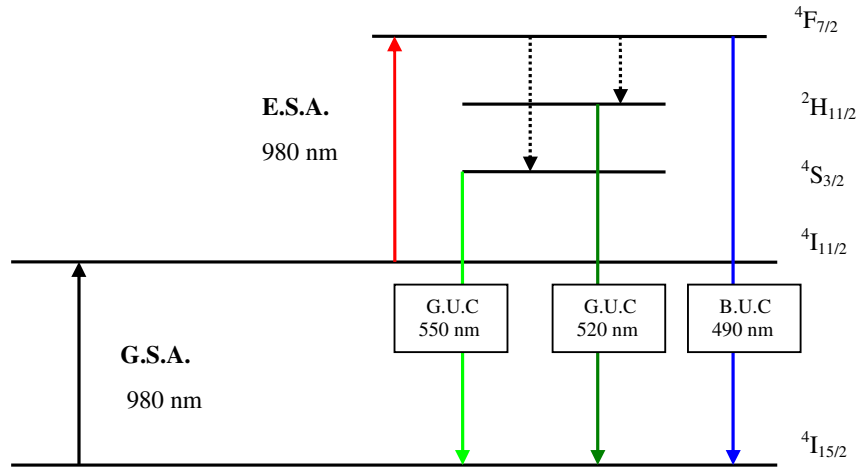
Fig. 2.7 The absorption of a pump photon at 980 nm (G.S.A.) from an excited Er^{3+} ion generates the E.S.A. process (red arrow) with the possibility of Green Up-Conversion (green arrows) or Blue Up-Conversion (blue arrow).

With the absorption of a pump photon at the wavelength of 980 nm, an Er^{3+} ion can be promoted to the excited level ^{4}I$_{11/2}$. This is the Ground State Absorption (G.S.A.) from the fundamental level ^{4}I$_{15/2}$. Usually, from this excited state, the Er^{3+} ion decades non-radiatively until it reaches the metastable level ^{4}I$_{13/2}$. But, before this happens, another pump photon at 980 nm can be absorbed by the excited Er^{3+} ion and the transition ^{4}I$_{11/2}$ → ^{4}F$_{7/2}$ can occur. This is the case of Excited State Absorption (E.S.A.) shown in Fig.2.7 with a red arrow. From this excited state the ion rapidly decays to the ^{2}H$_{11/2}$ and ^{4}S$_{3/2}$ levels (the dot arrows in Fig.2.7). Finally the Er^{3+} ion can relax to the ground level with emission of a photon at the wavelengths of 520 nm or 550 nm (the green arrows in Fig.2.7). In this case we speak of Green Up-Conversion process. With less probability, a

photon emission at 490 nm, in the blue region, can also occur due to the $^4F_{7/2} \rightarrow {}^4I_{15/2}$ transition. This latter is the Blue Up-Conversion (blue arrow in Fig.2.7). It is clear that, for optical amplification, Excited State Absorption can be a strong loss mechanism for pumping: two pump photons are absorbed with only one reemitted but in the visible wavelength region. The E.S.A. phenomena strongly depend upon glass composition and wavelength used for the pump mechanism [2,11].

The energy transfer mechanism between neighbouring ions can be also applied, with some advantage, in case of glasses doped with more than one type of RE ion. A constructive application of such an effect is made co-doping the Er^{3+} doped material with Yb^{3+} ions. In fact, this ion has an energy level structure with two levels, the $^2F_{7/2}$ (fundamental) and the $^2F_{5/2}$ (first excited level), respectively, with a broad absorption bandwidth from 800 nm to 1100 nm (related to Stark sublevel transitions) . In particular, at the wavelength of 980 nm the absorption cross-section σ_a of Yb^{3+} ion is around six times higher than that of Er^{3+}. Hence, using a pump radiation at 980 nm, it is possible to excite more efficiently the Yb^{3+} ions which, for cross-relaxation, transfer their energy to neighbouring Er^{3+} ions. This pump mechanism is shown in Fig.2.8.
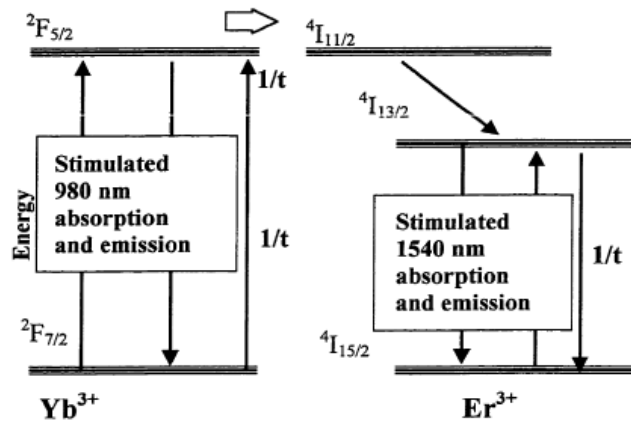

Fig. 2.8 Erbium-Ytterbium energy level diagram illustrating the 980nm pumping scheme[40].

The co-doping with Yb^{3+} ions of an Er^{3+} activated material not only increases the pump efficiency but also increases the distance among erbium ions reducing, contemporary, the quenching processes.

2.A.3 Rate Equations for a three-level system: the case of Er^{3+} /Yb^{3+} doped glass.

A simplified model for a three-levels system in Er^{3+}/Yb^{3+} doped glass, with 980 nm pumping, is shown in Fig. 2.9.
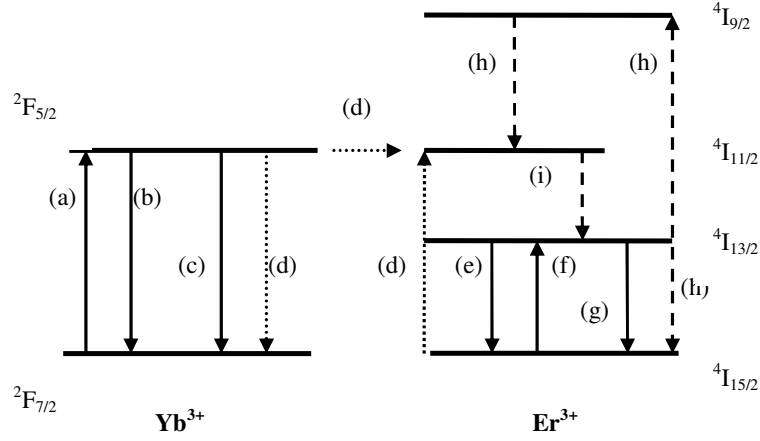
Fig. 2.9 Simplified model of Erbium-Ytterbium system.
The main transitions and energy levels convolved are shown.

According to the nomenclature reported in Fig.2.9, the main processes involved in this modelling are the following [10]:

(a,b) absorption and emission of pump photons from levels $^2F_{7/2}$ and $^2F_{5/2}$, respectively; (c) spontaneous decay of Yb^{3+} from level $^2F_{5/2}$; (d) resonant energy transfer process Yb($^2F_{5/2}$)+Er($^4I_{15/2}$) $\rightarrow$ Yb($^2F_{7/2}$)+Er($^4I_{11/2}$) which acts as indirect pumping of Er^{3+} ions; (e,f) stimulated emission and absorption between the $^4I_{13/2}$ excited level and the $^4I_{15/2}$ fundamental level of Er^{3+} ions; (g) spontaneous decay from the $^4I_{13/2}$ level of Er^{3+} ions; (h) *up-conversion* between two neighbours Er^{3+} ions to higher levels; (i) spontaneous decay of Er^{3+} ions from the $^4I_{11/2}$ level to the $^4I_{13/2}$ metastable level.

Introducing the following hypothesises, (1) the $^4I_{11/2}$ and $^4I_{9/2}$ levels are practically depopulated owing to the rapid non radiative decays related to them and hence the total population of Er^{3+} ions, N_{Er}, can be thought as the sum of N_{0Er} (the ground level population) with N_{1Er} (the higher lasing level population); (2) the main pumping process is represented by a resonant transfer of energy from Yb^{3+} ions to Er^{3+} ions, considering

negligible the direct absorption of pump photons from Er^{3+} ions; then we can write the *Rate Equations* for a three-level system:

$$\left. \frac{d N_1}{d t} \right|_{Yb} = \left(\sigma_{a,Yb} \, N_{0\,Yb} - \sigma_{e,Yb} \, N_{1\,Yb} \right) F_P - K \, N_{1\,Yb} \, N_{0\,Er} - \frac{N_{1\,Yb}}{\tau_{Yb}}$$

$$\left. \frac{d N_1}{d t} \right|_{Er} = \left(\sigma_{a,Er} \, N_{0\,Er} - \sigma_{e,Er} \, N_{1\,Er} \right) F_L + K \, N_{1\,Yb} \, N_{0\,Er} - \frac{N_{1\,Er}}{\tau_{Er}} - C \, N^2_{1\,Er}$$

(2.20)

where $N_{0\,Yb}$, $N_{1\,Yb}$ are the populations of $^2F_{7/2}$ and $^2F_{5/2}$ levels of Yb^{3+} ions and $N_{0\,Er}$, $N_{1\,Er}$ those of $^4I_{15/2}$ and $^4I_{13/2}$ levels of Er^{3+} ions; $\sigma_{a,Yb}$, $\sigma_{e,Yb}$, $\sigma_{a,Er}$, $\sigma_{e,Er}$ are the absorption and emission cross sections of Yb^{3+} and Er^{3+} ions, respectively; τ_{Yb} and τ_{Er} the lifetimes of $^2F_{7/2}$ and $^4I_{13/2}$ levels for Yb^{3+} and Er^{3+} ions, respectively; F_L and F_P the photon fluxes for laser and pumping radiation; K and C the energy transfer and up-conversion coefficients.

2B Spectroscopic Characterization of Er^{3+}/Yb^{3+} -doped glasses: Experimental

2.B.1 Glass composition and fabrication

We have tested different formulations of oxide glasses doped with Er^{3+} and/or Yb^{3+} ions for integrated optical amplifiers and lasers. Principally our choice has fallen on silicate glasses rather than phosphates for their superior chemical resistance and greater adaptability to different fabrication processes. However phosphate glasses, due to the high solubility of rare-earth ions, remain among the better hosts for laser and amplifier devices. For this reason in this work we also considered a commercial phosphate glass. The compositions of the glasses used in our experiments are reported in Table 2.2.

Oxide	MY2 [mol%]	SLASY1 [mol%]	SiO$_2$-GeO$_2$ [mol%]	B05 [mol%]	IOG2 [wt%]	IOG10 [wt%]
SiO$_2$	73	62	75	77.29	-	-
Al$_2$O$_3$	1	17	-	-	-	-
P$_2$O$_5$	0.4	0.3	-	-	-	-
Na$_2$O	14	12	-	-	4.56	-
K$_2$O	0.6	0.5	-	11.86	-	-
CaO	11	9	-	-	-	-
GeO$_2$	-	-	25	-	-	-
PbO	-	-	-	10.37	-	-
Sb$_2$O$_3$	-	-	-	0.48	-	-
Er$_2$O$_3$	0.32	0.4	0.1	0.5	2	1
Yb$_2$O$_3$	0.63	0.4	0.1	-	3	8

Table 2.2 Compositions of oxide glasses used for our experiments.

Soda-Lime Silicate (MY2) and alumino-silicate (SLASY) glasses

These two glasses were both fabricated at the Stazione Sperimentale del Vetro di Murano (Venice) by a conventional melt-quenching technique [P.IV]. The glasses were doped with erbium and co-doped with ytterbium. Their high sodium oxide concentration makes these materials suitable for fabrication of integrated optical amplifiers and lasers by the ion-exchange process. Moreover, the high content of aluminium oxide present in SLASY glass has the effect of increasing its emission bandwidth (around 1.55 μm) and making it qualified for WDM (Wavelength Division Multiplexing) applications.

Silicate B05 glass

The B05 sample is an innovative erbium doped modified silicate glass, produced in the Baccarat Cristallerie, and is a valuable candidate for further applications in optical technologies as, for instance, microsphere lasers. Standard melt-quenching process was used in the fabrication of B05 too.

Commercial Silicate (IOG10) and phosphate (IOG2) Schott glasses

These oxide glasses are both produced by Schott Company, a leader in optical glass manufacturing. Being commercial glasses, their compositions are not exactly known with the exception of the Er^{3+} and Yb^{3+} concentrations. IOG10 is a phosphorous-free, mixed alkali, zinc-silicate glass suitable for laser applications. On the other hand, IOG2 is a potassium-barium-alumino phosphate glass. Although it is not chemically durable as silicate glasses, IOG2 seems to be an excellent candidate for active photonic devices that require high gain. Waveguide lasers have already been fabricated on both glasses. We decided to use them for the realization of optical microsphere lasers.

SiO_2-GeO_2 thin film

This binary system thin glass layers were fabricated at the Institute of Photonics and Nanotechnologies (Trento Section), depositing the two oxides on silica substrates by a RF (radio frequency) magnetron sputtering technique. The composition is reported in Table 2.2, with that of the Er^{3+}/Yb^{3+} doping. Thanks to their photorefractive properties, SiO_2-GeO_2 thin films doped with rare-earth ions may represent an effective route to the simple fabrication of integrated optical amplifiers and lasers through direct UV laser writing or imprinting.

2.B.2   Absorption Measurements: set-up and results

<u>Set-up</u>

Optical absorption measurements were performed at room temperature with a Perkin Elmer $\lambda 19$ Spectrophotometer, which measures the transmittance of a sample in a wide range of wavelengths between ultraviolet and infrared regions. The instrument is almost completely automatic and guarantees a resolution of 1 nm. Both facets of the glass sample need to be polished first. The spectrophotometer measures the decrease of the optical intensity of the beam travelling through the sample as a function of wavelength λ. Labelling with I_0 the intensity incident on the sample and with I_T the transmitted one, the transmittance is defined as:

$$T(\lambda) = \frac{I_T(\lambda)}{I_0(\lambda)} \qquad\qquad (2.20)$$

The transmitted intensity radiation is related to the incident one through the Lambert-Beers law:

$$I_T(\lambda) = I_0(\lambda) \exp\left[-\alpha(\lambda)L\right] \qquad\qquad (2.21)$$

where $\alpha(\lambda)$ is the absorption coefficient and L is the thickness of the sample. Combining the equations (2.20) and (2.21) we obtain:

$$T(\lambda) = \exp\left(-\alpha(\lambda)L\right) \qquad\qquad (2.22)$$

from which, knowing the thickness of the sample and measuring $T(\lambda)$, it is possible to obtain the absorption coefficient. Hence, applying the eq. (2.16), it is easy to calculate the value of the absorption cross section $\sigma_a(\lambda)$.

Soda-Lime silicate (MY2) and alumino silicate (SLASY1) glasses

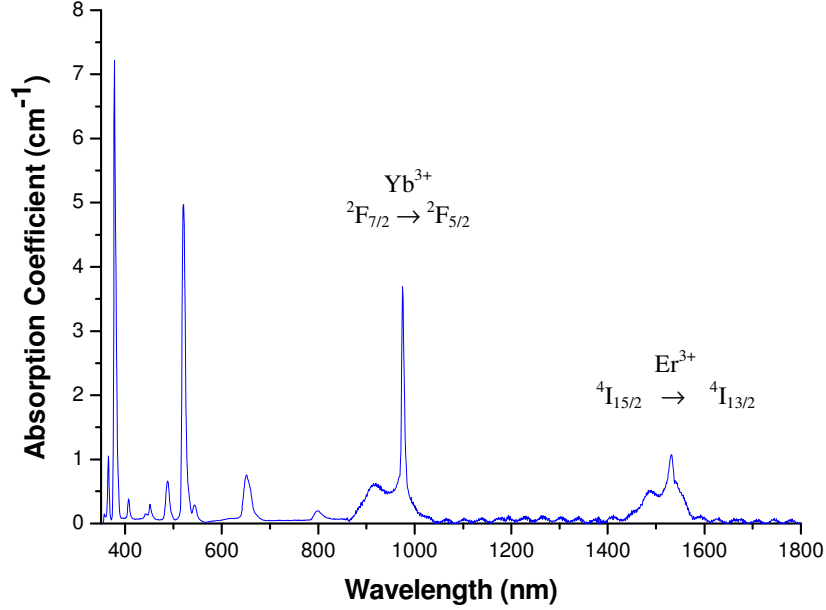The UV-Vis-NIR absorption spectrum obtained for the SLASY1 glass [P.IV] is plotted in Fig. 2.10.

Fig. 2.10: Room temperature absorption spectrum in the UV-Vis-NIR spectral region for SLASY1 sample. The Er^{3+} and Yb^{3+} transitions, around 1530 nm and 980 nm, respectively, are highlighted.

The spectrum is characteristic of Er^{3+}/Yb^{3+} silicate oxide glasses [39]. The absorption bands of our interest are identified with the transitions $^4I_{15/2} \rightarrow {}^4I_{13/2}$ of Er^{3+} ions around 1530 nm and $^2F_{7/2} \rightarrow {}^2F_{5/2}$ of Yb^+ ions around 980 nm. In fact also Er^{3+} ions present, at 980 nm, the $^4I_{15/2} \rightarrow {}^4I_{11/2}$ transition, which overlaps with that of Yb^{3+} mentioned above

We assume that the total absorption coefficient at wavelength $\overline{\lambda}$ is equal to the sum of the Er^{3+} and Yb^{3+} absorption coefficients according to the following relationship:

$$\alpha_{TOT}\left(\overline{\lambda}\right) = N\left(Er^{3+}\right) \cdot \sigma_a^{Er}\left(\overline{\lambda}\right) + N\left(Yb^{3+}\right) \cdot \sigma_a^{Yb}\left(\overline{\lambda}\right) \qquad (2.23)$$

with N the nominal concentrations of Er^{3+} or Yb^{3+} ions. Knowing the absorption cross section of Yb^{3+} ions alone, then, from eq. (2.23) it is possible to calculate the absorption cross section of Er^{3+} ions at $\overline{\lambda}$ wavelength. In the case of SLASY1 sample, the resulting value of Er^{3+} absorption cross section around 980 nm was $(0.25 \pm 0.01) \times 10^{-20}$ cm^2, as reported in our work [P.IV]. This value is almost seven times smaller than the corresponding Yb^{3+} absorption cross-section (around 1.80×10^{-20} cm^2). This result confirms that co-doping with Ytterbium ions can drastically improve the pump efficiency of a glass activated with Er^{3+} ions for laser and amplifier applications.

In Table 2.3 we report the total absorption coefficients measured around 0.98 and 1.53 μm together with the cross sections σ_a of Er^{3+} ions at the same wavelengths for SLASY1 and MY2 samples, respectively. The rare-earths concentration is also reported.

Glass	Concentration (ion/cm^3) $\times 10^{20}$		980 nm		1530 nm	
	Er^{3+}	Yb^{3+}	α (cm^{-1})	σ_a (cm^2) $\times 10^{-20}$	α (cm^{-1})	σ_a (cm^2) $\times 10^{-20}$
MY2	1.55	3.10	4.10	0.11	0.43	0.28
SLASY1	1.80	1.80	3.69	0.25	1.08	0.60

Table 2.3 Erbium and itterbium concentrations, absorption coefficients and erbium absorption cross-sections for MY2 and SLASY1 glasses.

The absorption FWHM (Full Width at Half Maximum) and effective bandwidth for the $^4I_{15/2} \rightarrow {}^4I_{13/2}$ transition of Er^{3+} ions are 16 nm ($\pm$ 1 nm) and 32 nm ($\pm$ 1 nm) for MY2 glass and 22 nm ($\pm$ 1 nm) and 53 nm ($\pm$ 1 nm) for SLASY1 sample [P.IV], respectively. The effect of an increase of alumina content on the shape of the absorption spectrum of Yb^{3+} ions around 980 nm is shown in Fig. 2.11.
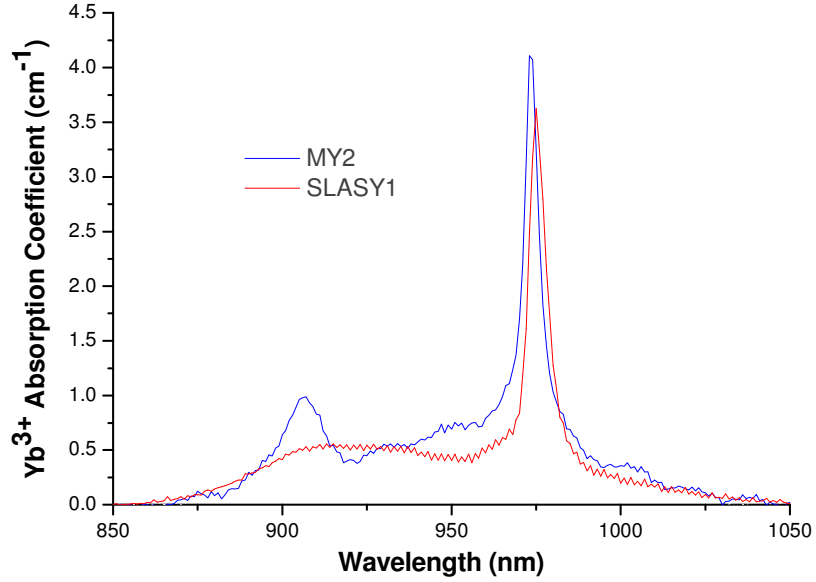
Fig.2.11: Comparison of Yb^{3+} absorption spectra around 980 nm
for MY2 and SLASY1 glasses [P.IV].

We can observe a red shift for the Yb^{3+} absorption peak λ_{peak} from 973 nm (in the case of MY2 glass) to 975 nm (in the case of SLASY1). Moreover, in the region between 900 nm and 970 nm, the profile of the absorption curve appears to be much flatter for the SLASY1 than for the MY2 glass. We believe that this effect is related to the high aluminium oxide concentration in the new SLASY1 glass formulation.

In reference [P.VII] we have studied the influence of increasing alumina content on the absorption properties of Er^{3+} ions around 1.55 μm, for another set of soda-lime alumino silicate glasses (AL glasses). In particular, as indicated in the Fig. 2.12, the basic composition of AL01 sample is similar to that of MY2 and the same applies for the pair of samples AL20 and SLASY1. As shown in the same figure we successfully demonstrated an increase up to 60% (from 32 nm to 50 nm) for the effective absorption bandwidth $\Delta \lambda_{eff}^{\ abs}$ of Er^{3+} ions when varying alumina content, inside the glass matrix, from 1 to 20, mol%.
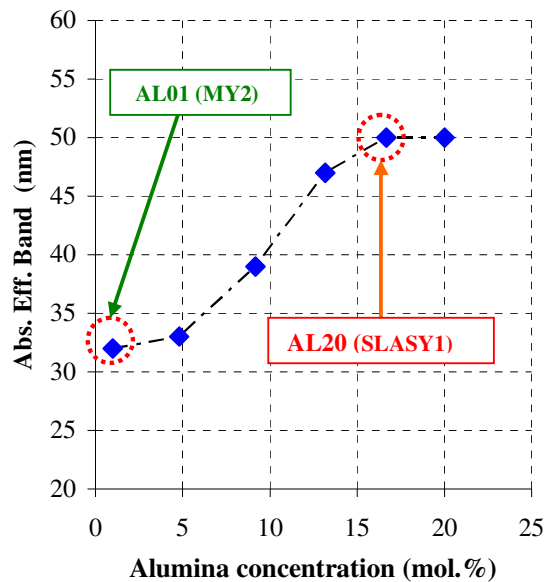
Fig.2.12: Dependence of absorption effective bandwidths on the increase of Al_2O_3 oxide concentration in an alumino-silicate glass matrix [P.VII]. The composition of soda-lime silicate glass MY2 is similar to that of AL01 while the composition of SLASY1 sample is closed to that of AL20.

The reason of this change for the effective absorption bandwidth is related to the different effect that aluminium oxide has on the silica network, acting as glass modifier for lower concentration and as glass former for higher ones [P.VII].

Modified Silicate B05 (Baccarat) glass

Fig.2.13 shows the absorption cross section for the $^4I_{15/2} \rightarrow ^4I_{13/2}$ transition of Er^{3+} ions in the B05 silicate glass.

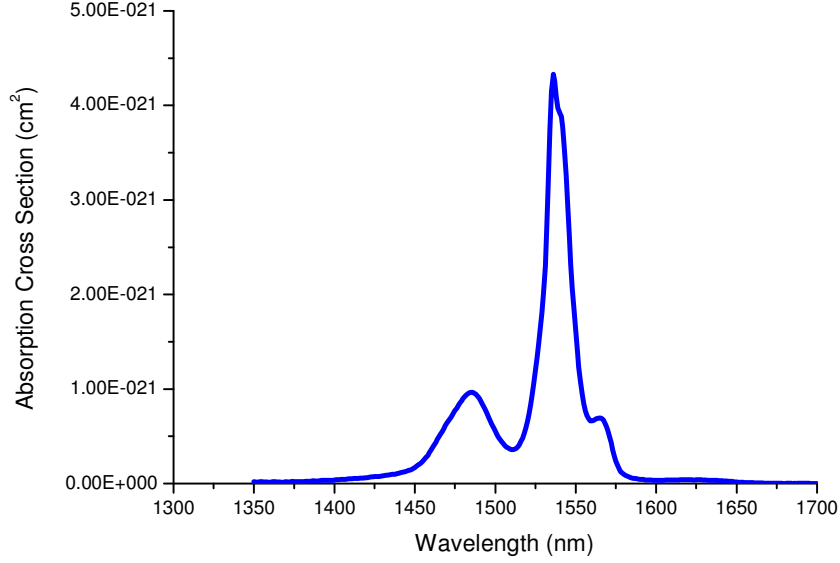**Fig.2.13**: Absortption cross section around 1530 nm for B05 glass

At the peak absorption wavelength of 1536 nm, the measured cross section σ_a is 4.33×10^{-21} cm^2. Being 2.2×10^{20} cm^{-3} the concentration of the Er^{3+} ions in the B05 glass, the absorption coefficient can be calculated from eq. (2.16) obtaining a value for α of 0.953 (cm^{-1}). As for absorption FWHM and effective bandwidths we got results typical of silicate glasses: 19 nm ($\pm$ 1 nm) and 32 nm ($\pm$ 1 nm), respectively.

Commercial Silicate (IOG10) and phosphate (IOG2) Schott glasses
In Fig. 2.14 is reported, in solid line, the absorption cross-section spectrum of IOG2 glass. A high peak value of 7.6×10^{-21} cm^2 is observed for the ^{4}I$_{15/2} \rightarrow ^4$I$_{13/2}$ transition of Er^{3+}. In the same figure, in dotted line, we show the emission cross-section spectra obtained using the reciprocity relation of McCumber's theory expressed in eq. (2.19). The calculated peak value is 8.0×10^{-21} cm^2 at 1533 nm.
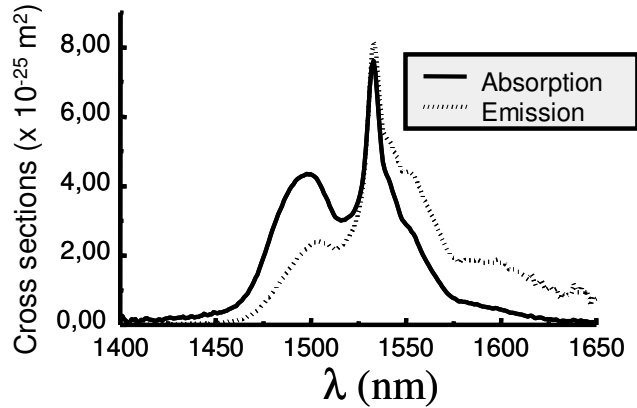
Fig.2.14: Er^{3+}/Yb^{3+} IOG2 phosphate glass: absorption (solid line) and emission (dot line) spectra.

Typically absorption and emission cross section are larger in phosphate glasses (like IOG2) than in silicate glasses (like Baccarat B05). Similarly absorption and emission effective bandwidths $\Delta \lambda_{eff}$ are wider (~50 nm) in a phosphate glass than in a silicate glass (only ~30 nm) [2,11]. These characteristics make phosphate glasses a suitable candidate for amplifiers in WDM as well as for laser sources able to exploit the broad erbium gain bandwidth.

As for IOG10 commercial silicate glass we obtained the results synthesized in Table 2.4, for the total absorption coefficients measured around 0.98 and 1.53 μm. Absorption cross sections σ_a of Er^{3+} ions at the same wavelengths are also reported. The effective absorption bandwidth related to the $^4I_{15/2} \rightarrow {}^4I_{13/2}$ transition is 32 nm ($\pm$ 1 nm), while the corresponding value of the FWHM is 15 nm ($\pm$ 1 nm).

Glass	Concentration $(ion/cm^3) \times 10^{20}$		980 nm		1530 nm	
	Er^{3+}	Yb^{3+}	α (cm^{-1})	σ_a (cm^2) $\times 10^{-20}$	α (cm^{-1})	σ_a (cm^2) $\times 10^{-20}$
IOG10	0.88	6.83	8.3	0.10	0.50	0.57

Table 2.4: Absorption cross-sections of Er^{3+} ions and total absorption coefficients at 980 nm and 1530 nm for IOG10 Schott silicate glass.

2.B.3   Fluorescence Measurements: set-up and results

Set-up

The fluorescence band of our interest corresponds to the $^4I_{13/2} \rightarrow {}^4I_{15/2}$ transition of erbium ions centred around 1530 nm. The excitation mechanism used in our experiments is shown in Fig.2.15
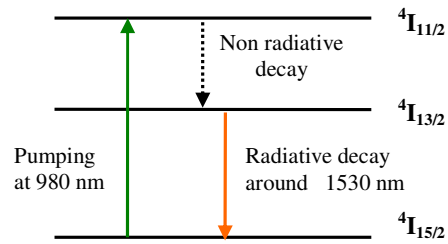

Fig.2.15: Pumping scheme of Er^{3+} used for the fluorescence measurements around 1530 nm

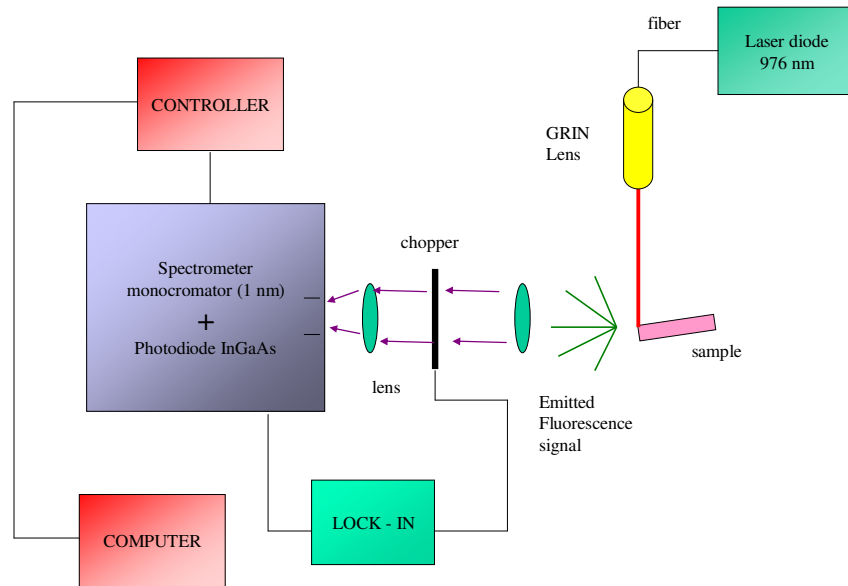The experimental set-up is sketched in Fig. 2.16.

Fig.2.16: Experimental set-up for fluorescence measurement.

As excitation source we used a 976 nm laser diode, wavelength stabilized by a fibre Bragg grating. The laser beam was collimated through a fiber pigtailed GRIN lens and sent to the edge of the sample. The fluorescence signal emitted from the sample was focused on the input opening of a SPEX 270M spectrometer, by means of a two lenses system. Inside the spectrometer, after a first reflection on a collimating mirror, the signal is directed to a rotating grating. The part of fluorescence signal reflected by the grating undergoes another reflection through a second mirror that focalizes the radiation on a InGaAs photodiode, which is at the output opening of the spectrometer. A lock-in technique was used to improve the signal-noise ratio. The amplified signal was acquired from an A/D converter and hence sent to a computer for data elaboration and visualization in real time. The pump power adopted in our experiments was around 30 mW, which was enough to acquire the fluorescence spectra with an acceptable noise level. The width of the input and output slits were set at 0.1 and 0.12 mm, respectively. This difference in width, due to the broadening of the beam through the optical system inside the spectrometer, guaranteed a spectral resolution of 1 nm. In this way, using an integration time of 3 seconds and a scan length of 300 nm (from 1400nm to 1700 nm), each measurement took about 9 minutes.

Results

Soda-Lime silicate (MY2) and alumino silicate (SLASY1) glasses
Fig. 2.17 compares the normalized fluorescence spectra of MY2 and SLASY1 samples. As we can see, in the case of SLASY1 glass a much broader fluorescence bandwidth is measured. We believe that the explanation for this behaviour, analogous to that observed for the absorption spectra, is related to the higher aluminum oxide concentration in SLASY1. For further investigation on this subject, we refer to the wide literature [2,11,50-51,P.VII].
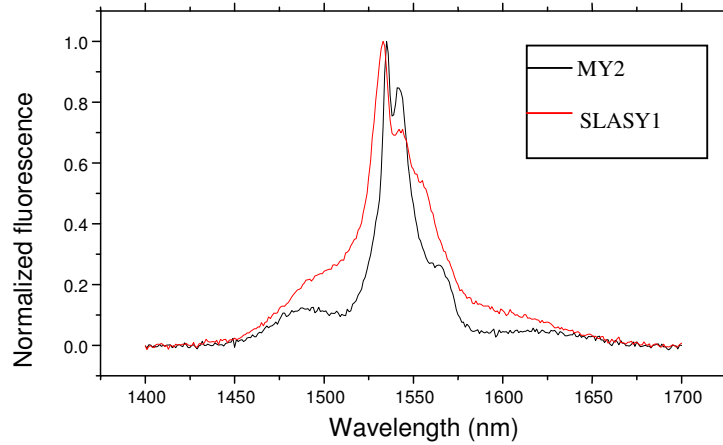
Fig.2.17: Comparison between the fluorescence spectra of samples MY2 and SLASY1. Their maximum amplitudes were normalized to one

In particular, as summarized in Table 2.5, the soda-lime silicate glass MY2 shows an effective emission bandwidth of 32 nm (± 1 nm) with FWHM of 17 nm (± 1 nm) while the corresponding values for SLASY1 glass formulation are 52 nm (± 1 nm) and 30 nm (± 1 nm), respectively.

Sample	$\Delta\lambda^{FWHM}_{fl}$ (±1 nm)	$\Delta\lambda^{eff}_{fl.}$ (±1 nm)	λ_p (±1 nm)
MY2	17	32	1535
SLASY1	30	52	1534

Table2.5: Fluorescence FWHM and effective bandwidth for the $^4I_{13/2}$ → $^4I_{15/2}$ transition, measured for different experimental silicate glasses. The peak emission wavelength is also reported.

These results confirm the potentiality of high alumina content silicate glasses for the development of high-performance broadband optical amplifiers and lasers.

Modified Silicate B05 (Baccarat) glass

The emission cross section for the $^4I_{13/2} \rightarrow {}^4I_{15/2}$ transition of Er^{3+} ions in the B05 modified silicate glass is presented in Fig.2.18.
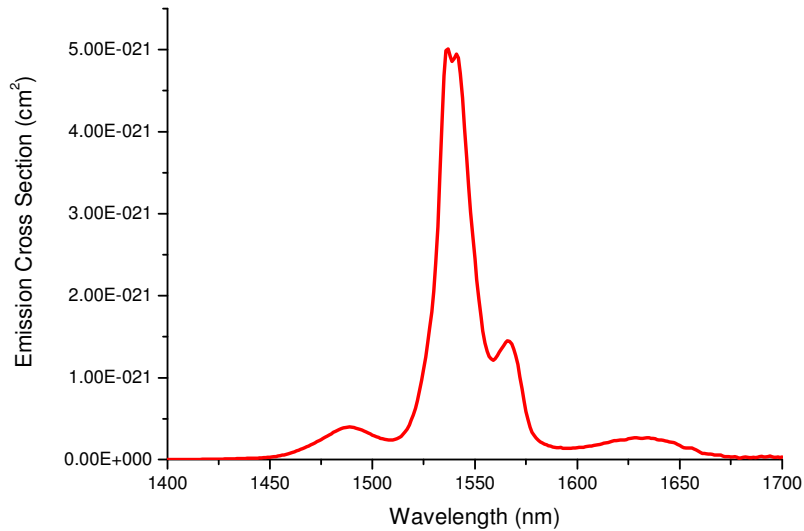
Fig..2.18: Emission cross section around 1530 nm for B05 glass

At the emission peak wavelength (1537 nm) the measured cross section σ_e is 5.21×10^{-21} cm^2. As for the absorption FWHM and effective bandwidth we got again results typical of silicate glasses: 18 nm ($\pm$ 1 nm) and 32 nm ($\pm$ 1 nm), respectively.

Commercial Silicate (IOG10) and phosphate (IOG2) Schott glasses

As shown in Fig.2.13, the peak emission cross section σ_e for IOG2 phosphate glass is 8.0×10^{-21} cm^2 at the wavelength of 1533 nm.

As for IOG10 silicate glass, in Fig.2.19 we report its fluorescence spectrum with a peak wavelength of 1536 nm.

42
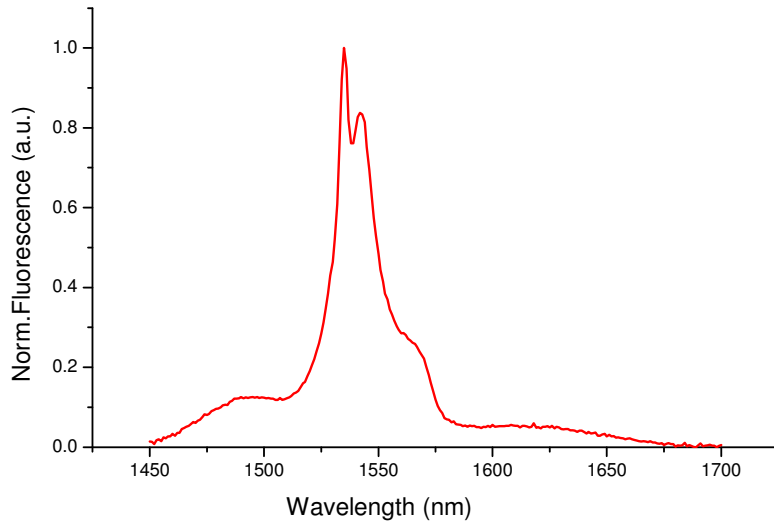
Fig..2.19: Normalized fluorescence spectrum of IOG10 Schott silicate glass.

The emission peak value and other main emission parameters are reported in Table 2.6

Sample	$\Delta\lambda^{FWHM}_{fl}$ $(\pm1\ nm)$	$\Delta\lambda^{eff}_{fl.}$ $(\pm1\ nm)$	σ_ε $(\pm0.01\ cm^2)$
IOG10	18	32	5.8×10^{-21}

Table2.6: Fluorescence FWHM, effective bandwidth, and peak emission cross section for the $^4I_{13/2} \rightarrow {}^4I_{15/2}$ transition, measured in IOG10 Schott silicate glass.

The high concentration of Yb^{3+} ions makes this glass suitable for lasing devices.

SiO₂-GeO₂ thin film

In Fig. 2.20 we report the fluorescence spectrum of SiO_2-GeO_2 films doped with Er^{3+}/Yb^{3+} obtained by exciting the TE_0 waveguide mode at 514.5 nm using prism coupling technique [17].

The peak of the emission spectrum is at f 1533 nm while the measured FWHM around that wavelength is about 40 nm, much larger than in most erbium-doped multi-component silicate glasses [2,39,52]. The presence, in the same spectrum, of the typical Yb^{3+} emission profile around 980 nm indicates the presence of back energy transfer process from Er^{3+} to Yb^{3+} ions [53].
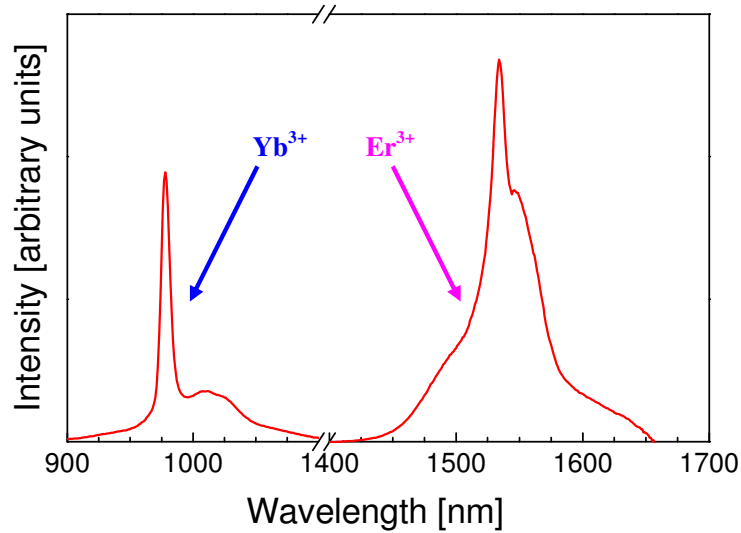
Fig. 2.20: Waveguide room temperature fluorescence spectrum in the region of the $^4I_{13/2} \rightarrow ^4I_{15/2}$ transition of Er^{3+} ions and in the region of the $^2F_{5/2} \rightarrow ^2F_{7/2}$ transition of Yb^{3+} ions. The excitation wavelength is 514 nm.

However, the luminescence excitation spectrum detected at 1533 nm and reported in Fig.2.21 shows that the energy transfer from Yb^{3+} to Er^{3+} ions is quite effective. In fact the spectral shape of the excitation spectrum corresponds to the typical ytterbium absorption [39,P.IV].
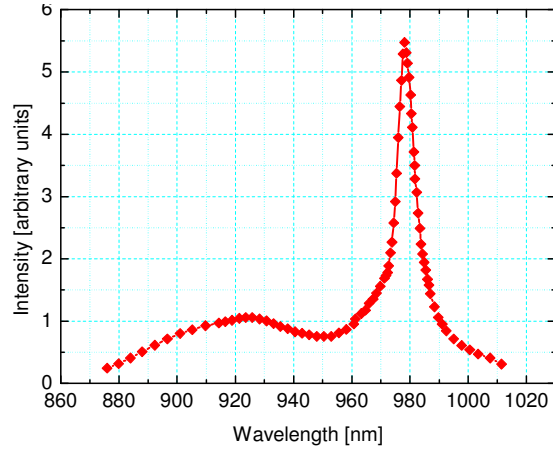
Fig.2.21: Photoluminescence excitation spectrum of the SiO2–GeO2:
Er3+/ Yb3+-codoped waveguide. The detection wavelength was set to
1533 nm.

2.B.4 Lifetime Measurements: set-up and results

Set-up

The lifetime measurement for the $^4I_{13/2} \rightarrow$ $^4I_{15/2}$ transition is very important for the characterization of our materials. As mentioned above, quenching effects may be assessed comparing the measured lifetime of the $^4I_{13/2}$ metastable level with the radiative one, obtained applying the Judd-Ofelt method [44,45]. The experimental set-up used for these measurements is reported in Fig.2.22
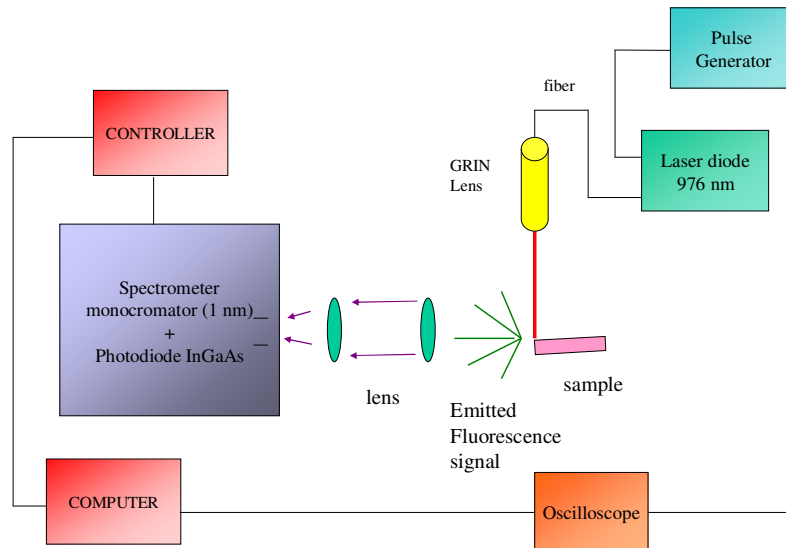
Fig.2.22: Experimental set-up for lifetime measurement

In comparison with set-up shown in Fig.2.16 two new pieces of equipment appear: a pulse generator and an oscilloscope. The former is connected with a pump laser and modulates the excitation radiation with a suitable square wave. The latter shows the result of time resolved fluorescence measurement according to the exponential decay law:

$$I = I_0 \, e^{-t/\tau} \tag{2.24}$$

where τ is the lifetime.

Results

Soda-Lime silicate (MY2) and alumino silicate (SLASY1) glasses
We studied the effect of an increase of alumina content on the measured lifetimes on AL glass formulations [P.V,P.VII] and the main results are reported in Fig. 2.23.
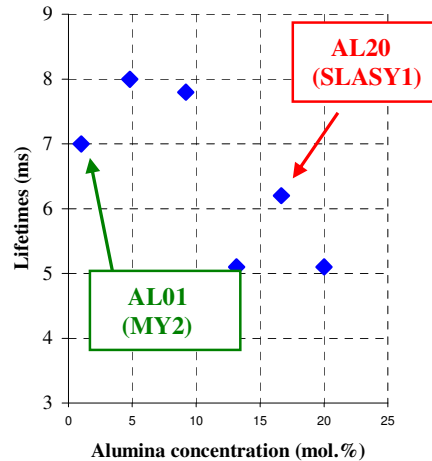
Fig.2.23: Measured lifetimes as a function of alumina
concentration in the glass.

A possible explanation of the different set of values obtained is again related to the different role that the aluminum oxide has on the silica network, as glass modifier and as a glass former, respectively. In particular, in the network modifier case (alumina < 10% mol.), the aluminum ions contribute to disrupt the silica structure and produce non-

bridging Al-O groups, which can then coordinate the Er^{3+} ions, thus reducing the Er^{3+} - Er^{3+} interaction and increasing the lifetime [50]. On the other hand, a further increase of aluminum oxide in the glass matrix reduces the non-bridging oxygen ions and allows the creation of Al−O−Si bridging oxygen (alumina as glass former), thus reducing the measured lifetimes. In Table 2.7 we summarize the main results in terms of Judd-Ofelt intensity parameters Ω_i, measured and calculated lifetime τ and quantum efficiency for MY2 and SLASY1 glasses.

Samples	Ω_2 $(10^{-20}cm^2)$	Ω_4 $(10^{-20}cm^2)$	Ω_6 $(10^{-20}cm^2)$	τ_{meas} ($\pm$ 0.2 ms)	$\tau_{calc.}$ ($\pm$ 0.2 ms)	η
SLASY1	8.19 ($\pm$ 0.58)	1.70 ($\pm$ 0.83)	1.00 ($\pm$ 0.29)	4.1	8.71	0.47
MY2	4.90 ($\pm$ 0.06)	0.84 ($\pm$ 0.06)	0.52 ($\pm$ 0.02)	7.5	12.0	0.62

Table2.7: Judd-Ofelt intensity parameters, measured and calculated lifetime τ and quantum efficiency for MY2 and SLASY1 samples.

The decrease of radiative and measured lifetimes from MY2 to SLASY1 glasses can be related to an increase in both the magnetic and the electric dipole contributions with the Judd-Ofelt intensity parameters, in particular Ω_4 and Ω_6, that affect the electric dipole contribution. Comparing the results presented in Fig. 2.23 with those reported in Table.2.7, we discover a significant difference between the measured lifetime of SLASY1 sample (4.1 ms), and that of the AL20 sample (same alumina content but without Yb^{3+} ions) equal to 6.2 ms.. This gives a 50% lower quantum efficiency. So far we do not have a specific explanation for this behavior (even if the possible presence of Fe impurities related to the introduction of Yb^{3+} could be considered).

Modified Silicate B05 glass, IOG10 Silicate and IOG2 Phosphate Schott glasses, SiO$_2$-GeO$_2$ thin film.

Finally, in Table 2.8, we report the values of measured lifetimes for the other glass formulations considered in our work.

glass	τ_{meas} (± 0.2 ms)	τ_{calc}	η
B05	11.5	18.4	0.62
IOG10	10.2	17.8	0.57
IOG2	6.8	-	-
SiO$_2$-GeO$_2$	8.7	-	-

Table2.8: Measured, calculated lifetime τ and quantum efficiency
for B05, IOG10, IOG2 and SiO$_2$-GeO$_2$ samples.

The high lifetime values measured in B05 and IOG10 samples and their rather good quantum efficiency confirm that the erbium ions are homogeneously distributed in the glass matrix and their interactions are practically negligible.

2.B.5 *Effect of glass fusion process on the spectroscopic properties Er^{3+} - doped oxide glasses: the case of fused microsphere.*

In literature there are very few papers on the effects that the glass fusion process may have on the spectroscopic properties of the material. We considered the case of Er^{3+} doped microspheres obtained by fusion of glass precursor through a plasma torch.

Figure 2.24 shows the photoluminescence spectra of the $^4I_{13/2} \rightarrow {}^4I_{15/2}$ transition of Er^{3+} ions for the bulk sample and the respective microsphere in B05 glass.
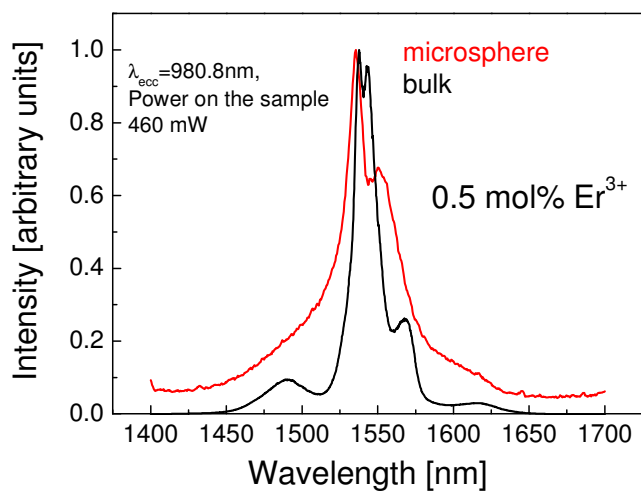
Fig.2.24: Room temperature photoluminescence spectra of the $^4I_{13/2} \rightarrow ^4I_{15/2}$ transition of Er^{3+} ions for the bulk sample (black) and the respective microspheres (red) in B05 modified silica glass.

A broadening of the luminescence spectrum can be clearly observed from the B05 bulk sample to the B05 microsphere. Correspondingly a shortening of the lifetime was also measured in the microsphere as compared to the corresponding bulk glass as shown in Figure 2.25.
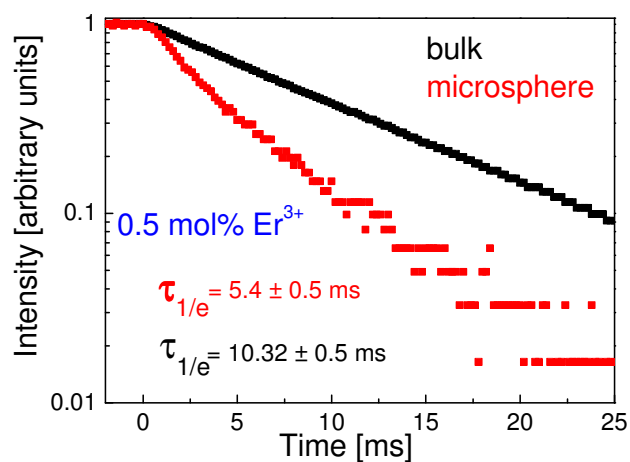
Fig. 2.25: Luminescence decay curves of $^4I_{13/2} \rightarrow ^4I_{15/2}$ transition of Er^{3+} ions for the bulk sample (black) and the respective microsphere (red) in B05 modified silicate glass.

On the contrary, using IOG2 phosphate glass, we did not observe a significant broadening of the bandwidth and we observed a smaller reduction in the lifetime values, as shown in Fig. 2.26
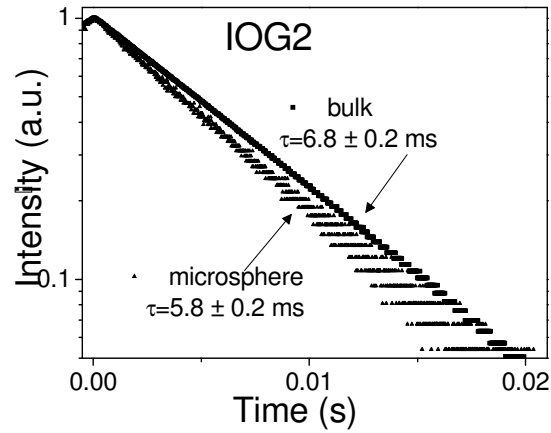
Fig. 2.26 : Luminescence decay curves of $^4I_{13/2} \rightarrow {}^4I_{15/2}$ transition of Er^{3+} ions for the bulk sample (squares) and the respective microsphere (triangles) in IOG2 phosphate glass.

A possible explanation for these quite interesting results, that we reported in our works [P.VI,P.VIII], is related to site to site inhomogeneities and changes in the local environment of Er^{3+} ion induced by the fabrication process. This effect has to be especially considered if we want to use microspherical laser performances as a 'test bed' for the active glass itself.

CHAPTER 3 *Devices: Development of a waveguide laser.*

Channel waveguides, for their capacity to confine light both laterally and in depth, are the basic blocks of many passive and active integrated optical devices such as switches, splitters, amplifiers and lasers [6]. If compared with semiconductor, glass waveguide lasers activated with Er^{3+}/Yb^{3+} show some important advantages: i) their high lifetimes (of the order of millisecond versus nanoseconds offered by semiconductor laser) allow to obtain a more efficient population inversion with better signal-to-noise-ratio (SNR); ii) their lower noise reduces the possibility of fluctuations in intensity, phase and frequency guaranteeing, at the same time, a narrower linewidth. On the contrary, their major drawback is that they require optical pumping in comparison with semiconductor lasers that can be pump electrically. Moreover, compared with fiber lasers, waveguide lasers exhibit a higher integration factor, having the possibility to be interfaced with other components realized on the same optical chip.

Fabrication processes strongly depend on the choice of the materials. The main technological strain consists in a reduction of fabrication costs, simplifying the processes without losing in terms of performances.

In this sense glass materials, for their higher adaptability to different fabrication processes and their undoubtedly low costs, fully respond to this aim.

Among the main manufacturing routes for the development of integrated optical amplifiers and lasers in Er^{3+}/Yb^{3+} doped glasses, we can list ion-exchange [39,54-56]; the deposition of thin film by RF magnetron sputtering, chemical vapour deposition (CVD), or sol-gel processes [P.II,59-63] and ion implantation with proton or heavy ions [64-66]. Moreover, in the last years, advances have being made in laser-based fabrication and patterning processes of glass structures, which include UV-laser and femtosecond-laser writing of channel waveguides in bulk glasses or in glassy thin-film [18-20,67-68].

In this chapter the results we obtained in the development of waveguide lasers will be presented. For this purpose different fabrication processes and materials have been selected: i) silver-sodium field assisted ion exchange in soda-lime silicate and alumino-silicate glasses (MY2 and SLASY1) [P.IV,V,VII,IX]; ii) a method, based on UV photo-imprinting technique, able to realize both guiding (waveguides) and periodic (gratings)

structures in active SiO_2-GeO_2 thin film [P.II,III]; iii) ion bean irradiation on tungsten-tellurite glasses doped with Er^{3+} ions [P.I].

In Section 3.A we will recall the fundamentals of electromagnetic propagation in optical waveguides. In Section 3.B we will describe the three technologies used: ion-exchange, UV photo-imprinting and ion beam irradiation. In Sections 3.C and 3.D, respectively, measurements set-up and preliminary results on devices characterization will be presented and discussed.

3.A Electromagnetic Theory of optical waveguide

Generally, for optical waveguide we consider a structure able to confine the light inside it thank to a local variation of refractive index in comparison with that of the surrounding media. The simplest dielectric guide is the planar slab (1D) waveguide schematically illustrated in Fig. 3.1
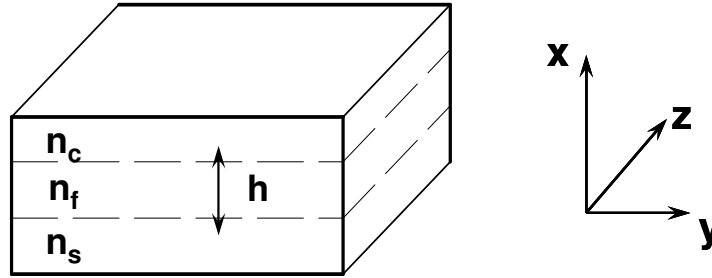
Fig. 3.1: Sketch of an "asymmetric" slab waveguide and the choice of the coordinate system. Note that the z-plane lies in the film-substrate interface.

Here, the guiding structure of thickness h has a refractive index n_f and it is sandwiched between a substrate of uniform index n_s and a cover of uniform index n_c. The light is trapped inside the waveguide if and only if $n_f > n_s$, n_c. If Ray Optics [69,70] represents a simple and intuitive model to describe the electromagnetic propagation in these kind of structures, a rigorous treatment is given by Wave Optics [70]. For more details on this well known subject, we refer to the wide literature [1,6,69]. Here we just remind that under the hypothesis of linear, homogeneous, isotropic and dielectric medium without losses, the Maxwell's equations written for the complex vector of electric and magnetic fields are, respectively:

$$\nabla \times \overline{E} = - j \omega \mu \overline{H}$$

(3.1)

$$\nabla \times \overline{H} = j \omega \varepsilon \overline{E}$$

where ε is the dielectric constant, μ the scalar magnetic permeability, $\overline{E}$ and $\overline{H}$ the electric and magnetic field having the following expression:

$$\overline{E}(x, y, z) = \overline{E}(x, y)e^{-j\beta z}$$

$$\overline{H}(x, y, z) = \overline{H}(x, y)e^{-j\beta z}$$

(3.2)

This kind of solution represents a plane wave, called *mode* of the waveguide, where β is the propagation constant along the propagation direction z [1,69]. Because the structure in Fig. 3.1 is invariant along y then $\partial/\partial y = 0$ and hence, for a TE mode ($H_y = E_z = E_x$ =0) the following equations system is verified [69]:

$$\begin{cases} H_x = -\dfrac{\beta}{\omega\mu} E_y \\[3mm] H_z = \left(\dfrac{j}{\omega\mu}\right) \dfrac{\partial E_y}{\partial x} \end{cases}$$

(3.3)

with the E_y component obeying the Helmholtz's equation

$$\frac{\partial^2 E_y}{\partial x^2} + \left(n^2 k^2 - \beta^2\right)E_y = 0$$

(3.4)

where n is the refractive index of the waveguide and $k = \omega/c = \omega\sqrt{\varepsilon_0 \mu_0}$ is the propagation constant in free space. The boundary conditions demand that E_y and $\partial E_y/\partial x$ are continuous across the waveguide boundaries at x = 0 and x = h.

For guided modes (for the others solutions we refer to [1,69]) we have

$$E_y = E_c \exp\left(-\gamma_c\left(x-d\right)\right), \; x>h \qquad (cover),$$

$$E_y = E_f \cos\left(k_f x - \phi_s\right), \; 0<x<d \qquad (waveguide), \qquad (3.5)$$

$$E_y = E_s \exp\left(\gamma_s x\right), \; x<0 \qquad (substrate).$$

where γ_i is defined as the transverse decay related to propagation constant κ_i by the relations $\kappa_i^2 = n_i^2 k^2 - \beta^2 = -\gamma_i^2$ (with $i = s,c$ in the case of substrate and cover, respectively), $\kappa_f^2 = n_f^2 k^2 - \beta^2$ (in the waveguide) with $\beta = k\, n_f \sin\theta$ is the z-component of the wave vector $\mathbf{k}\, n_f$ as shown in Fig. 3.2 [69].
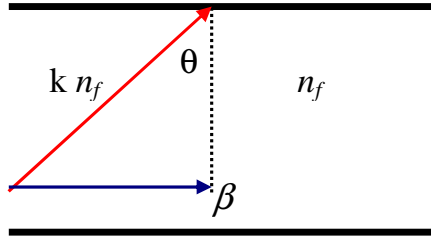

Fig. 3.2: Relation among the components of the propagation constant in a XZ plane.

 Application of the boundary conditions yields the formulas for the phase shifts:

$$\begin{cases} \tan\phi_s = \dfrac{\gamma_s}{\kappa_f} \\[2mm] \tan\phi_c = \dfrac{\gamma_c}{\kappa_f} \end{cases} \qquad (3.6)$$

and the dispersion relation:

$$\kappa_f \, h - \phi_s - \phi_c = m \, \pi \tag{3.7}$$

with m an integer defining the mode label.

Recalling the expressions of k_f and β, this last equation can be written as:

$$n_f \, h \cos \theta - \phi_s - \phi_c = m \, \pi \tag{3.8}$$

that yields to express the propagation constant β of each mode as a function of frequency ν and waveguide thickness h (*dispersion curves* [1,69]).

For a channel waveguide, able to confine the radiation in 2D dimension, there are no TE and TM modes as solutions of Maxwell's equation, but only hybrid modes.

In this case, the Marcatili's method gives an approximate solution of the problem [6].

3.B   Fabrication processes: Ion-exchange, UV photo-imprinting and ion beam irradiation techniques.

3.B.1 Ion-Exchange

3.B.1a Ion-Exchange technique: principle and advantages

For its simplicity, flexibility and low cost, ion-exchange is one of the most important technique used in the fabrication of integrated optical devices [12].

It consists in a replacement of some alkali ions originally contained in the glass matrix (usually Na^+ ions) with other ions having the same valence of the former and present in a molten salt solution where the glass is immersed. Because of the high temperature (tipically 300-400°C) at which the process occurs and concentration gradient established in proximity of the interface between glass and molten salt, Na^+ ions migrate in the solution and are replaced by cations originally contained in the salt melt, as shown in Fig.3.3.
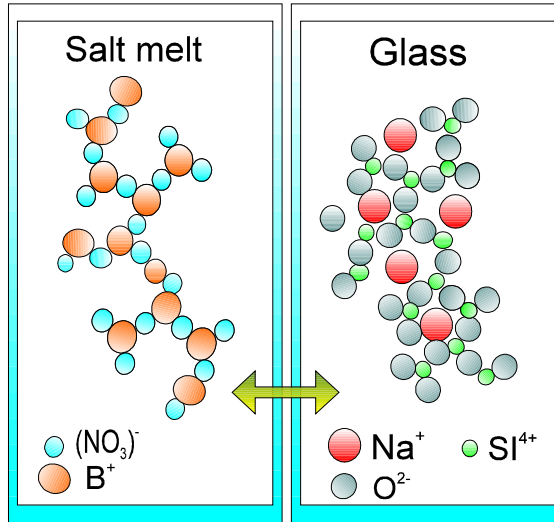
Fig. 3.3: Scheme of ion-exchange process

Due to the different size and polarizability of the ions participating in the process, the glass modifies its network locally in the exchanged regions. Generally, in ion-exchange these changes correspond to an increase of refractive index, giving rise to the formation of optical waveguides [13]. In particular, different cations (i.e. K^+, Ag^+, Tl^+, Cs^+, Rb^+,...) induce different refractive index change in the bulk glass [71]. This technique indeed presents several variations: field-assisted ion-exchange [72], field-assisted dry ion-exchange [73], inverse ion exchange [74], double ion-exchange [75], two-step ion exchange [76]. In any case the many benefits of this technology include: i) low production and materials costs; ii) low birefringence and propagation losses; iii) high compatibility with single-mode fiber [77]. Moreover, in order to increase the symmetry of the index profile (thereby improving fiber-waveguide coupling) and reduce the scattering losses, caused by the interaction between surface irregularities and propagating field in waveguide region, a burying of the guiding structure can be performed through field assisted or two-step ion-exchange processes [78].

3.B.1b Ion-Exchange technique: model.

Because of the diffusive nature of ion-exchange, the graded refractive index, induced by this process in optical devices, depends on the concentration C of incoming ions inside the glass matrix. Thereby the knowledge of this distribution gives many information on

the kind of ion-exchange occurred and on the optical properties (in term of refractive index) of the device.

Without going into details of the theory (for a more accurate description we refer to [13,79-80]), we say that, starting from the Fick's first law and expanding the continuity equation (or Fick's second law) for ionic flux, the time evolution of incoming ion concentration is derived as:

$$\frac{\partial c}{\partial t} = \frac{D_A}{1-\alpha c}\left(\nabla^2 c + \frac{\alpha(\nabla c)^2}{1-\alpha c} - \frac{e\vec{E}_{ext}}{f\,kT}\nabla c\right)$$

(3.9)

where c is the concentration of incoming ions (i.e. Ag$^+$ ions) normalized with respect to the saturated concentration; D_A and D_B are the self-diffusion coefficients of these ions and of sodium ions, respectively; $\alpha = 1 - M$ where $M = D_A/D_B$ is the ratio between these two diffusion coefficients; E_{ext} is the applied electric field; T, k, q and f are the absolute temperature, the Boltzmann's constant ($1.38 \cdot 10^{-23}$ [J/K]), the electron charge and the correlation factor (included in order to take into account the different nature of ionic mobility in diffusion and ion migration due to the electric field).

Considering the boundary conditions:

$$C(x, 0) = 0$$

(3.10)

$$C(x, t) = C_A = \text{costant}$$

in case of pure thermal ion-exchange for a slab waveguide, with $\alpha = 0$, the eq. (3.9) has the following analytical solution:

$$C(x, t) = C_A\, \text{erfc}\left\{\frac{x}{2\sqrt{D_A\,t}}\right\}$$

(3.11)

with $d = 2\sqrt{D_A\,t}$ the diffusion depth. Due to the proportionality between concentration distribution and refractive index [13], we can conclude that:

$$n(x) = n_{sub} + (\,n_{sup} - n_{sub}\,)\,erfc\left(\frac{x}{d}\right) \tag{3.12}$$

where n_{sub} is the refractive index of the bulk and n_{sup} is the surface refractive index of the planar waveguide region. When $\alpha \neq 0$, the (3.9) has not an analytic solution but only a numerical one [13]. Generally the refractive index profile is reconstructed from the knowledge of mode-index data, measured by accurate systems having a typical resolution of 2×10^{-4} and based on prism-coupling technique [6,17], applying recursive inverse Wentzel-Kramers-Brillouin (IWKB) algorithm [69,81-82]. One of the limits of this method is related to the fact that, using Gaussian or Erfc functions (the most commonly used functions to fit the effective indices measured), the IWKB fit procedure generally leads to reconstructed index profiles that do not correctly reproduce the number of modes observed experimentally. In one of our works [P.IX] we improved the accuracy of the IWKB method introducing a new expression, linear combination of two analytical functions, which is able to provide a better approximation of the solution of (3.9) for binary planar (1D) thermal ion-exchange process.

Considering the standard deviation between the exact theoretical effective indices, obtained using the Transfer-Matrix-Method (TMM) [83], and the measured ones we obtained the following results summarized in Table 3.1:

	SL1	*M3*	*IOG10*	*PER2*	*PSM1*
Erfc	$1.7\cdot10^{-3}$	$1.5\cdot10^{-3}$	$1.5\cdot10^{-3}$	$2.2\cdot10^{-4}$	$2.6\cdot10^{-4}$
Gauss.	$3.5\cdot10^{-4}$	$8.1\cdot10^{-4}$	$8.6\cdot10^{-4}$	$5.5\cdot10^{-4}$	$3.1\cdot10^{-4}$
C_{An} *Fun.*	$1.4\cdot10^{-4}$	$1.9\cdot10^{-4}$	$1.7\cdot10^{-4}$	$7.4\cdot10^{-5}$	$8.7\cdot10^{-5}$

Table 3.1: Standard deviation σ between experimental and theoretical effective index for different functions used in the reconstruction of the profiles.

As can be noted from the same table, for different silicate (**SL1**, **M3**, **IOG10**) and phosphate (**PER2**, **PSM1**) glasses, standard deviation (σ) values achieved using our function (C_{An} *Fun*) were always smaller then those obtained using Gaussian or ERFC and always comparable with the experimental error of the measured effective index values ($\sim 2 \times 10^{-4}$). These results were confirmed by other ones obtained with different ion-exchange conditions in different substrates [P.IX].

3.B.1c Ion-Exchange technique: Fabrication of channel waveguide in the case of
MY2 and SLASY1 silicate glasses.

The high content of sodium oxide in the composition of MY2 and SLASY1 silicate glasses (see Chapter 2) makes them suitable for the fabrication of channel waveguides by ion-exchange.

 In order to obtain a better confinement of the light inside the guiding structure, we selected silver-sodium ion-exchange that, among all typologies of ion-exchange, offers the highest refractive index change (Δn ~ 0.05$\div$ 0.1). Different openings (from 4μm to 10μm) in an oxidized mask, obtained following a standard photolithographic process, were used to define the exchange region.

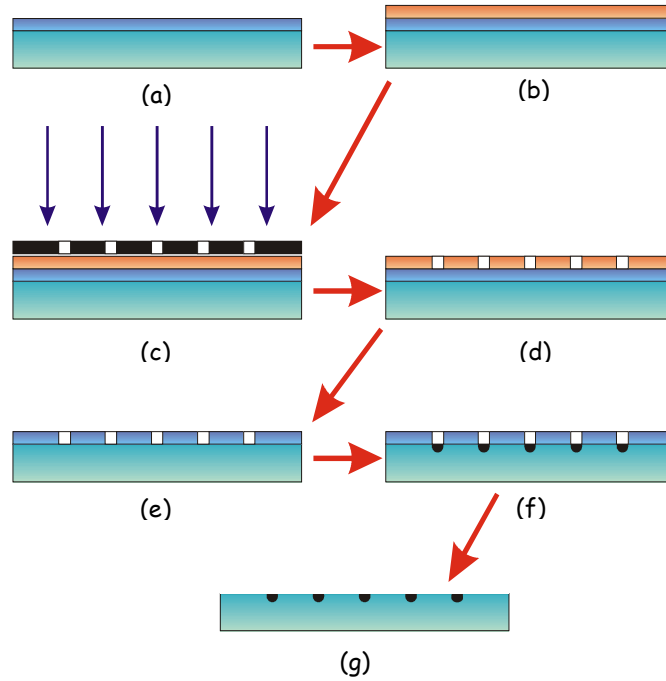Fig. 3.4 represents the fabrication steps.

Figure 3. 4 : Schematic of the channel waveguides fabrication
process in MY2 and SLASY1 glasses. From top to bottom:
(a) Ti mask deposition; (b) Photoresist deposition;
(c) Photoresist UV exposure; (d) Photoresist removal
(e) Ti etching and channel opening; (f) ion-exchange;
(g) mask removal.

The mask is obtained deposing 200 nm of titanium by RF sputtering [17]. In order to fabricate single mode channel waveguides at 1.55 µm we used a silver-sodium thermal ion-exchange. The composition of the adopted solution was 0.5 mol.% of silver nitrate ($AgNO_3$) in 99.5 mol.% of sodium nitrate ($NaNO_3$).

Before ion-exchange, in order to reduce the formation of silver clusters on glass surface, we decided to oxidize the mask in a pure sodium nitrate solution at 380 °C for 1 hour [84]. After that, we performed thermal ion-exchange at 325° C with duration of 7 min. (D_{Ag} = 5.8·10^{-3} μm^2/s) and 12 min.(D_{Ag} = 4.2·10^{-3} μm^2/s), respectively for MY2 and SLASY1 glass. At the end we removed completely the Ti mask with a second etching procedure.

Moreover, in the case of MY2 glass we operated a second step consisting in a field-assisted burial process in order to reduce the propagation losses, as indicated in Fig.3.5.
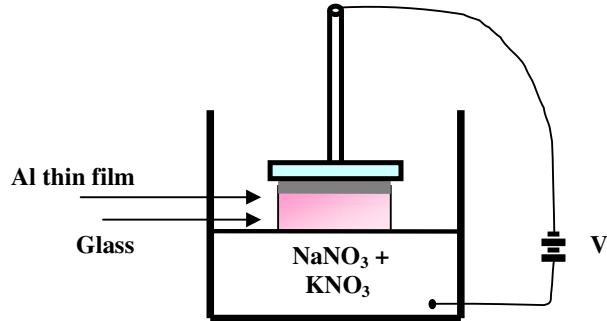

Fig.3.5 : Set-up for field-assisted burial ion-exchange

A voltage V = 300 volt was applied across the MY2 substrate of thickness 2 mm. The two electrodes were formed, respectively, by an eutectic solution of 55mol.% of $NaNO_3$ with 45mol% of KNO_3 and an aluminium oxide film obtained by thermal deposition. The thickness of the film was around 500 nm, the process temperature 285°C and the duration 30 minutes. Applying the voltage, the Ag^+ ions inside the glass go deeper and, contemporary, they are replaced by Na^+ ions near the surface with a consequent burying of the waveguide structure. Finally, to reduce the coupling losses between the fiber and the waveguide, a thermal annealing post-process can be request [85].

Proceedings in this way, for a 4μm wide channel waveguide in MY2 sample, after the burying step mentioned above, we performed a thermal annealing process with a duration of 25 minutes at the same ion-exchange temperature.

3.B.2 *UV-photoimprinting technique*

A local change at the refractive index of properly designed glasses or amorphous thin films can be performed using an UV radiation exposure. This technique may represent an attractive option in the fabrication of integrated optical components if compared with other conventional methods. In fact, it may reduce fabrication time and contemporary remove all those expensive fabrication steps such as optical photolithography patterning and chemical or physical etching.

This technology is based on a property that some materials have to undergo a permanent change in their refractive index by exposure to light radiation. This phenomenon is commonly known as *photosensitivity*. The inclusion of rare-earth elements in these materials allows to combine photorefractive and active properties and provide an effective route to the simple fabrication of integrated optical amplifiers and lasers.

3.B.2a Ge-doped glass Photosensitivity: two possible models

In 1978 photosensitivity was first observed by Hill and coworkers in a Ge-doped silica fiber that was exposed to an Ar-laser light at 488 nm launched into its core [86]. Ten years later, a transverse writing method was used by Meltz and his coworkers to photo-imprint Bragg gratings using wavelength in the range 240÷250 nm [87].

Nowadays, the most commonly used technique to write high efficiency Bragg gratings with UV radiation is the phase mask method [88].

Initially, photosensitivity was thought to be a phenomenon associated only with optical fibers having a large concentration of germanium in the core and photo-excited with 240÷250 nm ultraviolet (UV) light. Actually photosensitivity has been observed in a wide variety of crystalline and glassy materials, such as phosphate and fluoride glasses without germanium doping [89-90]. Nevertheless, for their material compatibility with optical fiber, silicate glasses or silica-germania thin films remain among the most important materials for fabrication of integrated optical devices utilizing photosensitivity. It is not yet clear the mechanism that induces an index change in these materials after an exposure to UV radiation. However, two are the most known models: the *color center model* and the *densification model*. The first one refers to the formation of Germanium-Oxygen Deficient Center (GODC) during the fabrication process of the material. In this case, because of the high-temperature reached in the fusion process of oxides, GeO_2 dissociates into the GeO molecule (in other words the Ge^{2+} center) which has higher stability at elevated temperature. Once the glass matrix is formed, this molecule breaks the tetrahedral structure of SiO_4 and contributes to form Ge-Ge or Ge-Si wrong bonds characterized by the presence of a oxygen vacancy. This kind of defects, labelled GODC, has an absorption band centered around 242 nm and are reported, schematically, in Fig. 3.6.
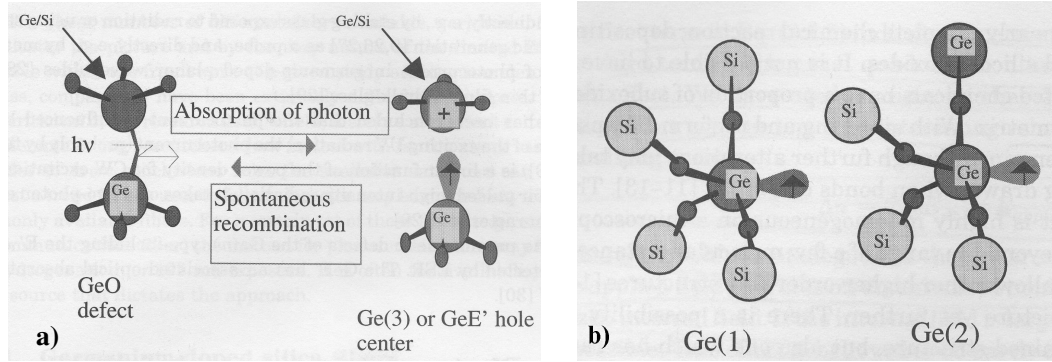
Fig.3.6: (a) mechanism of GeE' center formation; (b) defects on silica network induced by a germanium doping.

Instead of bonding to other Ge or Si atoms through a bridging oxygen, the Ge atom is bonded to Ge/Si atoms through an electron. When the material is exposed to UV radiation, the incoming photon breaks this bond and contributes to the creation of GeE' color center, releasing one electron in the glass matrix [91-92]. The mechanism of color centers formation has been demonstrated to be the first responsible of an increase on the refractive index of some amorphous materials [93]. On the other hand, another model links the breaking of Ge–e⁻–Ge/Si wrong bond to a reconfiguration of molecular structure with a possible densification (or expansion). This is the *densification model* [94]. In this model the UV radiation induces a volume change locally in the irradiated region. This last one can be associated to a density change and, hence, to a refractive index variation according to the Lorentz-Lorenz formula [22]:

$$\frac{\Delta n}{n} = \frac{\left(n^2 - 1\right)\left(n^2 + 2\right)}{6n^2}\left[-\frac{\Delta V}{V} + \frac{\Delta \alpha}{\alpha}\right] \qquad (3.13)$$

where ΔV is the change in volume, $\Delta \alpha$ is the bond polarizability. Generally, in case of silica or silicate glasses doped with germanium, the volume compaction ($\Delta V < 0$) is the dominant effect, with a consequent increase of physical density and hence of refractive index change [95].

3.B.2b   Fabrication of Bragg grating in photosensitive thin film: the Phase Mask technique

A fiber Bragg grating is a periodic perturbation of the refractive index in the core of a single mode fiber [96]. When the radiation generated by a wide band source interacts with grating, only that belonging to a narrow band (~ 0.3 nm) is reflected back without any perturbation on the rest of wavelengths as illustrated in Fig. 3.7.
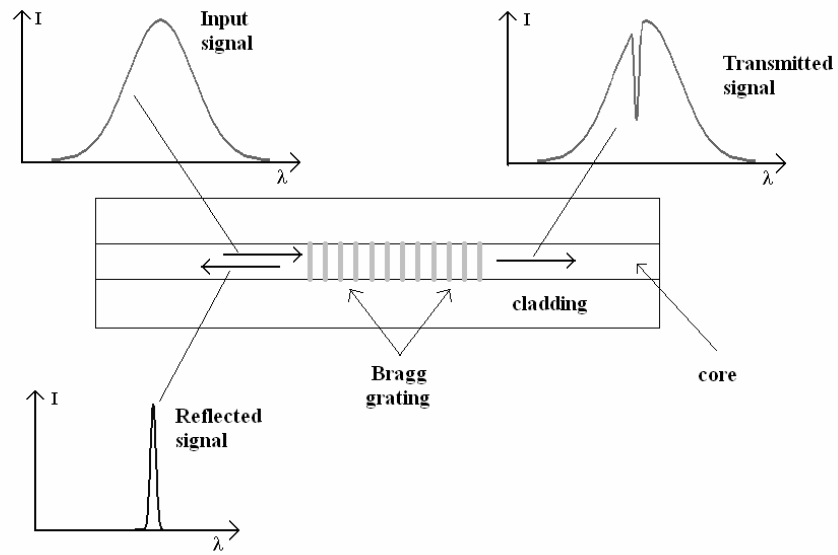
Fig.3.7: Working principle of a Bragg grating. It reflects the input radiation

in a narrow band while it is completely transparent at the other wavelengths.

If Λ is the period of the grating, the resonance condition is expressed by the well known *Bragg condition*:

$$\lambda_{Bragg} = 2\, n_{eff}\ \Lambda \tag{3.14}$$

where λ_{Bragg} is commonly called Bragg wavelength and n_{eff} is the effective refractive index of the fiber. For this property, Bragg gratings have gained attention not only for

fiber applications but also in integrated optics. For instance the possibility to write Bragg gratings with high reflectivity on both sides of an active channel waveguide, may represent a key step in the development of integrated laser sources. In fact they are an attractive alternative to mirrors in order to realise a resonant cavity.

Among all techniques actually adopted to fabricate Bragg gratings, that of phase mask is simple and efficient.

It uses a diffractive optics element, the phase mask, to spatially modulate the UV laser beam [97]. In Figure 3.8 is reported a schematic cross section of an ideal phase mask.
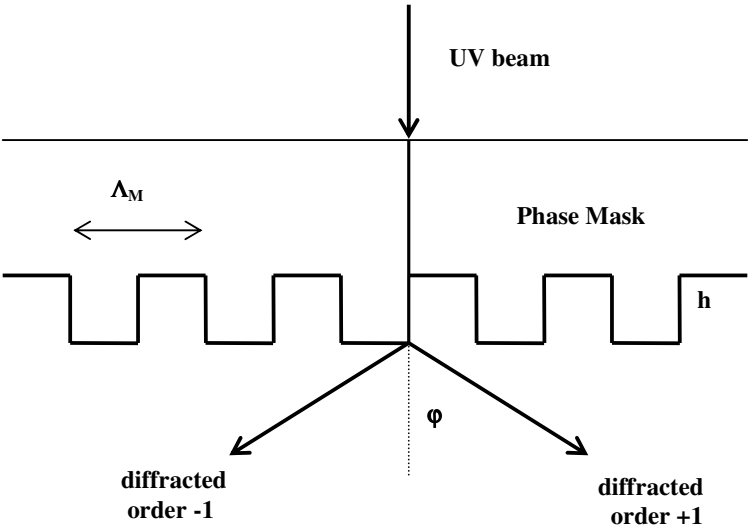
Fig. 3.8: Laser beam diffraction by a phase mask

The mask, constituted by a substrate of silica glass with an etched surface-relief grating (period Λ_M and thickness h) on one side the other side, is placed in close proximity to the surface of the photorefractive layer. As diffraction grating the mask splits the incident beam in multiple diffracted waves of *m* order according to the equation [96-97]

$$\Lambda_M \, \sin \varphi_m = m \, \lambda_{UV} \tag{3.15}$$

where λ_{UV} is the wavelength of the UV beam. The angles φ_m are measured with respect to the incident light. Considering only the orders ± 1, as shown in Fig. 3.8, these two beams overlap to each other and form an interference figure having a period Λ given by:

$$\Lambda = \frac{\lambda_{UV}}{2 \sin \varphi_{\pm 1}} \qquad (3.16)$$

From (3.15) and (3.16), we can conclude that the periodicity Λ of the interference pattern do not depend on the wavelength of the writing radiation but only from that of the mask, as reported below:

$$\Lambda = \frac{\Lambda_M}{2} \qquad (3.17)$$

At last, from the Bragg condition, it is possible to know the Bragg wavelength as a function of Λ_M value:

$$\lambda_{Bragg} = n_{eff} \; \Lambda_M \qquad (3.18)$$

Another advantage offered by this technique is the possibility to use laser sources with low spatial and temporal coherence. On the contrary, the main drawback in the phase mask use is related to the fact that the period of the grating is univocally determined by that of the mask (see eq. (3.17)) and hence, in order to change the Bragg wavelength (see eq. (3.18)), we need to change the mask.

3.B.2c Imprinting of the Bragg gratings and channel waveguides on SiO_2-GeO_2 thin film

Thin film with $75SiO_2$-$25GeO_2$ (molar %) composition, doped with 0.27 mol% each of Er_2O_3 and Yb_2O_3, were deposited onto vitreous silica substrates by RFMS (Radio Frequency Magnetron Sputtering) technique [59]. In order to improve the adhesion of the active films, the substrates were cleaned inside the RF sputtering deposition

chamber by removing some atomic layers just before starting the deposition procedure. We used a sputtering process that does not require a target sintered on purpose, as we simply placed pieces of GeO_2, metallic ytterbium and metallic erbium onto a 4" silica target. The residual pressure, before deposition, was about $2x10^{-5}$ Pa. During the deposition process the substrates were not heated. The sputtering was carried out with Ar gas at a pressure of 0.7 Pa and an applied RF power of 150 W, with a reflected power of 18 W. The deposition time was 4 h 15 min, producing a film with a thickness of about 3.35 µm. In order to reduce the losses of the sputtered film, we employed an annealing process in air at the temperature of 600°C for 6 hours.

In our experiments, in order to obtain a highly-efficient waveguide Bragg grating on the SiO_2-GeO_2 thin film we adopted a phase mask with central period $\Lambda_M = 1070$ nm and a KrF (Krypton-Fluore) excimer laser (Lambda Physics Compex 110) operating at 248 nm as UV light source

To fabricate 2D guiding structure in SiO_2-GeO_2 thin film we used a direct imprinting technique based on a single step replica of an intensity mask. In comparison with direct writing methods, which require a relative movement between focused laser beam and sample [98], direct imprinting offers the benefit that no movable part is present in the exposure system and, hence, the only limitations are related to the amount and the stability of the incident light. Since the first demonstrations of UV photo-induced channel waveguides [18], germano-silicate glasses have played an important role in this field, due to the high time durability for the refractive index changes induced and low scattering losses. The possibility to achieve significant positive refractive index change in RF sputtered SiO_2-GeO_2 thin film has been demonstrated [99]. Moreover no sensitization procedures are required to improve the photo-refractive properties of the material. The amplitude mask used in photo-imprinting technique was produced in our laboratories following two steps: a) deposition of Ti film, with thickness of 200 nm, through RF sputtering on pure silica substrate; b) patterning of the Ti film by copying an e-beam written photolithographic mask containing various sets of straight channels with different openings, from 4 to 10 µm. We could have used the original

photolithographic mask, but we preferred to make a copy in order to avoid any possible damage that excimer laser can produce on it during repeated exposures. The Ti mask was placed in contact with the SiO_2-GeO_2 thin film and then exposed to the KrF excimer laser source operating at 248 nm, as shown in Fig.3.9. Pulse fluency was kept low (36 mJ/cm^2) to prevent damage to the mask. Repetition rate was set at 10 Hz while cumulative exposure dose was 20 kJ/cm^2. Examination of the mask after exposure revealed that there was not damage and further tests confirmed the repeatability of the experiment. The sample was then cut at 15 mm length, and the edges were optically polished.
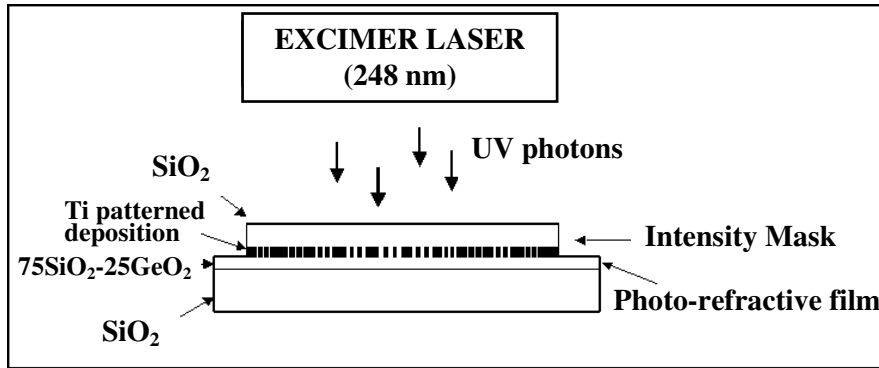

Figure 3.9: Schematic representation of the experimental set-up for photo-imprinting of channel waveguides in SiO_2-GeO_2 thin film.

3.B.3 Ion beam irradiation

3.B.3a Ion beam irradiation: principle and advantages

Ion beam irradiation is a commonly used technique to change the chemical, physical and optical properties of a wide range of materials like crystals, glasses and semiconductors. When an energetic ion (i.e.: N^+, Ne^+, Cu^+, Er^+, H^+) impinges on a material it will loose energy due to interaction with target electrons (electronic stopping) or by colliding with target nuclei (nuclear stopping) [22]. In particular, in the irradiated region, the material changes can induce a corresponding change on the refractive index with the possibility to define an optical waveguide. The order and sign of the index

change depends strongly on the material used and varies highly with the ion-beam dose (number of particles per unit volume). On the other hand, the depth of the waveguide under the surface depends on the energy of the bombarding particles and also on the material type [22]. The main advantage of this fabrication method is the possibility of controlling both the depth and the lateral distribution of the implanted ions. The former is done by choosing the appropriate ion energy, the latter by using a suitable mask. With this technique it had been demonstrated the possibility to obtain channel waveguides in crystal or amorphous materials, like LiF and $LiNbO_3$ [100-101] or silica and phosphate glasses [64-66].

3.B.3b Ion Beam Irradiation: Fabrication of channel waveguide in Er^{3+} -doped tellurite glasses.

We decided to use this technique to fabricate channel waveguide in Er^{3+} doped tellurite glasses. In fact we had previously studied a set of tungsten-sodium-tellurite glasses (WNT) and their spectroscopic properties are reported in [49]. Er^{3+} doped tellurite glasses are one of the most attractive materials for the development of C and L band amplifiers due to their large stimulated emission cross-sections, broad emission bandwidth (up to 60 nm) and low phonon energy.

If many papers refer on (1D) slab waveguide obtained in this glass formulation [49,102], nevertheless the fabrication of 2D guiding structures in Er^{3+}-doped tellurite glasses appears to be still a challenge. Because of their rather low chemical durability, these glasses can be damaged during some steps of typical channel waveguide fabrication processes like, for instance, ion-exchange.

The composition of the glass material used for our experiments is: TeO_2 (60 mol.%): WO_3 (25 mol.%): Na_2O (mol.%) doped with Er_2O_3 (0.5 mol.%). The waveguide fabrication procedure was as follows.

Double side polished silicon slices were glued to each other with a proper spacer to ensure a gap of about 25 μm, then polished in cross-section to a thickness of about 75 μm. The silicon mask was placed in front of the sample in order to define a multimode

channel waveguide, as illustrated in Fig.3.10(a). The dimensions of the substrate were 10 mm × 10 mm × 4 mm. The irradiations were carried out with a 1.5 MeV N$^+$ collimated beam from a Van de Graaff accelerator (available at Research Institute for Technical Physics and Materials Science –Budapest) with normal incidence on the sample. By defocusing the ion beam with a magnetic quadrupole and using the silicon mask slices, the waveguide stripes have been realized in the glass with different doses corresponding to 0.5, 1.0, 2.0 and 4.0 x 10^{16} ions/cm^2. The guiding structures so obtained are shown in Fig.3.10(b). The image was taken with Nikon Coolpix 4500 camera connected through a phase contrast microscope.
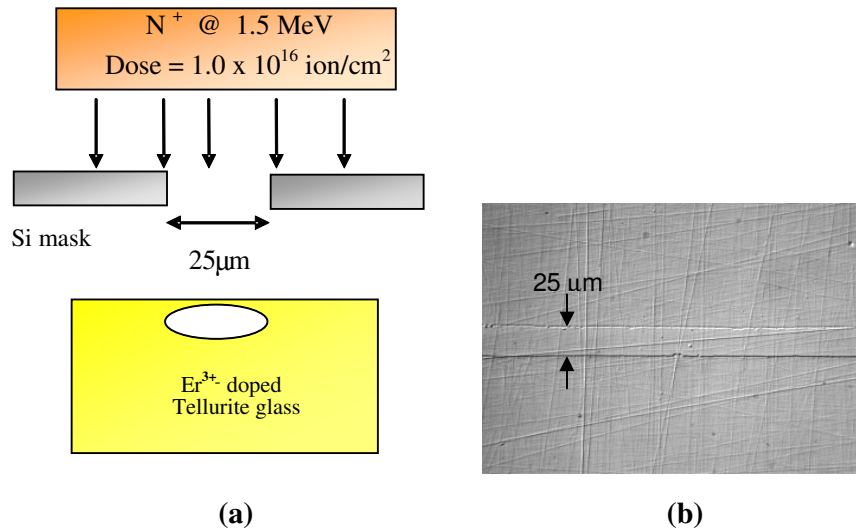

(a)   **(b)**

Fig.3.10: (a) Schematic representation of channel waveguide fabrication by ion beam bombardment; (b) Channel waveguide top-viewed observed at microscope

.

3.C Measurements

3.C.1 Losses and Near-Field measurements.

The technique used for loss measurement (typically, propagation loss and coupling loss) is schematically illustrated in Fig.3.11. It consists of two consecutive measures, respectively in configuration (a) and (b).
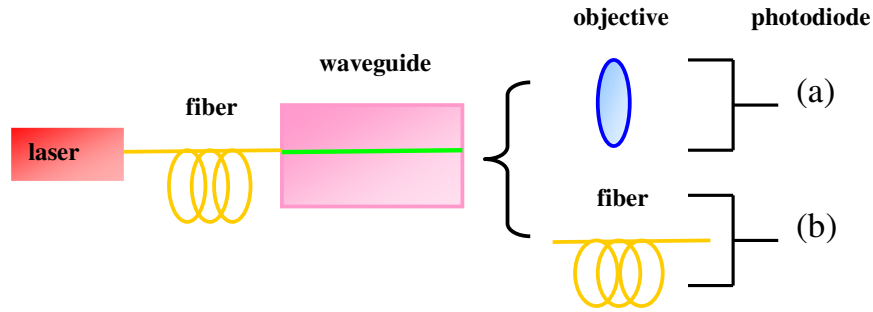

Fig. 3.11: Schematic representation of the experimental set-up
for losses measurement in channel waveguides.

The output power measured by the photodiode according to scheme (a) is

$$P(a) = P_{in} \, \alpha_c \, \alpha_p \, T_o \tag{3.19}$$

while, in configuration (b), we have:

$$P(b) = P_{in} \, \alpha_c \, \alpha_p \, \alpha_c \, T_f \tag{3.20}$$

where P_{in} is the power from the input fiber, α_c and α_p are the fiber-waveguide coupling coefficient and propagation loss coefficient, respectively. T_o and T_f are the transmission coefficient for the objective and the fiber at the output section. Because P_{in}, T_o and T_f are known, by solving the system represented by equations (3.19) and (3.20) it is possible to knowledge the α_c and α_p coefficients and, hence, the propagation and the

coupling losses for the device. The measurements were performed at 1.3 μm to avoid the absorption of Er^{3+} ions around 1.5 μm.

In the output section of Fig. 3.11(a), using a calibrate Hamamatsu C-1000 Vidicon camera instead of the photodiode, we were able to get the near field image of the channel waveguide.

3.C.2 Gain measurement.

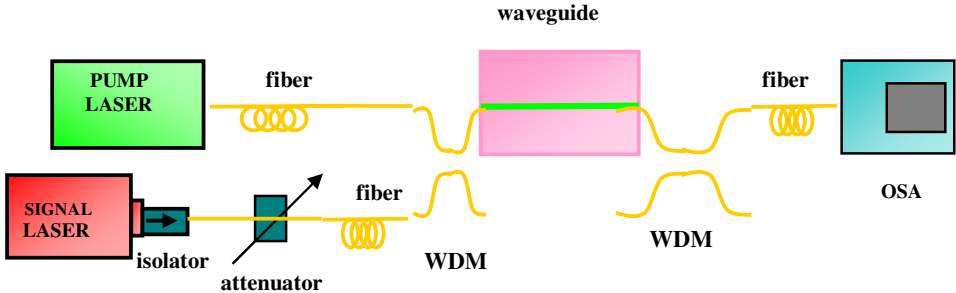For gain measurement, we adopted the following set-up:

Fig. 3. 12: Set-Up for gain measurement.

The source is a laser diode tunable between 1490 and 1600 nm. An isolator avoids the problems related to the undesired reflections, while the attenuator reduces the power at the input of the waveguide. The pump laser is a laser diode working at 976 nm. An input WDM combines the laser signal with that coming from the pump, while an output WDM works in dual mode. The amplified signal is directed to a spectrum analyzer (OSA) for processing. A matching gel between the fiber and the waveguide is introduced to improve and stabilize the couplings.

We define net optical gain as follows:

$$G\left(dB\right) = 10\log_{10}\left(\frac{P_{OUT} - P_{ASE}}{P_{IN}}\right) \tag{3.21}$$

where P_{ASE} is the noise power generated by the amplifier, P_{IN} is the signal input and P_{OUT} is the signal output power.

3.D Results

3.D.1 MY2 and SLASY1 ion-exchanged channel waveguides

For a 4µm wide channel waveguide in MY2 sample we obtained $\alpha_p \leq 0.6$ dB/cm and $\alpha_c \leq 0.8$ dB while, for a 5 µm wide channel waveguide in SLASY1 sample, we measured values of $\alpha_p \leq 0.4$ dB/cm and $\alpha_c \leq 0.7$. In Fig. 3.13 is shown the effect of the annealing process on the vertical and lateral dimensions of the field in the case of MY2 sample.
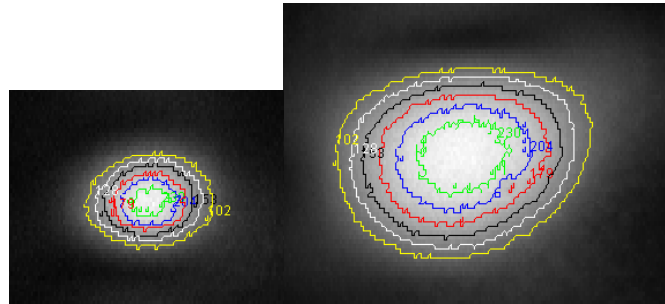

Fig. 3.13: Near Field intensity for a 4 µm channel waveguide in MY2 glass: (a) before annealing; (b) after annealing. The colours represent the intensity level of the field respect to the max: 0.9 (green line); 0.8 (blue line); 0.7 (red line); 0.6 (black line); 0.5 (white line); 0.4 (yellow line).

An increase of field dimension was obtained, improving the symmetry of the field and reducing the mismatch with the fiber. In particular, before the annealing, the near field dimensions measured were 4.1 µm × 2.9 µm while, after this step, the dimensions were of 7.9 µm × 5.9 µm at wavelength of 1550 nm. The waveguide was single mode in depth and multimode in transversal (lateral) direction.

For the 5 μm single mode channel waveguide obtained in SLASY1 sample, the measured dimensions of near field were 4.8 μm × 3.0 μm.

For what concern the optical gain, fixing for P_{IN} a reference value of -31 dBm, in a 4 μm MY2 channel waveguide we obtained an output power, $P_{o,PUMP\ OFF}$, of   -46.08 dBm when the pump laser was off. Switching on the pump, we progressively increased its power until to reach the maximum value of 170 mW. In this case the corresponding value measured for the output power, $P_{o,PUMP\ ON}$, was -29.54 dBm as reported in Fig. 3.14.

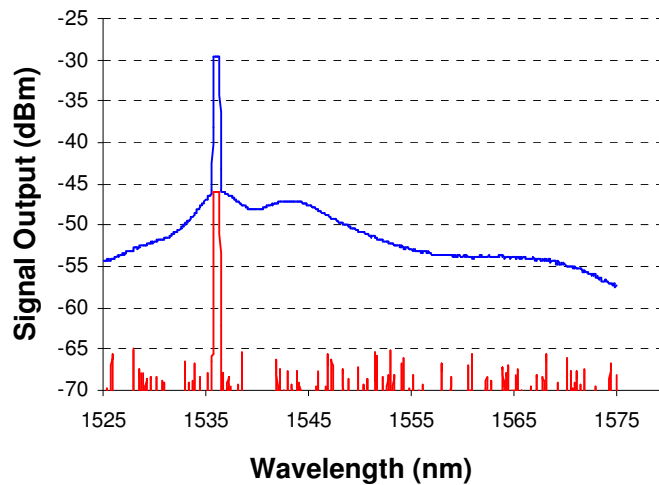**Fig. 3.14**: Dynamic of output power in two different cases: (a) pump off (red line); (b) pump on (blue line).

Refering to same figure, the *signal enhancement* is defined as the ratio of the output signal when the pump laser is on to that when it is off. In MY2 glass waveguide we obtained a value for the *sig. enh.* equal to 16.5 dB, while for the net gain we obtained a maximum value at 1536 nm of 1.5 dB as in Fig.3.15.
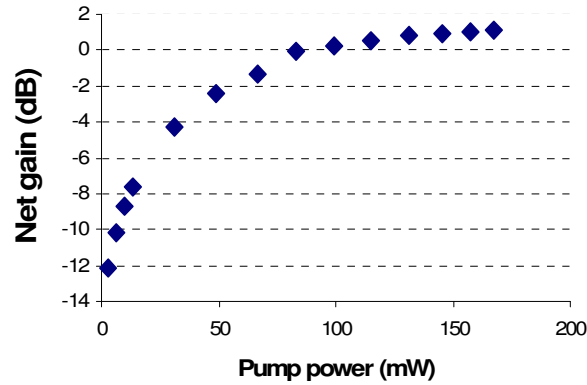
Fig. 3.15: Net gain (dB) as a function of pump power (mW)

The length of waveguide was around 2 cm. From this waveguide, which exhibited a positive net gain, by using two properly designed high reflective mirrors or fiber gratings, it is potentially possible to obtain a waveguide laser at 1536 nm.

No net gain was observed in SLASY1 sample, but only a signal enhancement of 2 dB/cm. The reason of this is, actually, under investigation. Possible explanations can be related to the following two phenomena: (a) the shift of the absorption Yb^{3+} peak at pump wavelength caused by the high concentration of aluminium oxide that can reduce the pump efficiency for this substrate; (b) an high value for co-operative up-conversion that may occur in these glass formulations [103].

3.D.2 Photorefractivity, grating and waveguide imprinting in SiO_2-GeO_2 thin film.

The SiO_2-GeO_2 thin film, fabricated by RF sputtering, as reported in § 3.B.2c, constituted a slab waveguide. The effective refractive indices of the waveguide modes of this structure were measured by a semi-automatic instrument based on dark-line spectroscopy and prism coupling technique [17], having a precision of 2×10^{-4}. The glass substrate had a refractive index of 1.495 at 633 nm while the waveguide supported 4 modes supported at this wavelength and only 1 at 1.55 µm. Propagation losses measured at 633 nm were 0.8 dB/cm and at 1300 nm less than 0.3 dB/cm, confirming the good optical quality of the annealed films. In order to evaluate the effect of UV exposure on the refractive index of the film, we irradiated the sample with single pulse fluency of 36 mJ/cm^2 and repetition rate of 10 Hz. After each irradiation the effective

index values of the supported modes at 633 nm were measured in TE polarization, and much care was taken to repeat the measurement in the same position on the waveguide, to avoid errors due to film inhomogeneities. The results obtained are reported in Fig. 3.16.
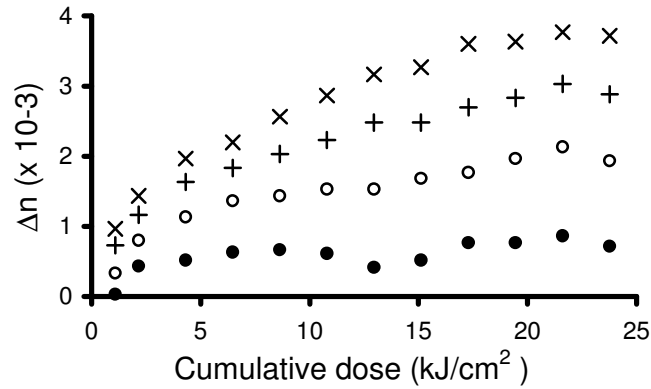

Fig. 3.16 UV light induced changes, with increasing cumulative dose, of the effective index values of the four TE modes supported by the waveguide at 633 nm

Significative changes on the effective index values of the four TE modes were detected. The effect increases with the irradiated energy and saturates at 22 kJ/cm^2 of cumulative exposure. The refractive index value of the film can be calculated with a fitting procedure from the values of the four effective indices. A maximum index change of 3.8 10^{-3} was obtained. Such a positive value of the index change is high enough to achieve a good lateral confinement of the radiation: channel waveguides direct imprinting on similar films is therefore possible.

Moreover, in order to test the contribution of the UV photo-induced volume densification to index change, we placed a thin metallic wire on the surface of the sample. The wire, with diameter of 150 μm, had a masking function respect to UV radiation. After an exposure to excimer laser with irradiated energy of 16.2 kJ/cm^2, the wire was removed and the exposed area around the masked region was scanned with a Tencor P-10 profilometer. The result of this measurement is reported in Fig. 3.17.
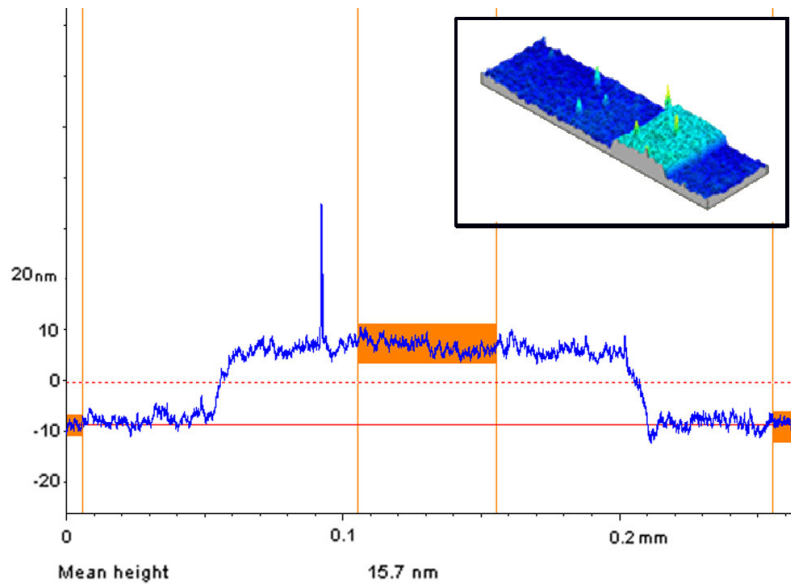
Figure 3.17 Profilometer scan of the sample surface after the UV-exposure around the masked region.

The step profile shown in Fig. 3.17 corresponds to the not-irradiated region of the SiO_2-GeO_2 thin film covered by the wire, while the surrounding regions are irradiated. A decrease of 16 ± 2 nm of the thickness of the film was measured, confirming that a densification of the material occurred as a result of UV irradiation [95]. The contribution of volume densification on refractive index change of the film calculated by Lorentz-Lorenz formula was in good agreement with that experimentally measured. This simple experiment demonstrated the validity of the compaction/densification model for UV exposed SiO_2-GeO_2 thin film.

The photo in Fig. 3.18 shows the operation of a highly-efficient waveguide Bragg grating, that was photo-induced by using the phase mask method. We used 36 mJ/cm^2 pulse fluency with a 10 Hz pulse repetition rate and the total irradiated energy density was 2.5 kJ/cm^2
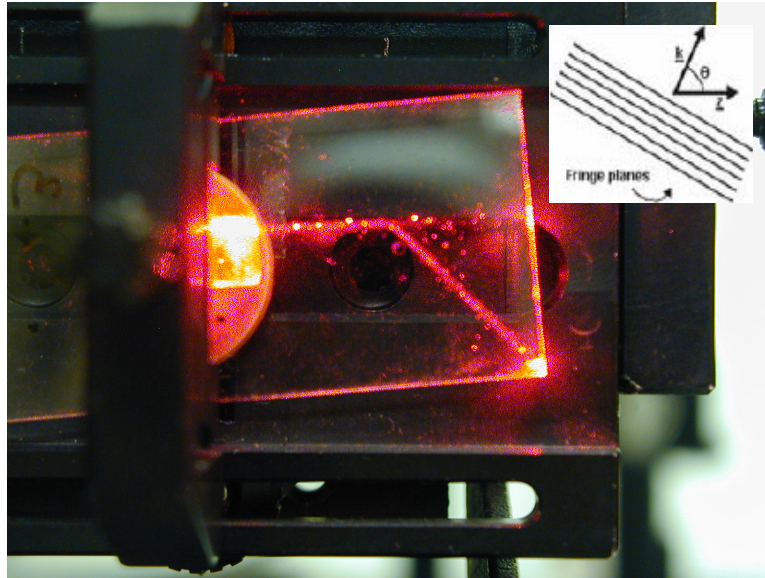
Figure 3.18 Deflection of a prism coupled He-Ne guided beam produced by a highly efficient photo-induced Bragg

In order to make evident the effect of the grating we prism-coupled a He-Ne laser beam (λ = 633 nm) into the a guided mode.

When the angle θ between the direction of the coupled light $\underline{z}$ and the grating vector $\underline{k}$ (see inset in the Fig. 3.18) satisfies the Bragg condition cos (θ)=$\lambda/n_e \Lambda$, where n_e is the modal effective index, the guided light is deflected symmetrically from the fringe planes. Spatial displacement, with a near 100% efficiency is achieved in a small distance ($\approx$ 1 mm) along the propagation direction.

Hence, the possibility to fabricate high efficiency Bragg grating applications has been demonstrated in a SiO_2-GeO_2 thin film.

After a cumulative exposure of 20 kJ/cm^2 for waveguide imprinting, examining the sample with a phase contrast microscope, the series of channels waveguides appear to be well defined and of good quality. In order to check surface quality and possible densification effects due to the UV exposure, a profilometer scan of the surface was performed in direction transversal to the light-induced channel. In Fig.3.19 a densification effect of 16 ± 2 nm in correspondence of a 7 µm mask openings is shown. The inset shows a 3D scan of a portion of the film including three optical channels. The compaction of the film produced by the exposure can be clearly seen.
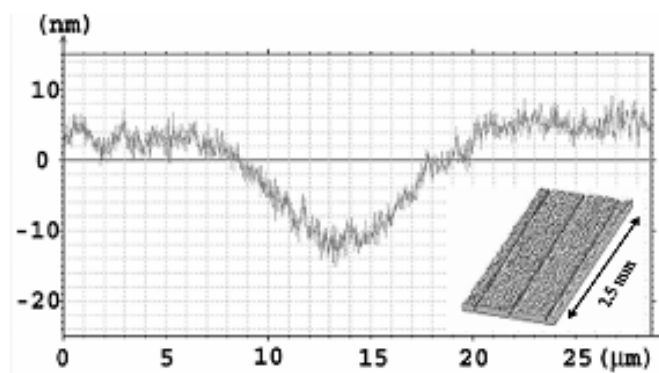
Figure 3.19 Profilometer scan of the film surface in direction transversal to a channel waveguide obtained by UV imprinting through a 7 µm wide opening of an intensity mask

We then measured the near-field of these channel waveguide at 1550 nm focusing the channel output onto the Vidicon camera, using a 0.8 NA (Numerical Aperture) microscope objective. For a 7 µm wide channel, the intensity distribution is shown in Fig. 3.20
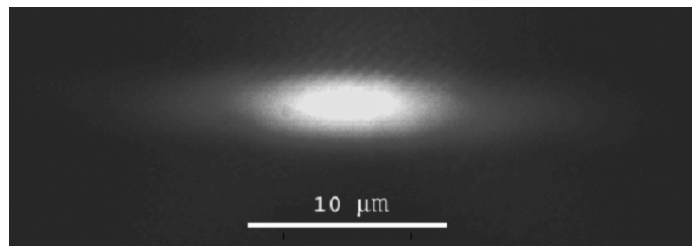
Figure 3.20 Measured near field distribution at 1550 nm of a channel waveguide obtained by UV imprinting through a 7 µm wide opening.

All the imprinted channel waveguides were single mode at 1550 nm. The field is strongly asymmetric because the difference between the substrate and the film refractive indices (in the vertical direction) is about one order of magnitude higher than that induced by the UV exposure (in the transversal direction).

Propagation and fiber-to-waveguide coupling losses were both directly measured at 1300 nm, in order to avoid the absorption band of the $^4I_{13/2} \rightarrow {}^4I_{15/2}$ transition of the erbium ions. Propagation losses were less than 0.3 dB/cm, namely equal to those previously measured in unexposed planar waveguide. This means that the exposure process did not affect the intrinsically low scattering losses of the material. Coupling losses from a standard communication fiber into a 7 μm waveguide were 3.1 ± 0.2 dB, but this rather large value could be expected due to the waveguide asymmetry.

Hence, the fabrication of low loss channel waveguides in SiO_2-GeO_2 thin film was demonstrated.

The final target of this research activity on photorefractive and active thin films will be the implementation of an "all photo-written" laser device where both the waveguide and the Bragg gratings are obtained through UV photo-imprinting (see Fig.3.21).
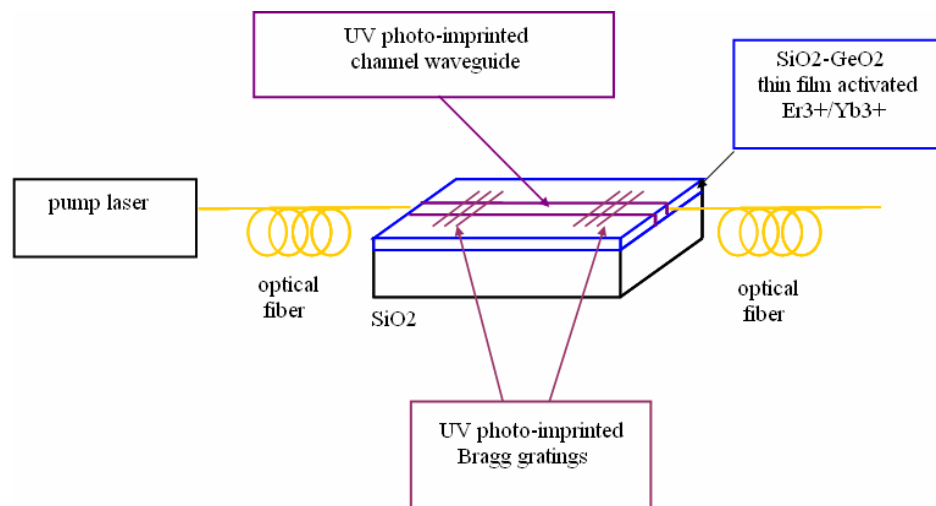

Fig. 3.21 The design of an integrated all photo-induced waveguide laser in SiO_2-GeO_2 thin film activated with Er^{3+}/Yb^{3+}.

3.D.3   Characterization of ion beam irradiated channel waveguide in tellurite glass

In order to test the effect of the nitrogen implantation on the refractive index of Er^{3+} - doped tungsten tellurite glass, a 633 nm laser beam was coupled into the waveguide with a multimode optical fiber MM 50/125. The output signal was focused onto a Vidicon camera with a 20× microscope objective (NA = 0.4). The result is shown in Fig. 3.22.
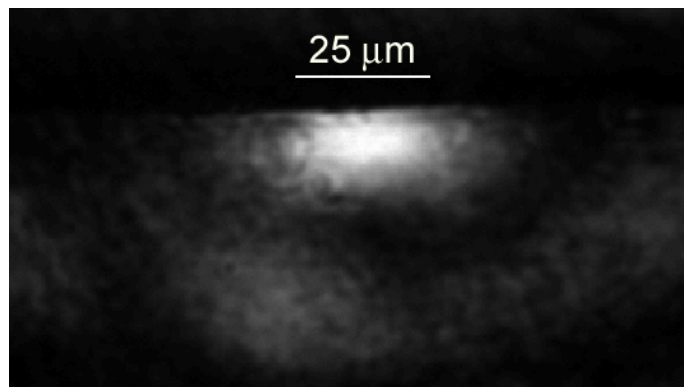
Figure 3.22 Measured near field distribution at 633 nm of a channel waveguide obtained by ion beam irradiation through a 25 μm wide opening.

The light is indeed confined both in vertical and in lateral direction around the implanted region. This fact implies that, due to the N^+ irradiation [22], there was an increase of the refractive index ($\Delta n > 0$) of the Er^{3+} -doped glass. The best guiding channels in terms of 2D light confinement were obtained with a dose of 1.0×10^{16} ions/cm^2. The length of the waveguides was 7mm with a depth around 10 μm. A 2D guiding effect was also confirmed observing the well confined green up-conversion emission obtained pumping the Er^{3+} ions at 980 nm along the waveguide, as shown in Fig. 3.23.
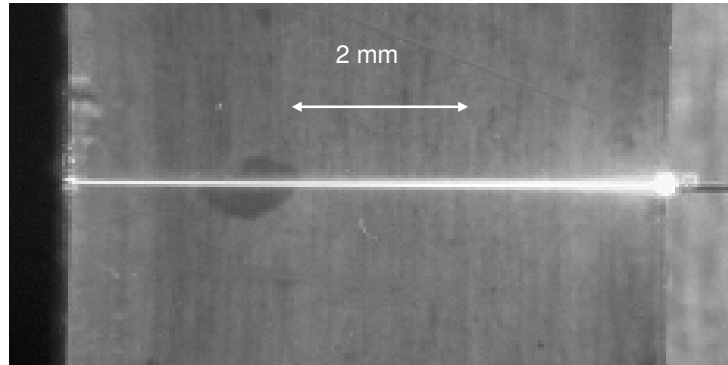
Fig. 3.23: Confined green up-conversion of Er[3+] ions along the waveguide after 980 nm pumping.The end-fire coupled input fiber is visible on the right side.

Some generic considerations can be reported on ion beam irradiation induced refractive index change Δn. The relationship between Δn and the defects-dependent parameters is described by Lorentz-Lorenz equation reported in (3.13). Generally the dominant factors of ion implantation on refractive index is usually due to the nuclear damage process. For many materials this corresponds to a volume expansion ($\Delta V > 0$) with a consequence decrease of physical density and hence to a reduced refractive index. In such cases the ion-implanted region acts as an optical "barrier" with a negative refractive index change [22,66]. In our case, instead, the measured near field profile (see Fig.3.22 and Fig. 3.23) is similar to that of a "conventional" waveguide. This suggests that, due to the ionization processes induced by the implanted nitrogen ions (i.e. rearrangements of substrate bonds and chemical interactions with the substrate), a positive refractive index change occurs. Collating these considerations to equation (3.13), it means that the contributions coming from bond polarizability $\Delta\alpha$ have a greater effect on the refractive index change than that of ΔV, counteracting and overcoming possible volume expansions [22]. Further works are in progress to get a better understanding of the waveguide formation mechanism in these glasses.

We believe that the possibility to fabricate channel waveguides in Er[3+] activated tellurite glasses open the door to the development of a new class of waveguide lasers and amplifiers working in L-band.

CHAPTER 4 *Structures: Microsphere Lasers*

During the past decade applied research has targered on a reduction in size of optoelectronics devices making use of structures with a strong light confinement for both classical and non-linear optical applications. Optical microcavities fully respond to these requisites and found many applications in telecommunications and sensing [23]. In particular high quality factor microcavities can be obtained with microspheres fabricated in silicate and phosphate glasses. In dielectric microspheres light can be trapped in whispering gallery modes (WGMs) [104] and guided in a thin ring, close to the equator, due to successive total internal reflections.

Historically, WDMs were first observed in the gallery of the cupola of St Paul's Cathedral in London: a whisper spoken close to the wall can be heard all the way along the gallery, some 42 m to the other side. Lord Rayleigh was the first to identify the refocusing effect of the curved surface as the sound travels along the gallery; he also suggested that such modes of the electromagnetic field could find some applications due to the extreme confinement of the field [105].

Due to the properties mentioned above, dielectric glass microspheres doped with Rare-Earths (Er^{3+} and Yb^{3+}, principally) are ideal candidate for the realization of microlasers where very low threshold, high pump efficiency and very narrow emission linewidth are expected [24-25,106]. In this chapter we will demonstrate the realization of microspherical lasers based on Er^{3+}or Er^{3+}/Yb^{3+} doped silicate (B05, IOG10) and phosphate (IOG2) glasses, optically pumped at 1480 nm, with emission around 1550 nm. The chapter is organized as follows. In Section A two theoretical models are presented in order to describe the electromagnetic propagation in microspherical resonator. While the former concerns the geometric optics approximation, the latter is based on wave optics and Maxwell's equations (in the formulation of vector and scalar Debye's potentials [107-111]). Section B introduces numerical simulations, developed in MATLAB code, in order to have a better comprehension of the WGMs and field distributions. Section C takes into account the problem of light coupling into a microsphere [112-113] and finally Section D focuses on the experimental set-up developed for the laser measurements and results. Three Appendices on the theoretical part conclude this chapter.

4.A Electromagnetic Theory of Microspherical Resonators

The microresonators discussed in this chapter are dielectric spherical resonators (DSRs). A first approximate, but more intuitive, approach to study the light propagation in this kind of structure is given by use of the geometrical optics. Then, a rigorous electromagnetic field analysis is represented by solving the Maxwell's equations in spherical coordinates. An analogous procedure can be adopted to describe the electric and magnetic field components for others types of microresonators such as microdisks or microrings. The only difference is that, in this last case, a cylindrical coordinates system must be considered [1]

4.A.1 Qualitative Description of WGMs: the Geometrical Optics Approach

Considering a dielectric microsphere of radius **a** with refractive index *N*, the WGMs can be viewed as light rays that propagate by total internal reflections if

$$\theta_i > \theta_c = \arcsin\left(\frac{1}{N}\right) \tag{4.1}$$

where θ_i is the incidence angle of the light ray makes with respect to the normal to the spherical surface and θ_c is the critical angle corresponding to total internal reflection. In this way, for large microspheres (**a** >> λ), the propagation of the light radiation can be considered confined in the region between the sphere surface and an internal spherical surface (signed in dots) whose tangents correspond to the critical angle, as illustrated in Fig.4.1.
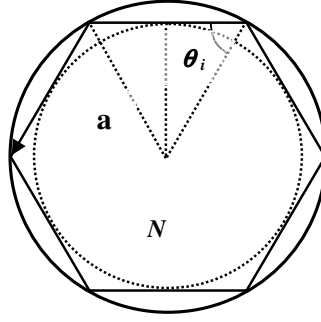
Fig.4.1: Total internal reflection for the light rays in correspondence of the surface of the microsphere. If the optical path equals the integer number of wavelengths, a resonance occurs.

In one round trip, for a high number of reflections, the distance that the WGM traverses is approximately $2\pi\,a$. If this distance is exactly equal to an integer number of wavelengths, a standing wave may occur. This is the resonance condition that can be expressed as

$$2\pi a \approx l\frac{\lambda_0}{N} \tag{4.2}$$

where l is an integer number, λ_0 is the wavelength in the vacuum and λ_0/N is the wavelength in the medium. Letting x be a dimensionless size parameter defined as below

$$x = \frac{2\pi a}{\lambda_0} = \frac{l}{N} \tag{4.3}$$

the resonance condition becomes

$$N\,x \approx l \tag{4.4}$$

The integer l, introduced as the number of wavelengths in the circumference, can be also related to the angular momentum of a circulating photon. In fact, if the momentum of the single photon is expressed by

$$\left| \vec{p} \right| = \hbar k = \hbar \, \frac{2 \pi N}{\lambda_0} \tag{4.5}$$

then the angular momentum of the photon can be written as

$$\left| \vec{L} \right| = \left| \vec{r} \times \vec{p} \right| = \hbar \, \frac{2 \pi a N}{\lambda_0} = \hbar \, N \, x \approx \hbar \, l \tag{4.6}$$

where $\vec{r}$ is the radial vector. Thus, the integer number l can be related to the angular momentum of the radiation.

We adopt a spherical coordinate system as shown in Fig.4.2 (r for radial direction, ϕ for the azimuthal direction and θ for the polar direction):
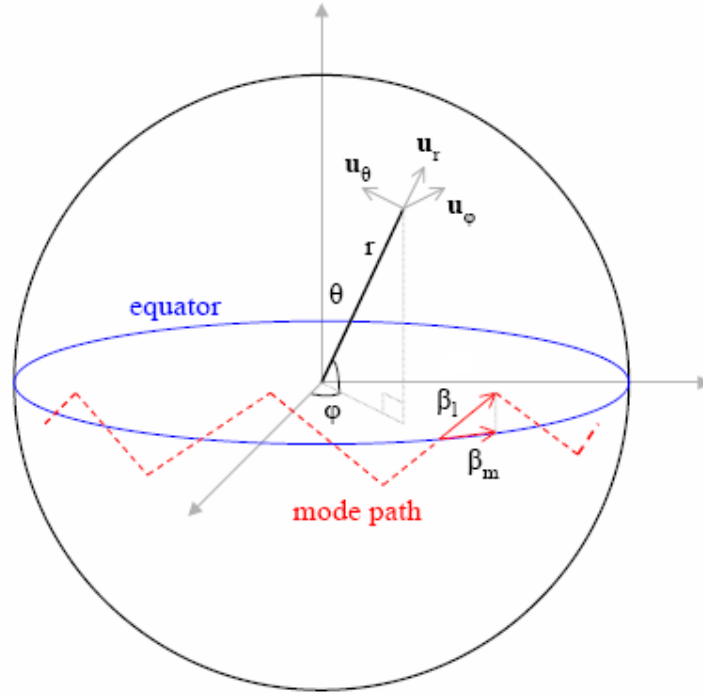

Fig. 4.2 Spherical coordinate system for Whispering-Gallery Modes and modes propagation along the surface of the sphere

Following the ray optics model, the modes can be thought to propagate along a ziz-zag paths around the equator (see Fig.4.2). With mode number l, two other integer numbers, n and m, characterize a WGM mode in microspherical resonators. The radial mode

number n is equal to the number of field maxima in the direction along the radius of the sphere, while m is the azimuthal mode number. For any fixed value of l, $|m| \leq l$. The value $l - m + 1$ equals the number of field maxima in the polar direction. Different values of m imply that the modes travel in zig-zag paths with different inclinations with respect to the equatorial plane. When $m = l$, (the "fundamental mode"), the inclination is the smallest while, for $m = 0$ the inclination is 90° with respect to the equatorial plane. All modes with the same l and n have the same resonant wavelength regardless of the value of m. The wave number β_l, in the direction of the zig-zag path, is defined as

$$\beta_l = \sqrt{\frac{l\,(l+1)}{a}}$$

(4.7)

where a is the ray of the sphere (see Appendix A and [112]).

The projection of β_l onto the equator is commonly referred to as the "propagation constant" of the mode:

$$\beta_m = \frac{m}{a}$$

(4.8)

4.A.2 Analytic model for a dielectric spherical resonators: solution of the Maxwell equations

It is well known that, for an isotropic linear and homogeneous dielectric medium, without any electromagnetic sources inside it, the expressions of electric $\vec{E}$ and magnetic $\vec{H}$ fields can be expressed by the following equations

$$\vec{E} = \frac{\nabla \times \nabla \times \vec{A}}{j\omega\mu\varepsilon} - \frac{1}{\varepsilon}\nabla \times \vec{F}$$

(4.9)

$$\vec{H} = \frac{\nabla \times \nabla \times \vec{F}}{j\omega\mu\varepsilon} + \frac{1}{\mu}\nabla \times \vec{A}$$

where $\vec{A}$ and $\vec{F}$ are called, respectively, *magnetic vector potential* and *electric vector potential* [70].

These two vector potentials satisfy the system equations [109]:

$$\nabla \times \nabla \times \vec{A} - k^2 \vec{A} = -j\omega\mu\varepsilon \nabla \phi^m$$

$$(4.10)$$

$$\nabla \times \nabla \times \vec{F} - k^2 \vec{F} = -j\omega\mu\varepsilon \nabla \phi^e$$

with ϕ^m and ϕ^e two scalar functions and k the propagation constant.

In a spherical coordinates system, the electromagnetic field can be expressed as a superposition of TE and TM modes, making a suitable choice for the magnetic $\vec{A}$ and electric $\vec{F}$ vector potentials:

$$\vec{A} = A_r \, \hat{r}$$
$$\vec{F} = F_r \, \hat{r}$$

$$(4.11)$$

in which the scalar components A_r and F_r do not satisfy the Helmholtz's scalar equation, because generally:

$$\nabla^2 A_r \neq \left(\nabla^2 \vec{A} \right)_r$$

Knowing these scalar components it is possible to obtain the vector expressions for the electromagnetic field, using eq. [4.9]. In fact one can demonstrate that, starting from the knowledge of its radial components, the electromagnetic field is univocally defined (see Appendix B) [110,114].

Then, to determinate the field solutions of this problem, we will follow the next logic steps:

- Determination of A_r and F_r expressions;

- Determination of the general field components from the knowledge of A_r and F_r;

- Determination of TE and TM components;

- Characteristic equations for TE and TM modes.

To determinate the expressions of A_r and F_r components, one proceeds from the general equations of vector potentials [4.9].

For instance, in the case of the magnetic vector potential, developing the first of equations [4.10], we get:

$$\nabla\nabla\cdot\vec{A} - \nabla^2\vec{A} - k^2\vec{A} = -j\omega\mu\varepsilon\nabla\phi^m \tag{4.12}$$

that, projected along the tern $(\hat{r}, \hat{\theta}, \hat{\varphi})$, gives an equations system along the polar and azimuthal components, respectively [109]:

$$\frac{\partial^2 A_r}{\partial r\,\partial\theta} = -j\omega\mu\varepsilon\,\frac{\partial\phi^m}{\partial\theta}$$

$$\tag{4.13}$$

$$\frac{\partial^2 A_r}{\partial r\,\partial\varphi} = -j\omega\mu\varepsilon\frac{\partial\phi^m}{\partial\varphi}$$

From these ones it follows immediately the solution:

$$\phi^m = -\frac{1}{j\omega\mu\varepsilon}\frac{\partial A_r}{\partial r} \tag{4.14}$$

Then, substituting the eq. (4.14) in the radial components of eq. (4.12), we obtain [109]

$$\frac{\partial^2 A_r}{\partial r^2} + \frac{1}{r^2\,sen\theta}\frac{\partial}{\partial\theta}\left(sen\theta\,\frac{\partial A_r}{\partial\theta}\right) + \frac{1}{r^2\,sen^2\theta}\frac{\partial^2 A_r}{\partial\varphi^2} + k^2 A_r = 0 \tag{4.15}$$

that, it is easy to verify, can assume the synthetic form:

$$\left(\nabla^2 + k^2\right)\frac{A_r}{r} = 0 \tag{4.16}$$

This is the scalar Helmholtz's equation having A_r/r as solution. The same procedure can be applied to electric vector potential $\vec{F}$. Hence, one infers that the electromagnetic fields can be expressed starting from the following choice for vector potentials:

$$\vec{A} = A_r \, \hat{r} = r \psi^m \, \hat{r}$$
$$\vec{F} = F_r \, \hat{r} = r \psi^e \, \hat{r}$$

(4.17)

where $\psi^{e,m}$ are, respectively, *electric* and *magnetic scalar potentials* (also called *Debye potentials*) [107,111] which satisfy the homogeneous scalar Helmholtz's equation $(\nabla^2 + k^2)\psi = 0$, with $\psi = \psi^{e,m}$.

In a spherical coordinates system, the solutions of this equation (for all mathematical steps we refer to Appendix A) are expressed by eq. (A.19) and then radial components of vector potentials, A_r e F_r, can be written as:

$$A_r = r \psi(r,\theta,\phi) = r \psi_1 \, j_l(k\,r) P_l^m (\cos\theta)\cos(m\varphi) = F_r$$

(4.18)

valid for $r < a$, where a is the ray of the sphere, l and m are angular and azimuthal mode numbers previously introduced, j_l *(kr)* corresponds to the first order spherical Bessel function and P_l *^{m}(cosθ)* are Legendre functions (see Appendix C) [115]. Hence, for instance, the magnetic vector potential $\vec{A}$ assumes the form:

$$\vec{A} = r \psi(r,\theta,\phi) \, \hat{r} = r \psi_1 \, j_l(k\,r) P_l^m (\cos\theta)\cos(m\varphi) \, \hat{r}$$

(4.19)

where

$$\begin{cases} k = k_0, \ r > a \\ k = k_0 \, n_s, \ r \leq a \end{cases}$$

(4.20)

In case of $r > a$, the first order spherical Bessel functions j_l *(kr)* must be substituted by the second order spherical Hankel functions $h_l^{(2)}$ *(k₀ r)*, which represent the evanescent

tail of the field immediately outside the spherical microresonator. This discontinuity can be resolved as reported at the end of Appendix A. In this way, knowing the A_r and F_r components, we are able to express the general field components.

2nd STEP: Determination of general field components from the knowledge of A_r and F_r;

Considering the first equation of system (4.9), it can be written as below:

$$\vec{E} = \frac{\nabla \times \nabla \times \vec{A}}{j\omega\mu\varepsilon} - \frac{1}{\varepsilon}\nabla \times \vec{F} = \frac{\nabla\nabla \cdot \vec{A} - \nabla^2 \vec{A}}{j\omega\mu\varepsilon} - \frac{1}{\varepsilon}\nabla \times \vec{F} \qquad (4.21)$$

In a spherical coordinates system, remembering the expressions (4.17) for vector potential $\vec{A}$, the first term at the second member of eq. (4.21) can be developed as follows:

$$\nabla\nabla \cdot \vec{A} - \nabla^2 \vec{A} = \left(\frac{\partial^2}{\partial r^2} + k^2\right)A_r \, \hat{r} + \frac{1}{r}\frac{\partial^2}{\partial r \partial \theta}A_r \, \hat{\theta} + \frac{1}{r\sin\theta}\frac{\partial^2}{\partial r \partial \varphi} \, A_r \, \hat{\varphi} \qquad (4.22)$$

On the other hand, from the curl of electric vector potential $\vec{F}$ we have:

$$\nabla \times \vec{F} = \frac{1}{r^2 \, sen\theta}\begin{vmatrix} \hat{r} & r\hat{\theta} & r\sin\theta \, \hat{\varphi} \\ \frac{\partial}{\partial r} & \frac{\partial}{\partial \theta} & \frac{\partial}{\partial \varphi} \\ F_r & 0 & 0 \end{vmatrix} = \frac{1}{r\sin\theta}\frac{\partial F_r}{\partial \varphi}\hat{\theta} - \frac{1}{r}\frac{\partial F_r}{\partial \theta}\hat{\varphi} \qquad (4.23)$$

So writing, the electric field as:

$$\vec{E} = E_r \, \hat{r} + E_\theta \, \hat{\theta} + E_\varphi \, \hat{\varphi} \qquad (4.24)$$

and substituting the equations (4.22) and (4.23) in (4.21), we obtain:

$$
\left\{
\begin{array}{l}
E_r = \dfrac{1}{j\omega\mu\varepsilon}\left(\dfrac{\partial^2}{\partial r^2} + k^2\right)A_r \\[4ex]
E_\theta = \dfrac{1}{j\omega\mu\varepsilon r}\dfrac{\partial^2 A_r}{\partial r \partial \theta} - \dfrac{1}{\varepsilon r \sin\theta}\dfrac{\partial F_r}{\partial \varphi} \\[4ex]
E_\varphi = \dfrac{1}{j\omega\mu\varepsilon r \sin\theta}\dfrac{\partial^2 A_r}{\partial r \partial \varphi} + \dfrac{1}{\varepsilon r}\dfrac{\partial F_r}{\partial \theta}
\end{array}
\right.
\qquad (4.25)
$$

that are the general expressions for electric field components, in a spherical coordinates system, as a function of vector potential radial components A_r e F_r. In the same way, it is possible to evaluate the magnetic field components that are reported below:

$$
\left\{
\begin{array}{l}
H_r = \dfrac{1}{j\omega\mu\varepsilon}\left(\dfrac{\partial^2}{\partial r^2} + k^2\right)F_r \\[4ex]
H_\theta = \dfrac{1}{j\omega\mu\varepsilon r}\dfrac{\partial^2 F_r}{\partial r \partial \theta} + \dfrac{1}{\mu r \sin\theta}\dfrac{\partial A_r}{\partial \varphi} \\[4ex]
H_\varphi = \dfrac{1}{j\omega\mu\varepsilon r \sin\theta}\dfrac{\partial^2 F_r}{\partial r \partial \varphi} - \dfrac{1}{\mu r}\dfrac{\partial A_r}{\partial \theta}
\end{array}
\right.
\qquad (4.26)
$$

The equations shown in these two last systems are, formally, the same reported in [109].

3rd STEP: Determination of TE and TM components;

The case of TE modes

When considering TE modes, the radial component of magnetic vector potential $\vec{A}$ is zero, $A_r = 0$. Thus, for a TE mode the systems [4.25] and [4.26] become

$$
\begin{cases}
E_r = 0 \\[2mm]
E_\theta = -\dfrac{1}{\varepsilon\, r \sin\theta}\dfrac{\partial F_r}{\partial\varphi} \\[4mm]
E_\varphi = +\dfrac{1}{\varepsilon\, r}\dfrac{\partial F_r}{\partial\theta} \\[4mm]
H_r = \dfrac{1}{j\omega\mu\varepsilon}\left(\dfrac{\partial^2}{\partial r^2}+k^2\right)F_r \\[4mm]
H_\theta = \dfrac{1}{j\omega\mu\varepsilon\, r}\dfrac{\partial^2 F_r}{\partial r\,\partial\theta} \\[4mm]
H_\varphi = \dfrac{1}{j\omega\mu\varepsilon\, r \sin\theta}\dfrac{\partial^2 F_r}{\partial r\,\partial\varphi}
\end{cases}
\tag{4.27}
$$

The system [4.27] shows how the polar and azimuthal components of electric field are related to the radial component of electric vector potential $\vec{F}$.

Inside the microsphere (medium 1), this radial component can be written as

$$
F_{1r} = r\,F_l^{\,m}(r,\theta,\varphi) = r\,A_1\,j_l(k\,r)\,P_l^{\,m}(\cos\theta)\cos(m\varphi)
\tag{4.28}
$$

while, outside the microsphere (medium 2), the expression (4.28) becomes

$$
F_{2r} = r\,F_l^{\,m}(r,\theta,\varphi) = r\,A_2\,h_l^{\,(2)}(k_0\,r)\,P_l^{\,m}(\cos\theta)\cos(m\varphi)
\tag{4.29}
$$

where A_1 and A_2 are constant amplitude (crest) factors and $j_l\,(kr)$ and $h_l^{\,(2)}(k_0\,r)$ are the first order spherical Bessel and Hankel functions, respectively. By substituting these two last expressions in the system (4.27), it is possible to calculate all the components of the electric and magnetic field for a TE mode. In fact, remembering the expression of

the first order derivate for j_l function defined in eq. (C2) [see Appendix C], one can write that :

$$\frac{\partial F_{1r}}{\partial r} = A_1 P_l^m (\cos\theta)\cos(m\varphi)\left[(l+1)\, j_l(k\,r) - k\,r\, j_{l+1}(k\,r)\right]$$

(4.30)

$$\frac{\partial^2 F_{1r}}{\partial r^2} = A_1 P_l^m (\cos\theta)\cos(m\varphi)\left\{k\,(l+1)\, j_l^{'}(k\,r) - \left[k\, j_{l+1}(k\,r) + k^2\, r\, j_{l+1}^{'}(k\,r)\right]\right\}$$

(4.31)

Adopting the (C3) expression written for the $l+1$ order spherical Bessel function $j_{l+1}(k\,r)$, we get

$$j_{l+1}^{'}(k\,r) = j_l(k\,r) - \frac{l+2}{k\,r}\, j_{l+1}(k\,r)$$

(4.32)

Substituting the eq. (C2) and (4.32) in (4.31), we obtain

$$\frac{\partial^2 F_{1r}}{\partial r^2} = A_1 P_l^m (\cos\theta)\cos(m\varphi)\left\{l\,(l+1)\frac{j_l(k\,r)}{r} - k^2\, r\, j_l(k\,r)\right\}$$

(4.33)

So, for a TE mode, the radial component of the magnetic field inside the microsphere can be expressed as

$$H_{1r} = \frac{1}{j\omega\mu\varepsilon}\left(\frac{\partial^2}{\partial r^2} + k^2\right)F_{1r} = \frac{l\,(l+1)\, A_1 P_l^m (\cos\theta)\, \cos(m\varphi)}{j\omega\mu\varepsilon}\frac{j_l(k\,r)}{r}$$

On the other hand, the polar and azimuthal components of the magnetic field in the case of a TE polarized WGM are given, respectively, by

$$H_{1\theta} = \frac{1}{j\omega\mu\varepsilon r}\frac{\partial^2 F_{1r}}{\partial r\partial\theta} = \frac{1}{j\omega\mu\varepsilon r}\frac{\partial}{\partial r}\left[rA_1\, j_l(k\,r)P_l^{m^{'}} (\cos\theta)(-\sin\theta)\cos(m\varphi)\right]=$$

$$= -\frac{A_1 P_l^{m^{'}} (\cos\theta)(\sin\theta)\cos(m\varphi)}{j\omega\mu\varepsilon r}\left[j_l(k\,r) + k\,r\, j_l^{'}(k\,r)\right]$$

$$H_{1\varphi} = \frac{1}{j\omega\mu\varepsilon r\sin\theta} \frac{\partial^2 F_{1r}}{\partial r\partial\varphi} = \frac{1}{j\omega\mu\varepsilon r\sin\theta} \frac{\partial}{\partial r} \Big[-r A_1 j_l(k r) P_l^m(\cos\theta) m \sin(m\varphi) \Big]$$

$$= -\frac{m A_1 P_l^m(\cos\theta) \sin(m\varphi)}{j\omega\mu\varepsilon r\sin\theta} \Big[j_l(k r) + k r j_l'(k r) \Big]$$

Finally, recalling the equation (C3), we can write the field components of a TE mode, inside the spherical microresonator, in the form:

$$\begin{cases}
E_{1r} = 0 \\[2mm]
E_{1\theta} = \dfrac{m}{\varepsilon \sin\theta} A_1 j_l(k r) P_l^m(\cos\theta) \sin(m\varphi) \\[3mm]
E_{1\varphi} = -\dfrac{1}{\varepsilon} A_1 j_l(k r) P_l^{m\,'}(\cos\theta)(\sin\theta)\cos(m\varphi) \\[4mm]
H_{1r} = \dfrac{l(l+1) A_1 P_l^m(\cos\theta) \cos(m\varphi)}{j\omega\mu\varepsilon} \dfrac{j_l(k r)}{r} \\[4mm]
H_{1\theta} = -\dfrac{A_1 P_l^{m\,'}(\cos\theta)(\sin\theta)\cos(m\varphi)}{j\omega\mu\varepsilon r} \Big[k r j_{l-1}(k r) - l j_l(k r) \Big] \\[4mm]
H_{1\varphi} = -\dfrac{m A_1 P_l^m(\cos\theta) \sin(m\varphi)}{j\omega\mu\varepsilon r\sin\theta} \Big[k r j_{l-1}(k r) - l j_l(k r) \Big]
\end{cases} \qquad (4.34)$$

where $P_l^{m\,'}(\cos\theta)$ is the first order derivate of Legendre function made in respect of its argument $\cos\theta$. To obtain the same field components in the surrounding medium ($r > a$), it is enough to substitute the spherical Bessel function j_l *(kr)* with second order spherical Hankel function $h_l^{(2)}$ *(k_0 r)*.

The case of TM mode

For the TM modes, the radial component of electric vector potential $\vec{F}$ is zero, $F_r = 0$.
Thus, for a TM mode the systems (4.25) and (4.26) assume the form

$$
\begin{cases}
E_r = \dfrac{1}{j\omega\mu\varepsilon}\left(\dfrac{\partial^2}{\partial r^2} + k^2\right)A_r \\[2mm]
E_\theta = \dfrac{1}{j\omega\mu\varepsilon r}\dfrac{\partial^2 A_r}{\partial r\partial\theta} \\[2mm]
E_\varphi = \dfrac{1}{j\omega\mu\varepsilon r\sin\theta}\dfrac{\partial^2 A_r}{\partial r\partial\varphi} \\[4mm]
H_r = 0 \\[2mm]
H_\theta = +\dfrac{1}{\mu r\sin\theta}\dfrac{\partial A_r}{\partial\varphi} \\[2mm]
H_\varphi = -\dfrac{1}{\mu r}\dfrac{\partial A_r}{\partial\theta}
\end{cases}
\tag{4.35}
$$

Proceeding similarly to the case of Te mode, inside the microsphere, the field
components of a TM mode can be written as below

$$
\begin{cases}
H_{1r} = 0 \\[2mm]
H_{1\theta} = -\dfrac{m}{\mu\sin\theta}A_1\,j_l(kr)P_l^m(\cos\theta)\sin(m\varphi) \\[2mm]
H_{1\varphi} = \dfrac{1}{\mu}\,A_1\,j_l(kr)P_l^{m'}(\cos\theta)(\sin\theta)\cos(m\varphi) \\[4mm]
E_{1r} = \dfrac{l(l+1)A_1 P_l^m(\cos\theta)\cos(m\varphi)}{j\omega\mu\varepsilon}\dfrac{j_l(kr)}{r} \\[2mm]
E_{1\theta} = -\dfrac{A_1 P_l^{m'}(\cos\theta)(\sin\theta)\cos(m\varphi)}{j\omega\mu\varepsilon r}\left[kr\,j_{l-1}(kr)-l\,j_l(kr)\right] \\[2mm]
E_{1\varphi} = -\dfrac{mA_1 P_l^m(\cos\theta)\sin(m\varphi)}{j\omega\mu\varepsilon r\sin\theta}\left[kr\,j_{l-1}(kr)-l\,j_l(kr)\right]
\end{cases}
\tag{4.36}
$$

It is worth noticing that the systems (4.34) and (4.36) correspond to those reported in [116] without constant factors.

4th STEP: Characteristic equations for TE and TM modes ;

Resonance frequencies are determined by imposing the continuity conditions of the tangential components of the electric and magnetic fields at the surface of the microsphere:

$$\hat{r} \times \vec{E}_1 \times \hat{r} = \hat{r} \times \vec{E}_2 \times \hat{r}$$

$$\hat{r} \times \vec{H}_1 \times \hat{r} = \hat{r} \times \vec{H}_2 \times \hat{r}$$

(4.37)

where $\vec{E}_1$, $\vec{E}_2$ and $\vec{H}_1$, $\vec{H}_2$ are internal and external electric and magnetic fields, labelled with 1 and 2, respectively.

Hence, for what concern the characteristic (or the eigenvalue) equations, the boundary conditions (4.37) must be employed.

Inside the microsphere, the tangential component of the electric field is

$$\hat{r} \times \vec{E}_1 \times \hat{r} = \frac{1}{r^2 \, sen\theta} \begin{vmatrix} \hat{r} & r\,\hat{\theta} & r\sin\theta\,\hat{\varphi} \\ 1 & 0 & 0 \\ E_{1r} & r\,E_{1\theta} & r\sin\theta\,E_{1\varphi} \end{vmatrix} \times \hat{r} =$$

(4.38)

$$= \left(E_{1\theta}\,\hat{\varphi} - E_{1\varphi}\,\hat{\theta} \right) \times \hat{r} = - E_{1\theta}\,\hat{\theta} - E_{1\varphi}\,\hat{\varphi}$$

where $E_{1\theta}$ and $E_{1\varphi}$ are expressed by the second and the third equations of system (4.34)
In the same way, outside the sphere we can write:

$$\hat{r} \times \vec{E}_2 \times \hat{r} = - E_{2\theta}\,\hat{\theta} - E_{2\varphi}\,\hat{\varphi}$$

(4.39)

where, for the polar and azimuthal components of the electric field outside the sphere, the following expressions subsist:

$$E_{2\theta} = -\frac{1}{\varepsilon_0 \, r \sin\theta} \frac{\partial F_{2r}}{\partial \varphi} = \frac{m}{\varepsilon_0 \, \sin\theta} \, A_2 \, h_l^{(2)}(k_0 \, r) P_l^m (\cos\theta) \sin(m\varphi)$$

(4.40)

$$E_{2\varphi} = +\frac{1}{\varepsilon_0 \, r} \frac{\partial F_{2r}}{\partial \theta} = -\frac{1}{\varepsilon_0} \, A_2 \, h_l^{(2)}(k_0 \, r) P_l^{m'} (\cos\theta)(\sin\theta) \cos(m\varphi)$$

Comparing the equations (4.38) and (4.39) and using eq. (4.34) and eq. (4.40), we get:

$$\frac{1}{\varepsilon} A_1 \, j_l(k \, r) \left[-\frac{m}{\sin\theta} P_l^m (\cos\theta) \sin(m\varphi) \hat{\theta} + P_l^{m'} (\cos\theta) \sin\theta \, \cos(m\varphi) \, \hat{\varphi} \right] =$$

$$= \frac{1}{\varepsilon_0} A_2 \, h_l^{(2)}(k_0 \, r) \left[-\frac{m}{\sin\theta} P_l^m (\cos\theta) \sin(m\varphi) \hat{\theta} + P_l^{m'} (\cos\theta) \sin\theta \, \cos(m\varphi) \hat{\varphi} \right]$$

and eliminating the common terms, it is possible to write the continuity condition for tangential components of the electric field in the case of a TE mode:

$$\frac{1}{\varepsilon} A_1 \, j_l(k \, r) = \frac{1}{\varepsilon_0} A_2 \, h_l^{(2)}(k_0 \, r)$$

(4.41)

In order to obtain the characteristic equation for the TE modes in a DSR, it remains to express the continuity condition for the magnetic field at the spherical surface. As we have just done for the components of the electric field, from the second equation of system (4.37) we get, respectively:

$$\hat{r} \times \vec{H}_1 \times \hat{r} = \frac{A_1}{j\omega\mu\varepsilon r} \left[P_l^{m'} (\cos\theta) \sin\theta \, \cos(m\varphi) \hat{\theta} + \frac{m}{\sin\theta} P_l^m (\cos\theta) \sin(m\varphi) \hat{\varphi} \right] \cdot$$

$$\cdot \left[k \, r \, j_{l-1}(k \, r) - l \, j_l(k \, r) \right]$$

99

$$\hat{r} \times \vec{H}_2 \times \hat{r} = \frac{A_2}{j\omega\mu\varepsilon_0 r} \left[P_l^{m'}(\cos\theta)\sin\theta\cos(m\varphi)\hat{\theta} + \frac{m}{\sin\theta} P_l^m(\cos\theta)\sin(m\varphi)\hat{\varphi} \right] \cdot$$
$$\cdot \left[k_0\, r\, h_{l-1}^{(2)}(k_0\, r) - l\, h_l^{(2)}(k_0\, r) \right]$$

Equalizing these two expressions and eliminating the common terms, we obtain the continuity condition for the magnetic components of a TE mode

$$\frac{1}{\varepsilon} A_1 \left[k\, r\, j_{l-1}(k\, r) - l\, j_l(k\, r) \right] = \frac{1}{\varepsilon_0} A_2 \left[k_0\, r\, h_{l-1}^{(2)}(k_0\, r) - l\, h_l^{(2)}(k_0\, r) \right] \tag{4.42}$$

Combining the equations (4.41) and (4.42), we have

$$\frac{k\, r\, j_{l-1}(k\, r) - l\, j_l(k\, r)}{j_l(k\, r)} = \frac{k_0\, r\, h_{l-1}^{(2)}(k_0\, r) - l\, h_l^{(2)}(k_0\, r)}{h_l^{(2)}(k_0\, r)} \tag{4.43}$$

Finally, from equation (4.43), it is possible to write the characteristic equation for a TE mode in a DSR:

$$n_s \frac{j_{l-1}(n_s\, k_0\, a)}{j_l(n_s\, k_0\, a)} = \frac{h_{l-1}^{(2)}(k_0\, a)}{h_l^{(2)}(k_0\, a)} \tag{4.44}$$

obtained imposing $r = a$ at the surface of the sphere. This equation gives the positions of the resonances. In the microsphere $k = n_s\, k_0 = n_s\, 2\pi/\lambda$ while, outside the microsphere, $k = k_0$ because we suppose that the surrounding medium is air. More generally, if the refractive index of the surrounding medium is $n_{sm} \neq 1$ the equation [4.44] modifies its expression as reported in [117].

$$n_s \frac{j_{l-1}(n_s\, k_0\, a)}{j_l(n_s\, k_0\, a)} = n_{sm} \frac{h_{l-1}^{(2)}(n_{sm}\, k_0\, a)}{h_l^{(2)}(n_{sm}\, k_0\, a)} \tag{4.45}$$

that is the case of major interest for sensing.

For what concern the characteristic equation of TM-modes, we remind that the components of the TM modes are expressed in system (4.36). In this case, applying the

continuity conditions for the magnetic field and proceeding in the same way as for electric field, we end up writing:

$$\frac{j_{l-1}\left(n_s\,k_0\,a\right)}{j_l\left(n_s\,k_0\,a\right)} - n_s\,\frac{h_{l-1}^{(2)}\left(k_0\,a\right)}{h_l^{(2)}\left(k_0\,a\right)} + \frac{l}{k_0\,a}\left(\frac{n_s^{\,2}-1}{n_s}\right) = 0 \qquad (4.46)$$

That is the characteristic equation of TM modes, obtained imposing $r = a$ [113].

4.B Numerical calculations

In this chapter we want to clarify, with some examples, the meaning of the mode quantum numbers l, n, m and their relation with the field distribution in a microspherical structure. Contemporary, we want to verify the exactness of our model. For this purpose we choose the data reported in [118] and compared the relative results. We first report here the parameters of the problem: $R_0 = 16$ µm, $\lambda = 1.48$ µm, $n_s = 1.985$. The starting-point were the characteristic equations and their solutions in order to find the azimuthal quantum number l. For simplicity we only considered the TE polarization mode as done in [118]. All programs were developed in MATLAB.

Fig. 4.3 shows the real part of the characteristic equation for TE modes. The narrow line in the figure represent the discrete l values for WGMs.
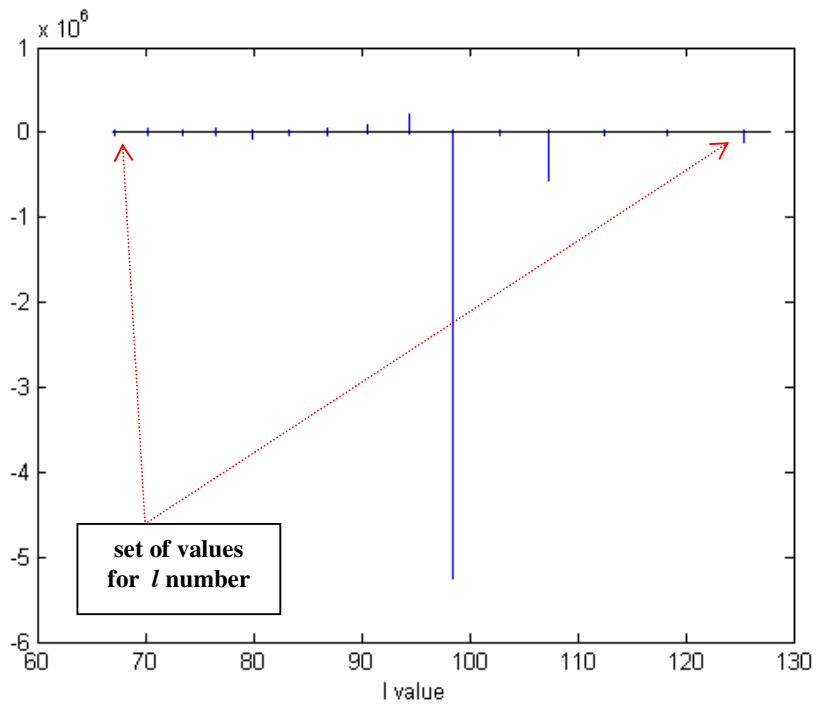
Fig. 4.3 Discrete set of *l* values that satisfies the
characteristic equation for TE modes.

The discrete values of quantum number *l* are 125, 118, 113, 107, 103, 99, 95, 91, 87, 83, 80, 77, 74, 70, 67 and they are closed to those reported in [118]

Once obtained these *l* values in corresponding to the resonance conditions, it is possible to calculate the radial eigenfunction of the field expressed by eq.(A.23), achieving some important information about the behaviour of the resonant modes (WGMs) in this direction.
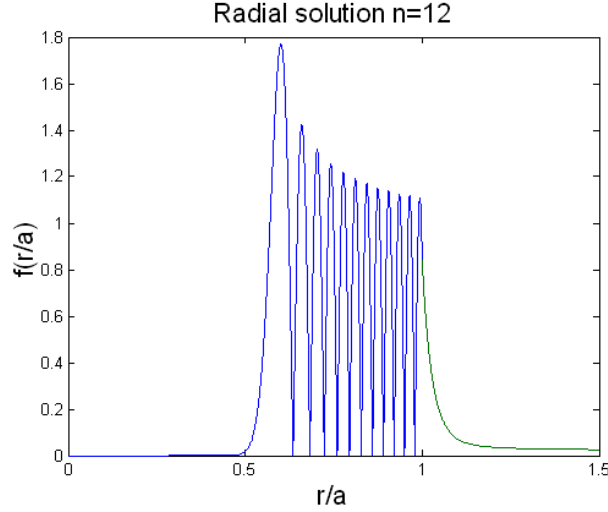
Radial solution n=1

Radial solution n=4

Radial solution n=8
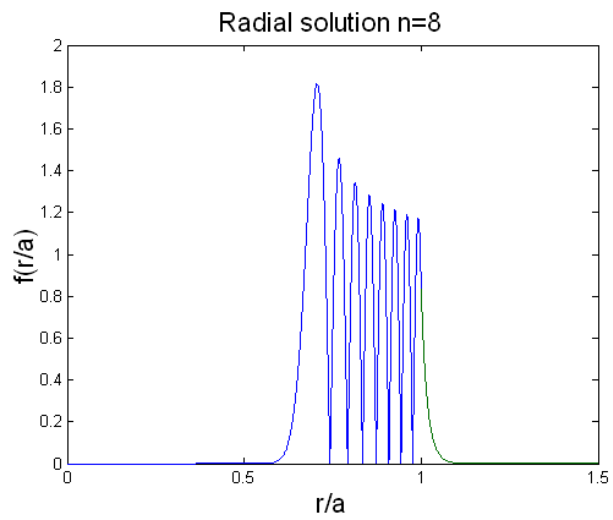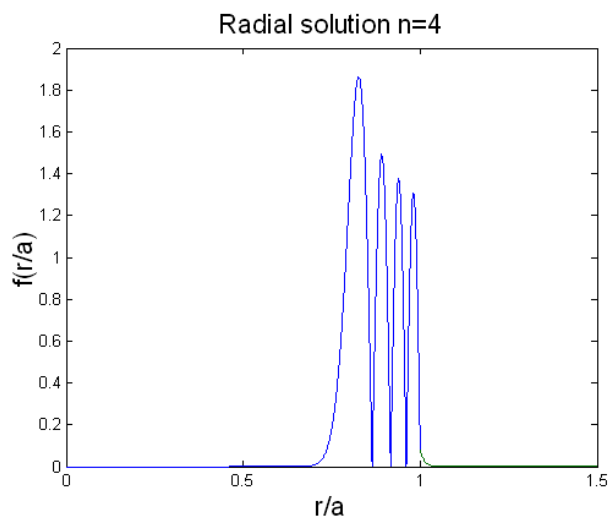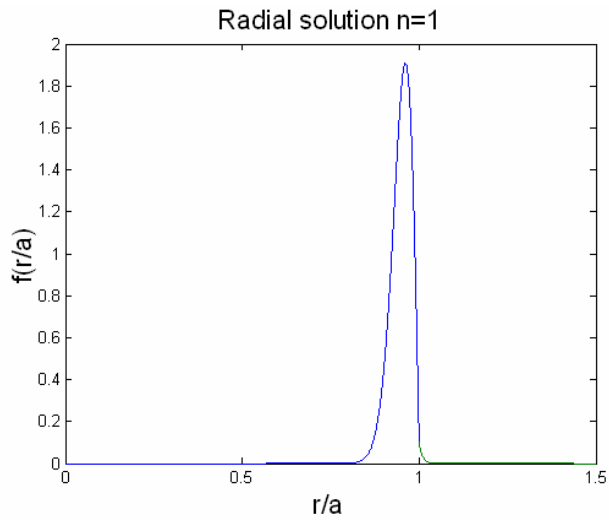
Fig. 4.4: (a) Field distribution in radial direction for: (a) $l = 125$ (n = 1); $l = 107$ (n = 4); $l = 91$ (n = 8); $l = 77$ (n = 12).

As previously stated, n equals the number of maxima in the radial direction. In particular, as shown in Fig.4.5(a)-(d), with a decrease of quantum number l an increase of quantum number n occurs. This means that while the peak of a WGM is very close to the surface of the microsphere for a high value of l (see Fig. 4.4(a)), in correspondence of a smaller one, the mode peak position changes in the radial direction going deeper inside the sphere (see Fig.4.4(b)-(d)). As a consequence a WGM characterized by a high value of the n number presents higher radiation losses with a reduction of the total quality factor Q of the spherical microresonator (see § 4C) [113]. The most interesting case is represented by a WGM well confined in proximity of the spherical surface, corresponding to $n = 1$ as reported in Fig. 4.4(a). Refering to Fig. 4.4(a)-(d) we observe the following correspondences between the couples of l and n quantum numbers: $l = 125$, $n = 1$ (Fig.4.4(a)), $l = 107$, $n = 4$ (Fig.4.4(b)), $l = 91$, $n = 8$ (Fig.4.4(c)); $l = 77$, $n = 12$ (Fig.4.4(d)). An analogous trend is reported in [118] and it confirms the validity of our approach. According to the model, for the radial components of the field the solutions are represented by a spherical Bessel function (blue line in Figures 4.4) inside the microsphere (r < a) while, outside the sphere, the radial electromagnetic field has an exponential decay related to a second order spherical Hankel function (green line in Figures 4.4).

Finally, because the quantum number *m* ranges from –*l* to +*l* values, the choice of *l* value fixes univocally those of *m* and, consequently, the number of maxima *l-m+1* in polar direction is determined, as shown in Fig. 4.5(a)-(f) and Fig.4.6(a)-(b).
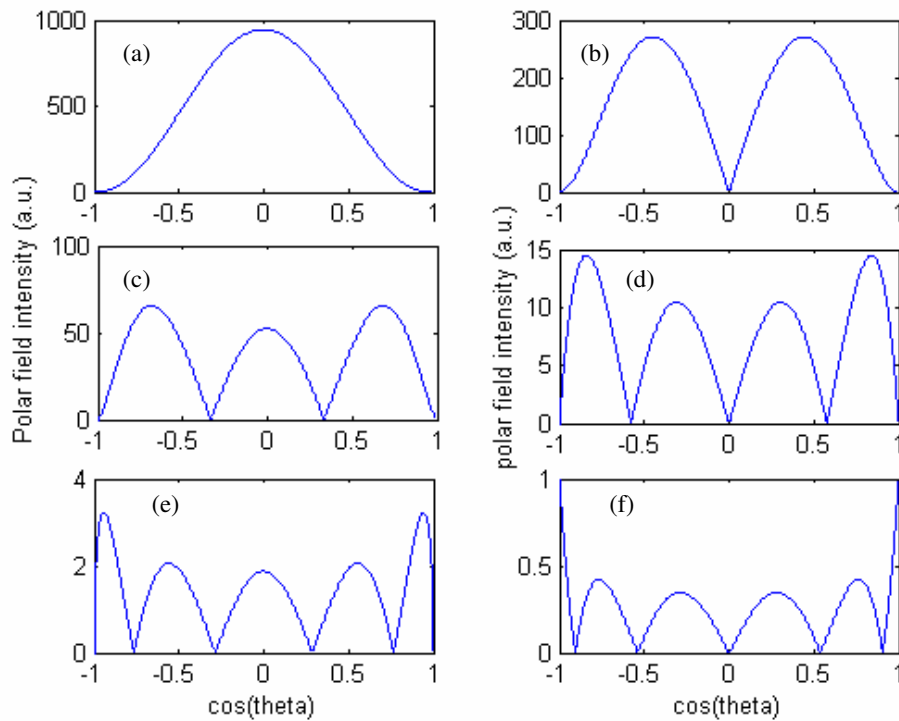

Fig. 4.5: Polar field intensity distribution for different WGM: (a) fundamental WGM for l-m=0; (b) WGM with 2 maxima (l-m=1); (c) WGM with 3 max. (l-m=2); (d) WGM with 4 max. (l-m=3); (e) WGM with 5 max. (l-m=4); WGM with 6 max. (l-m=5)
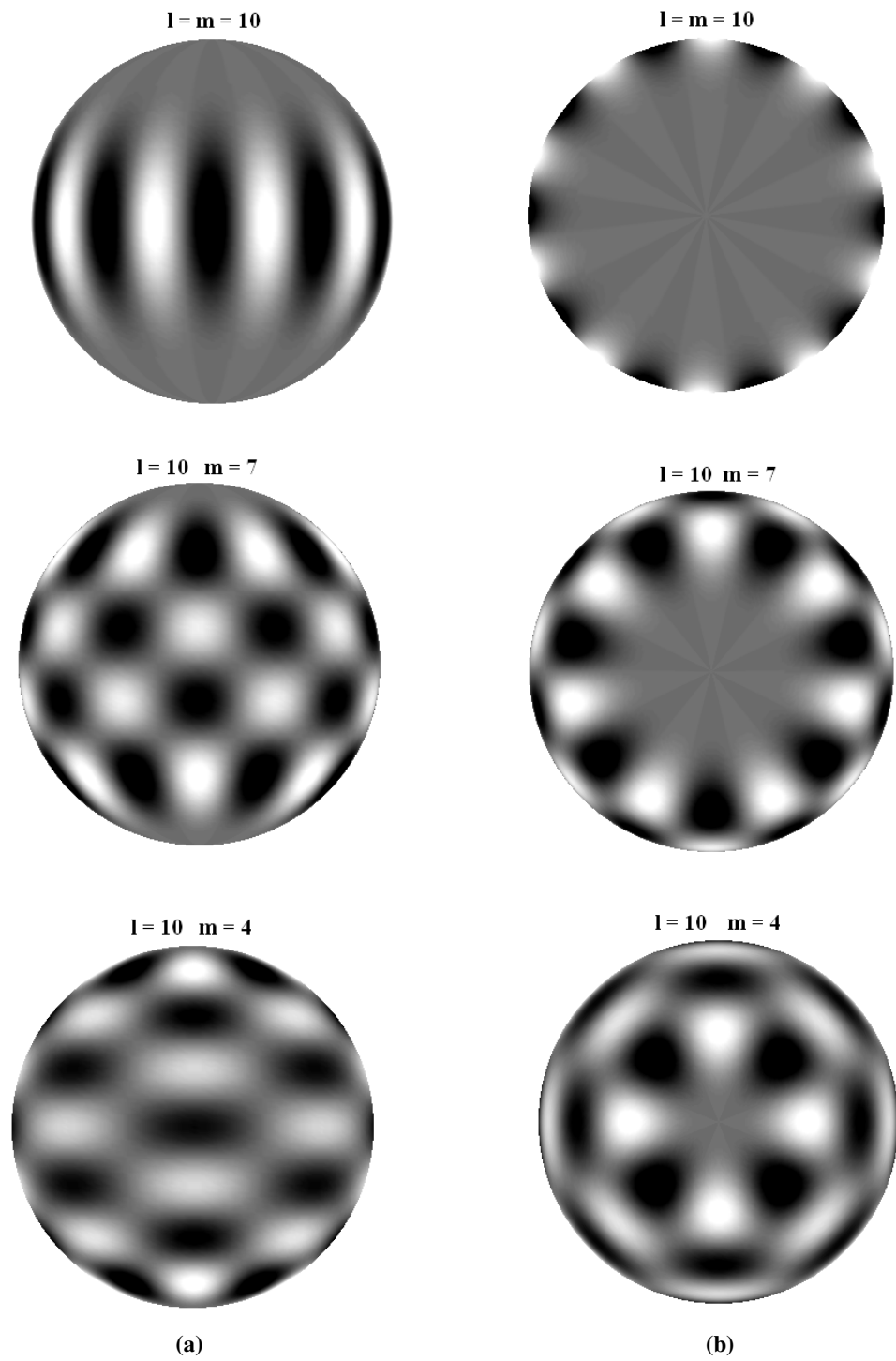
l = m = 10   l = m = 10

l = 10   m = 7   l = 10   m = 7

l = 10   m = 4   l = 10   m = 4

(a)   (b)

Fig. 4.6: **(a)** Normalized distribution of a set of spherical armonic functions characterized by the quantum number $l = 10$ and $m = 10, 7, 4$. An increase of quantum number m corresponds to a decrease of number of the max. in polar direction. **(b)** The projections equatorial plane show the presence of m max. corresponding to the spherical armonic described by quantum number l and m.

4.C Excitation of resonance modes: the tapered fiber coupling technique and some important parameters of spherical microresonators.

4.C.1 Cavity quality factor Q

The losses in DSR devices are described by one important parameter: the quality factor Q. A general expression for this parameter involves energy storage and power loss, as reported below:

$$Q_{TOT} = \frac{2\,\pi\,(stored\;energy)}{energy\;loss\;per\;cycle} = \frac{\omega_0\,V}{W}$$

(4.47)

where ω_0 is the cavity resonant frequency, V is the energy stored in the mode and W is the energy loss rate of the mode. In particular, the quality factor Q is given by different contributions, each one related to a particular kind of loss:

$$\frac{1}{Q_{TOT}} = \frac{1}{Q_{int}} + \frac{1}{Q_{ind}}$$

(4.48)

in which Q_{int} accounts for intrinsic losses while Q_{ind} describes the coupling loss (external loss) due to the coupler. The intrinsic losses are given by [113]:

$$\frac{1}{Q_{int}} = \frac{1}{Q_{mat}} + \frac{1}{Q_{scat}} + \frac{1}{Q_{rad}} + \frac{1}{Q_{cont}}$$

(4.49)

where Q_{mat} is related to the materials absorption losses, Q_{scat} describes the loss caused by residual irregularities on the surface of microresonators, Q_{rad} represents the tunnelling losses due to the curvature of the microsphere in the propagation path of the mode and Q_{cont} is caused by surface contaminations.

.

Material Loss

The quality factor due to the material absorption can be expressed by [113]

$$Q_{mat} = \frac{2\pi N a}{\lambda \alpha} \cong \frac{l}{\alpha} \cong \frac{\sqrt{l(l+1)}}{\alpha}$$ (4.50)

where λ is the wavelength, N is the refractive index of the material, a is the radius of the microsphere, l is the angular quantum number and α is the absorption coefficients of the material. Generally, for silica microsphere ($N = 1.45$) $\alpha = 0.2$ dB/Km at $\lambda = 1.55$ μm, and then $Q_{mat} > 10^{11}$.

Scattering Loss

The contribution related to the surface scattering Q_{scat} is given by the following expression [113]

$$Q_{scat} \cong \frac{3\varepsilon (\varepsilon + 2)^2}{(4\pi)^3 (\varepsilon - 1)^{5/2}} \frac{\lambda^{7/2} (2a)^{1/2}}{(\sigma B)^2}$$ (4.51)

where $\varepsilon = N^2$ is the dielectric constant and σB (nm^2) is a term that measures the correlation length of surface irregularities distribution. For vitreous materials, experimental values for σ and B are, respectively, 0.3 nm and 3 nm. Hence, for instance, in the case of $\lambda > 1$μm e $d > 50$ μm (microsphere diameter), we get $Q_{scat} > 10^{10}$.

Radiation Loss

For what concern the quality factor associated to radiation loss we can say that, increasing the radial dimension of the microsphere, this kind of loss presents an abrupt decrease. For example, in case of pure fused silica microsphere having a high enough

radial dimension (i.e.: $a \geq 20$ μm), $Q_{rad} > 10^{21}$ and then the effects of these losses can be, generally, neglected. The Q_{rad} term can be expressed by [113]

$$Q_{rad} = \frac{1}{2}\left(l + \frac{1}{2}\right)N^{1-2b}\sqrt{N^2 - 1}\exp(2T_l)$$

(4.52)

$$with \quad \begin{cases} b = 0, \; for \; TE \; mod es; \\ b = 1, \; for \; TM \; mod es. \end{cases}$$

and

$$T_l = \left(l + \frac{1}{2}\right)\left[ar\cosh\left(\frac{l + \frac{1}{2}}{x}\right) - \sqrt{1 - \frac{x^2}{\left(l + \frac{1}{2}\right)^2}}\right]$$

(4.53)

with x the size parameter defined in (4.3) giving the resonance positions.
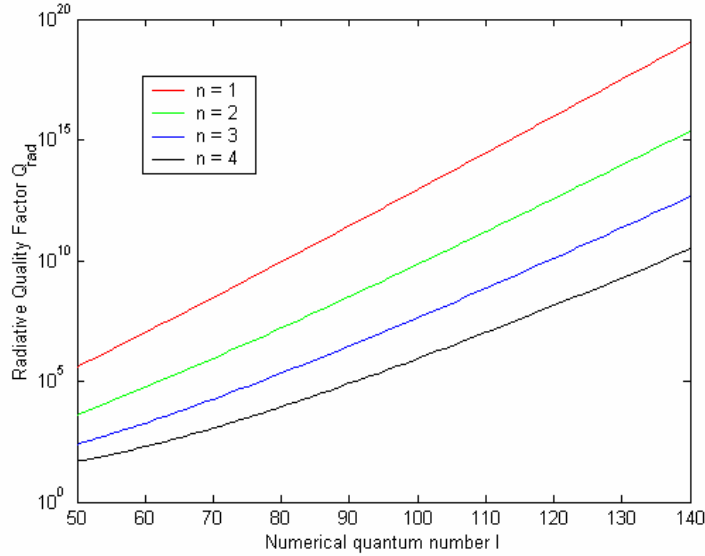The (4.52) and (4.53) equations are valid for high values of l parameter ($l > 18$).

Fig. 4.8 Radiative Quality factor Q_{rad} as a function of quantum number l and n.

A graph on the behaviour of Q_{rad} as a function of quantum number l and n is shown in Fig. 4.3. When l assumes a value approximately around 100 with $n = 1$ (red line in the

109

diagram), the WGM is strongly confined in a thin superficial layer. For this reason the effect of the spherical bounding is not so strong on the propagation of this mode and the Q_{rad} term can assume a high value ($Q_{rad} > 10^{11}$).

On the other hand, maintaining fixed the value of l and increasing n, we can observe a decrease of radiative quality factor Q_{rad}. This is due to the fact that, for higher value of quantum number n, the radial part of the field presents an increase of maxima in this direction: the mode extends towards deeper regions in the microsphere and the curvature effect is more stronger on it. In this case the quality factor Q defined in (4.49) is called *intrinsic quality factor*, Q_{intr}, because the constituting terms are related to the properties of dielectric microresonator.

4.C.2 Excitation of resonance modes in a microsphere cavity

To excite a WGM in a spherical microcavity we need to transfer the light inside the microsphere. Different strategies can be used for this purpose such as prism coupling, polished half block fiber coupling or fiber taper coupling tecnique [112]. In all of these methods the evanescent tail of the electromagnetic field in the coupling device is put in close proximity with the microsphere till it overlaps with the evanescent tail of a WGM. In any case, depending on the intensity of the coupling, the price to pay for this interaction is a reduction of the overall quality factor Q as expressed in eq. (4.48). In fact, considering the case of a fiber taper coupler as reported in Fig. 4.9,
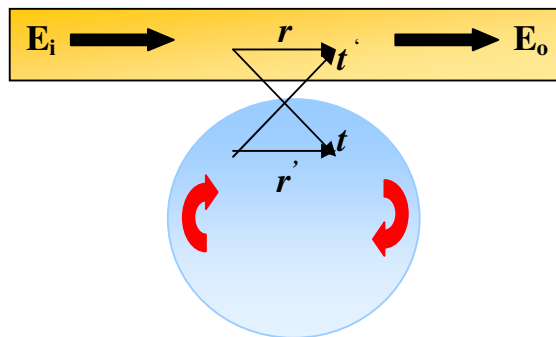

Fig. 4.9 Scheme of the coupling between fiber taper and cavity

we call with E_i and E_o the amplitude of the electric field before and after the interaction with the spherical microcavity, respectively.

Let t and t' be the transmission coefficients of fiber and microsphere, r and r' the corrispective reflection coefficients, for the symmetry and energy conservation we have $t = t'$, $r = r'$ and $r^2 - t^2 = 1$. The behaviour of microsphere is similar to a Fabry-Perot microcavity, with unequal mirrors (one is reflecting 100% of the light). Considering the phase and amplitude contributions for each round trip (for a detailed treatment of Fabry-Perot resonator model we refer to [1]), we can write the ratio between the light intensity coupled inside the microsphere I_s and that at the input of the coupling section I_i

$$\frac{I_s}{I_i} = 1 - \frac{I_o}{I_i} = 1 - \left\| \frac{E_o}{E_i} \right\|^2 = \frac{T_{max}}{1 + F^2 \, sen^2 \left(\beta L/2 \right)} \tag{4.54}$$

where T_{max} is expressed by:

$$T_{max} = 1 - \left(\frac{r - e^{-\alpha L}}{1 - r\, e^{-\alpha L}} \right)^2 \tag{4.55}$$

and F is the *Finesse* of the spherical microcavity, defined as:

$$F = 2 \frac{\sqrt{r\, e^{-\alpha L}}}{1 - r\, e^{-\alpha L}} \tag{4.56}$$

In all these equations, α represents the absorption coefficient of the material (0.2 dB/km in the case of microsphere composed by pure fused silica at 1.55 μm wavelength), $L \cong 2 \pi\, a$ is the optic path and β the propagation constant of the light in the spherical microresonator given by (4.7). From eq.(4.54) we can say that, respect to the incident light spectrum in the fiber, the microsphere is a resonant cavity because it "absorbs" the radiation only in correspondence of some particular frequencies. Hence, the transmitted spectrum in the fiber will present minimum values (spectral holes) in correspondence of the absorption frequencies of the microsphere.

The eq.(4.54) represents the transfer function, in the frequencies domain, which describes the optical power transmitted in the cavity. According to (4.55), the amplitude of this transfer function assumes a maximum value (T_{max} = 1) when $r = e^{-\alpha L}$. This condition is also called *critical coupling*. The *finesse F* accounts for the frequency selectivity of the device and depends on the values assumed by the reflection coefficient *r* as reported in (4.56). In particular, for a spherical microcavity the *Free Spectral Range FSR*, which represents the frequency distance between two maxima is given by:

$$\Delta \nu = \nu_{l+1} - \nu_l = \frac{c}{L N} \cong \frac{c}{2 \pi a N} \tag{4.57}$$

where $\nu_l = \dfrac{c\,l}{L N} \cong \dfrac{c\,l}{2 \pi a N}$, with *c* the velocity of light in the vacuum.

4.C.3 Phase matching between the microcavities and the fiber-taper coupler

The coupling efficiency is maximized when the propagation constant of a suitable mode in the fiber β_{fiber} equals the propagation constant, β_{sphere}, of a WGM of the microresonator. This is the so called *phase matching condition* between the microcavity and fiber-taper coupler.

The propagation constant of the fundamental mode of a tapered fiber with radius r (the tapered has a diameter of a few microns) in air is given by [119]:

$$\beta_{fiber} = \sqrt{k^2\, N^2 - \left(\frac{2.405}{r}\right)^2} \tag{4.58}$$

where *k* is the propagation constant in free space. On the other hand, the propagation constant β_{sphere} of a WGM is equal to β_l expressed by (4.7) and depends on the quantum number *l* and the radius of microsphere. Then, from these two last expressions, it is easy to conclude that the phase matching condition $\beta_{fiber} = \beta_{sphere}$ can be reached by a suitable choice for radial dimensions of tapered fiber and microsphere.

For instance, for IOG10 silicate glass microsphere the *phase matching condition* can be obtained from the following graph where we report the propagation constant β (m^{-1}) at the wavelength of 1480 nm and 1545 nm, as a function of fiber radius (μm).
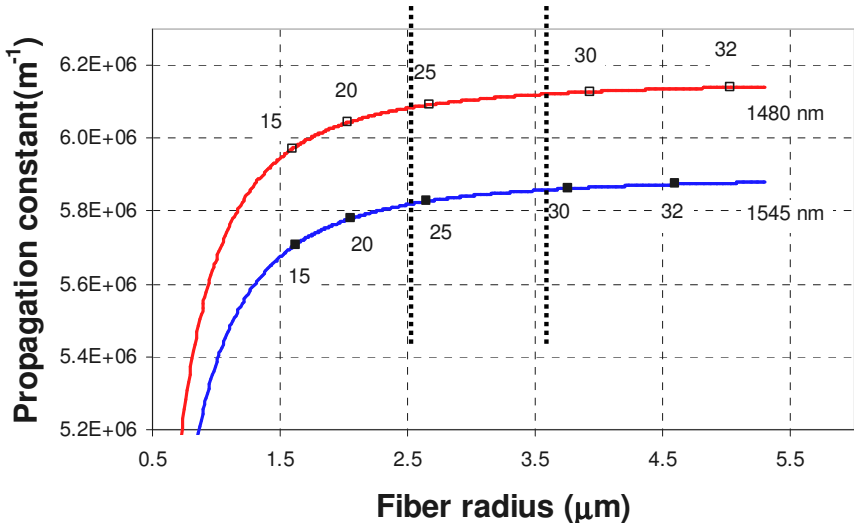

Fig. 4.10 Propagation constant as a function of fiber radius at pump wavelength (1480 nm) and laser wavelength (1545 nm). The numbers reported in the graph are the radius (μm) of the microspheres having the corresponding propagation constant at 1480 nm (empty square) and 1550 nm (square) for the fundamental mode.

As it is easy to see, only a limited set of value for fiber and microsphere radii satisfies the *phase condition* for both wavelengths. In particular, for $1.5\ \mu m < r_{fiber} < 2.5\ \mu m$ and $15\ \mu m < r_{sphere} < 25\ \mu m$ we have $\beta_{fiber} \cong \beta_{sphere}$ at both wavelengths.

4.D   Measurements on laser action in active glass microspheres: Experimental and Results

4.D.1 Fabrication of optical microspheres

Microspheres were produced from different kind of oxide glasses: an experimental modified-silica glass, doped with 0.5 mol.% of Er^{3+} (Baccarat Glass, B05), and commercial Er^{3+}/Yb^{3+} co-doped silicate (IOG10) and phosphate glass (Schott IOG2). Each bulk glass sample was ground first and then microspheres were produced by fusion of these glass powders through a microwave plasma torch as shown, in Fig. 4.7.
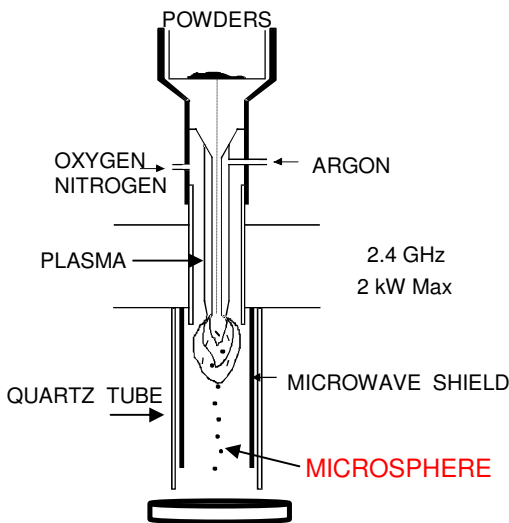

Fig. 4.11 A scheme of the plasma torch system used to fabricate glass   microspheres

This system is adopted at the Laboratoire d'Optronique at the ENSSAT in Lannion (France), where the microsphere were fabricated. The plasma is generated using a microwave supply with a nominal oscillator frequency of 2.4 GHz and a maximum power of 2KW. Argon is used as plasma gas and oxygen or nitrogen as sheath gas. The glass powders were axially injected and melt when passing trough the flame while the surface tension forces give them their spherical shape. Free spheres with diameters in

the range 10 to 200 µm were collected a few centimetres below. The diameter of the spheres depends on the powder size. After their realization, the microspheres were selected and then glued to the tip of an optical fibre, in order to make easier to manipulate them (see Fig. 4.12).

The fiber was then mounted on a translation stage with piezoelectric actuators and a positioning resolution of 40 nm.
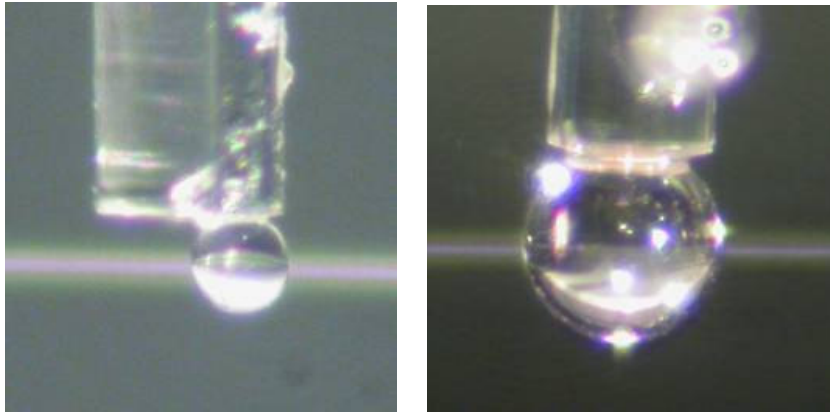

Fig. 4.12 Two images of microspheres glued to a fiber tip for handling. On the background it is possible to see the tapered fiber for coupling.

4.D.2 Fabrication of tapered fiber

We used a tapered or half-tapered fiber to couple the pump light in the microsphere and, contemporary, to draw the fluorescence or laser signal out of it, following the scheme shown in Fig. 4.9. The tapered fiber was fabricated by heating and the same time slowly stretching a section of standard telecommunication fiber to form a narrow waist. As indicated in Fig. 4.13 the stripped fiber was placed inside a short alumina cylinder, which was then heated by an oxygen-butane flame up to a temperature close to a melting point of silica (about 2100 °C).
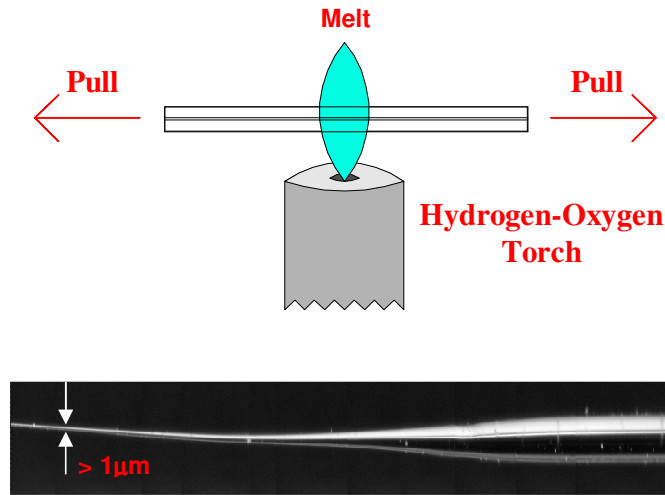
Fig. 4.13 Fabrication process of a tapered fiber coupler. As shown in a microscope image below, it is possible to obtain dimensions about 1 μm for the diameter of the taper.

The taper waist can be as little as a micrometer in diameter while the typical total length of the adiabatic tapered section is about 2 cm. The half taper fiber coupler was obtained instead by heating and stretching a fiber until breaking, using a fusion splicer. The tapered end is about 1.5 μm in diameter.

4.D.3 Set-up for laser action measurements and results

The experimental setup for laser characterization of Er^{3+}-doped microspheres is represented in Fig. 4.14 and it was realized with standard fiber-optic components spliced or connected with APC connectors.
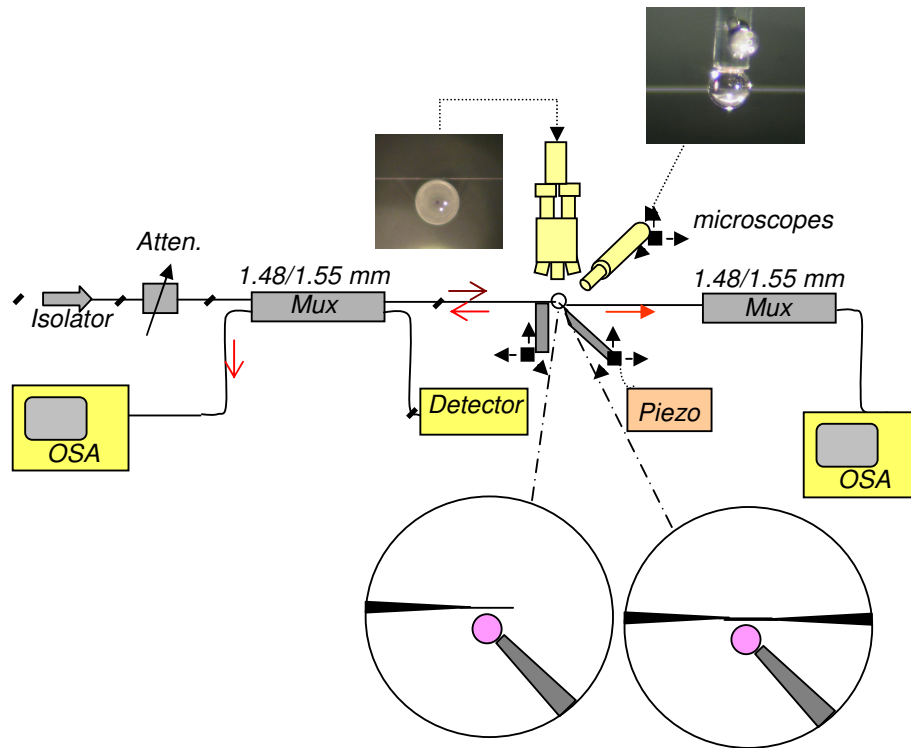
Fig. 4.14 Fluorescence and Laser measurements Set-Up for optical microsphere

It consists of a fiber pigtailed pump laser diode operating at 1.48 µm with a maximum power of 300 mW, an isolator that prevent feedback into the laser diode, and a WDM that demultiplexes light at 1.48 and at 1.55 µm. This latter device allows us to simply use an half taper as the coupling device: in fact the counter propagating fluorescence or laser signal from the sphere can be collected by the same input fiber and directed to an Optical Spectrum Analyzer (OSA) through the 1.55 µm port of the WDM. Two camera systems permit the operator to monitor the relative position of tapered fiber and microsphere. This last one can be positioned through a piezoelectric actuators system. We chose a pump laser diode operating at 1.48 µm, instead of 980 nm, because with this choice the matching condition can be better fulfilled at both the pumping and lasing wavelength. In Fig. 4.15 and 4.16 we report the emission spectra of a B05 glass microsphere with a diameter of 85 µm and a IOG2 microsphere with a diameter of 70 µm, respectively. Below lasing threshold more modes are excited, which qualitatively justifies the large number of lines on the fluorescence spectrum. These series of peaks

can be assigned to several families of modes each of them having the same radial order *n*, but different polarizations and angular moment *l*.
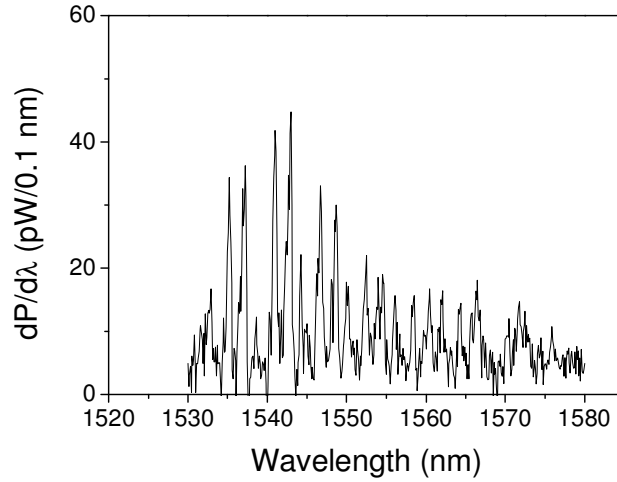

Fig. 4.15 WGMs fluorescence spectrum around 1.55 μm of a 85 μm diameter microsphere fabricated in Er^{3+} doped B05 silicate glass microsphere fluorescence

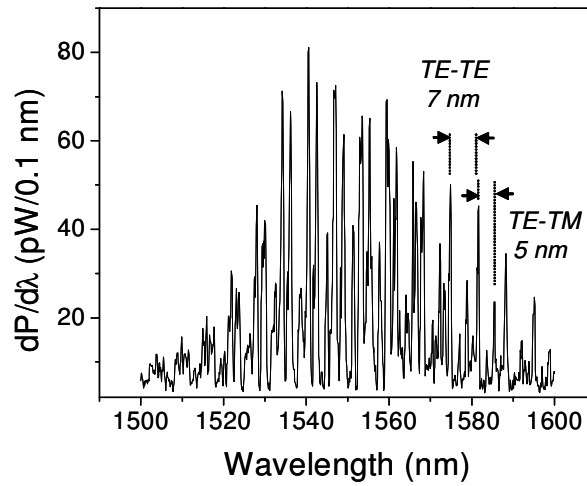

Fig. 4.16 WGMs fluorescence spectrum around 1.55 μm of a 70 μm diameter microsphere fabricated in Er^{3+}/Yb^{3+} doped IOG2 phosphate glass microsphere. The distance between two consecutive TE modes is on the order of few nm.

When increasing the pump intensity above a minimum threshold of 2.5 mW we obtained laser oscillation as shown in Fig.4.17 for B05 Baccarat microsphere and in Fig.4.18 for IOG2 phosphate Schott glass microsphere.

Fig. 4.17 Laser spectra corresponding to the maximum (red line) and to the minimum (blue line) wavelength peak values obtained in B05 glass microsphere with diameter of 85 μm.
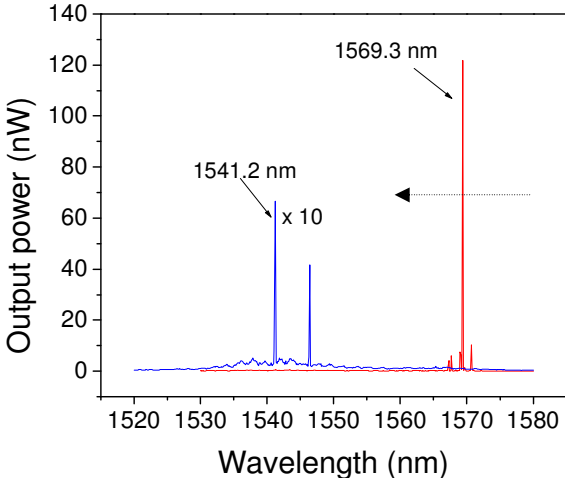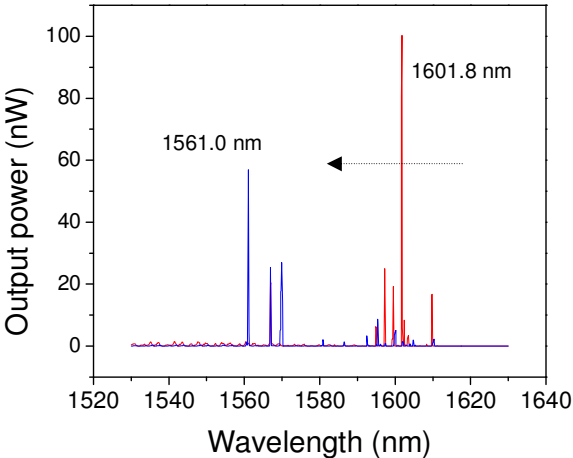

Fig. 4.18 Laser spectra corresponding to the maximum (red line) and to the minimum (blue line) wavelength peak values obtained in IOG2 glass microsphere with diameter of 70 μm.

In both cases, adjusting the pumping power and varying the relative contact position between the fiber taper and the sphere, the emission domain can be selected. For a large

value of this distance and low pumping power we obtained a maximum for the laser emission around 1569.3 nm for B05 microsphere (red peak in Fig.4.17). On the contrary, for a lower gap value associated to higher pumping we obtained multimode laser effects at lower wavelengths, around 1541.2 nm (blue peaks in Fig.4.17). The covered range is about 30 nm broad. A similar set of results we observed in the microsphere made from IOG2 phosphate glass, as reported in Fig.4.18. Fluorescence spectrum looks broader as compared to that of B05 glass microsphere and correspondingly the difference between the lowest (blue line at 1561.0 nm) and the highest (red line at 1601.8 nm) peak lasing wavelengths expands to 40 nm. Moreover a blue shift for these lasing peaks with an increase of pump power was experimentally obtained also in IOG2 microsphere. This effect can be qualitatively explained with a similar shift that occur in the net cross section of the Er^{3+}-doped phosphate glass, as reported in Fig.4.19. At very low pumping power (corresponding to an inversion rate $p < 0.3$) the net cross section is negative in the whole communication window, and no lasing mode can be excited. With an increase of pump power the inversion rate increases ($p = 0.3 \div 0.4$) as well: the net cross section becomes positive in the longer-wavelength region and, consequently, a lasing mode in that region can be excited first with a lower threshold. Further increasing the pumping power, the gain at shorter wavelengths becomes positive (the inversion rate p ranges from 0.5 to 0.8) with a shift in that region of the spectrum and laser action.
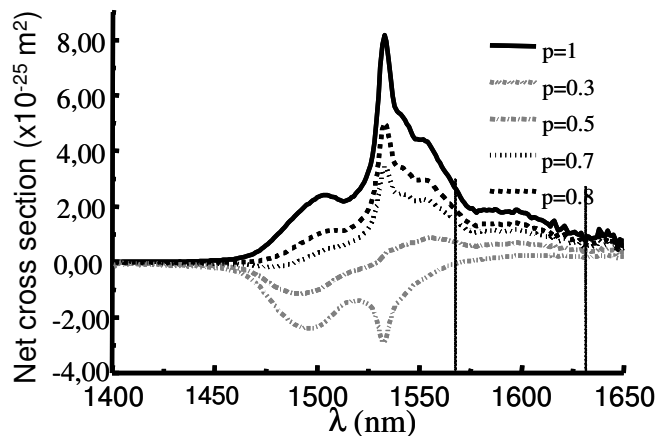

Fig. 4.19 Net gain spectra $G(\lambda,p)$ for Er^{3+}/Yb^{3+} IOG2 co-doped phosphate glass in term of pumping level.

120

Therefore, simply adjusting the pump power it is possible to tune the wavelength of the lasing mode and this is an important benefit that the microsphere lasers offer in comparison with the waveguide lasers where the lasing wavelength is fixed. A drawback is related to the fact that the shift of the lasing wavelength is not continuous but discrete.

Lasing in a 50 µm diameter IOG10 silicate glass microsphere was also successfully demonstrated as shown in Fig.4.20.
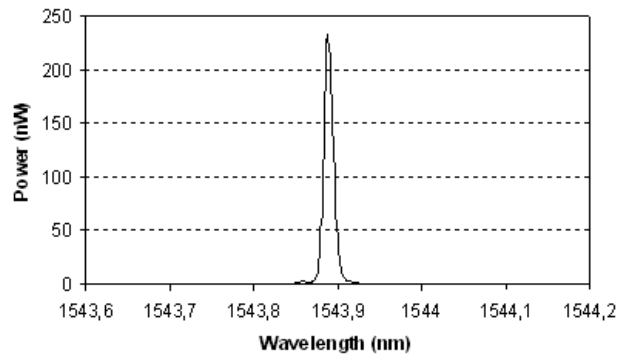

Fig. 4.20 Lasing emission for IOG10 silicate glass
microsphere with a diameter of 50 µm.

A 1480 nm pump laser was used . The radius of the fiber taper was 2.5 µm.

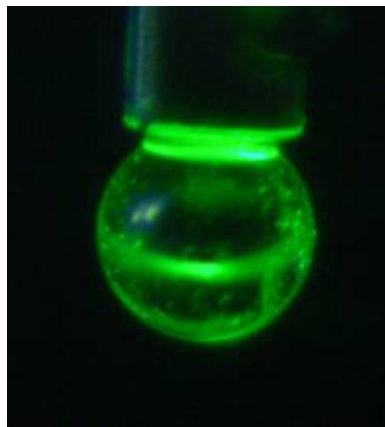A maximum lasing power of 240 nW was obtained at 1543.9 nm with a pump threshold around 400 µW.

Fig. 4.21 Green Up-Conversion in IOG10 silicate glass
microsphere laser with a diameter of 50 µm.

CONCLUSIONS

This thesis is focused on the fabrication and characterization of optical waveguides and microspherical cavities in RE doped glasses for lasers and amplifiers. A number of different Er^{3+} or Er^{3+}/Yb^{3+} doped glasses were tested and used during this work including four silicate glasses (two experimental ones, one from Baccarat, and one from Schott), a commercial Schott phosphate glass, an experimental tellurite glass, and a silica-germania glass layer. Spectroscopic characterizations were performed in all these glasses while different fabrication processes (i.e. ion-exchange, RF-sputtering, UV imprinting, and ion beam irradiation or glass melting) were implemented depending on the glass formulation and on the device type (waveguide or microsphere). The main results have been the development of innovative photoimprinting techniques, based on UV exposure or ion beam irradiation, to fabricate channel waveguides in novel active glasses and the demonstration of tunable laser action in different types of glass microspherical cavities.

The two classes of experimental silicate glasses doped with Er^{3+} and Yb^{3+}, a soda-lime (MY2) and a soda-lime-alumino (SLASY1) silicate, were fabricated with a conventional melt-quenching technique. MY2 presented high values for both lifetime (7.5 ms) and quantum efficiency (62%) but exhibited a rather narrow effective bandwidth around 1.55 μm (only 31 nm). In order to improve this latter value, which is critical for WDM applications, we increased the aluminium oxide content of the glass ([P.IV], [P.V], [P.VII]). In fact in SLASY1 glass (17% of alumina) a 60% increase of the effective emission bandwidth (up to 50 nm) was observed compared to MY2 glass (1% of alumina). On the other hand in SLASY1 glass the measured lifetime was shorter (<5 ms) and the quantum efficiency smaller (47%) in comparison with MY2. We ascribed these results to the different role that the alumina has in the silica network depending on its concentration: it acts as a glass modifier for lower concentrations (MY1 glass) and as a glass former for higher ones (SLASY1 glass).

As both MY2 and SLASY1 contain high percentage of sodium oxide, these glasses were selected for the fabrication of channel waveguide by the ion-exchange process ([P.IV], [P.VII], [P.IX]). The best performances, as amplifiers, were obtained in MY2

waveguides. In particular, using a three steps fabrication process (first thermal ion-exchange and then burial by field-assisted ion exchange, followed by an annealing treatment) for a 4 μm wide channel waveguide we measured propagation losses ≤ 0.6 dB/cm, fiber-waveguide coupling losses ≤ 0.8 dB and, more important, a net gain of 0.8 dB/cm with a pump power of 170 mW at 976 nm. This gain could be enough to obtain a laser action in this glass.

Er^{3+}/Yb^{3+} activated SiO_2-GeO_2 thin films were fabricated in order to obtain a multifunctional material having both active and photo-refractive properties. The films were deposited by a RF-magnetron sputtering system. Instead of using a sintered multi-component target, pieces of GeO_2, metallic erbium and metallic ytterbium were simply placed on a silica target.

A photoluminescence bandwidth over 40 nm and a lifetime of 8.7 ms were measured in the slab waveguide.

Using UV excimer laser irradiation (KrF, 248 nm), because of the photorefractive properties of germanium, it is possible to modify the physical properties of the film (i.e.: the density) and thus the refractive index. In particular a maximum positive refractive index change of 3.8×10^{-3} was obtained with 22 kJ/cm^2 of cumulative exposure. This value is high enough not only to fabricate gratings but also a channel waveguides in such material. The former were obtained using the phase mask technique, the latter with an amplitude mask and a photo-imprinting process ([P.II], [P.III]). The resulting Bragg gratings had efficiency near 100%. The channel waveguides had propagation losses ≤ 0.3 dB/cm at 1300 nm, the same as the slab waveguide. This method to fabricate waveguides by a single step replica of an intensity mask has the very important benefit to reduce the fabrication steps and related costs in comparison with other standard techniques (ion exchange, film deposition followed by etching, …). Moreover, for integrated laser applications, both guiding structure and reflective Bragg gratings can be fabricated with the same UV imprinting technique.

Remarkably, we have recently demonstrated [P.I], for the first time, the possibility of fabricating active channel waveguides in tellurite glasses [49] using nitrogen ion beam irradiation. A region of positive refractive index change (Δn > 0) was formed in the ion-

implanted channel, permitting 2D light confinement. From the result we obtained, it seems that the ionization processes induced by the implanted nitrogen ions (i.e.: rearrangements of the substrate bonds and chemical interactions with the substrate) are the major contributing factors to the refractive index increase. We believe that channel waveguides in tellurite glasses, for the unique spectroscopic properties of these materials (particularly the broad band), may have great potential for the development of integrated active devices.

As for microspherical cavities we presented an analytical model for the electromagnetic propagation in dielectric spherical resonators based on the solution of Maxwell's equations by means of vector and Debye's scalar potential. Numerical simulations, developed in MATLAB code, were also performed in order to demonstrate the validity of the method adopted and to calculate the WGMs field distribution inside these microspherical structures.

Microspheres were produced from three different oxide glasses: a modified-silica glass, doped with 0.5 mol.% of Er^{3+} (Baccarat Glass B05), and commercial Er^{3+}/Yb^{3+} doped silicate (IOG10) and phosphate (IOG2) glasses, both developed by Schott for laser applications. Each bulk glass sample was ground first and then microspheres (with diameters below 100 μm) were produced by fusion of the glass powders through a microwave plasma torch.

The effect of the glass fusion process on the spectroscopic properties of the active microspheres was investigated. The spectroscopy of these microcavities has revealed a broadening of the luminescence spectrum and a shortening of the lifetime compared to those of the corresponding bulk glasses. We believe that both effects are related to inhomogeneous changes in the local environment of Er^{3+} ions induced by the microsphere fabrication process [P.VI].

The problem of coupling light in these microcavities has also been addressed and properly designed fiber tapers have been fabricated and used for this purpose.

From all type of microspheres we obtained laser action, with low threshold (few hundreds of μW or a few mW at maximum), narrow band and few hundreds of nW as output power. Moreover, the fact that different laser wavelengths could be excited

within a broad range, depending on pump coupling conditions, demonstrated that tunability is another important characteristic of these optical microsources [P.VI, P.VIII].

APPENDIX A

Helmholtz's equation in spherical coordinates and its solution.

In this appendix we will obtain the expression of magnetic and electric vector potentials $\vec{A}$ and $\vec{F}$. For instance, we consider the case of magnetic vector potential $\vec{A}$. From the divergence equation of magnetic field $\vec{H}$:

$$\nabla \cdot \vec{H} = 0 \tag{A1}$$

it is possible to write that

$$\vec{H} = \frac{1}{\mu} \nabla \times \vec{A} \tag{A2}$$

as it is always true that $\nabla \cdot \nabla \times \vec{V} = 0$, being $\vec{V}$ any vector. Moreover, the vector potential $\vec{A}$ can be expressed through a Debye potential ψ, as shown in eq. (4.17). This scalar potential satisfies the Helmholtz's equation

$$\nabla^2 \psi + k^2 \psi = 0 \tag{A3}$$

where k^2 is a separation constant. In a spherical coordinate system the eq.(A3) becomes

$$\frac{1}{r^2} \frac{\partial}{\partial r} \left(r^2 \frac{\partial A}{\partial r} \right) + \frac{1}{r^2 \sin\theta} \frac{\partial}{\partial \theta} \left(\sin\theta \frac{\partial A}{\partial \theta} \right) + \frac{1}{r^2 \sin^2\theta} \frac{\partial^2 A}{\partial^2 \phi^2} + k^2 A = 0 \tag{A4}$$

To solve the equation (A4), we use the standard approach of separating the variables:

$$A(r,\theta,\phi) = R(r)\Theta(\theta)\Phi(\varphi) \tag{A5}$$

Substituting (A5) in the equation (A4) and multiplying for $r^2 / R\Theta\Phi$, we obtain

$$\frac{1}{R} \frac{d}{dr} \left(r^2 \frac{dR}{dr} \right) + k^2 r^2 + \frac{1}{\Theta \sin\theta} \frac{d}{d\theta} \left(\sin\theta \frac{d\Theta}{d\theta} \right) + \frac{1}{\Phi \sin^2\theta} \frac{d^2\Phi}{d\varphi^2} = 0 \tag{A6}$$

where the first term only depends on r, the second is a function of θ and the third depends on φ.

Azimuthal Dependence

The last term of the (A6), multiplied by $\sin^2\theta$, involves only φ variable. It must be then a constant which we call $-m^2$

$$\frac{1}{\Phi}\frac{d^2\Phi}{d\varphi^2}=-m^2 \tag{A7}$$

Solutions of eq. (A7) are of the form

$$\Phi(\varphi)=\begin{Bmatrix}\cos m\varphi\\ \sin m\varphi\end{Bmatrix} \tag{A8}$$

where m is an integer (in order that the solution is the same for φ and $\varphi+2\pi$).

Thus, the eq. (A6) is reduced to the following form:

$$\frac{1}{R}\frac{d}{dr}\left(r^2\frac{dR}{dr}\right)+k^2\,r^2+\frac{1}{\Theta\sin\theta}\frac{d}{d\theta}\left(\sin\theta\frac{d\Theta}{d\theta}\right)-\frac{m^2}{\sin^2\theta}=0 \tag{A9}$$

The third and fourth terms in eq. (A9) are only a function of θ (whereas the first two only depend on r).

Polar Dependence

As we have just obtained for azimuthal dependence, also for polar *dependence* we can write

$$\frac{1}{\Theta\sin\theta}\frac{d}{d\theta}\left(\sin\theta\frac{d\Theta}{d\theta}\right)-\frac{m^2}{\sin^2\theta}=-l(l+1) \tag{A10}$$

where $l(l+1)$ is a constant. Developing the first term and rearrangingin, the previous equation becomes

$$\frac{d^2\Theta}{d\theta^2}+ctg\,\theta\frac{d\Theta}{d\theta}+\left(l(l+1)-\frac{m^2}{\sin^2\theta}\right)\Theta=0 \tag{A11}$$

that is the *Associated Legendre equation.*

So, the solution to the angular equation for Θ, reported in (A11), is

$$\Theta(\theta) = P_l^m(\cos\theta) \tag{A12}$$

where the $P_l^m(\cos\theta)$ are *Associated Legendre functions* and $l = 0, 1, 2, 3,\ldots$while m runs over integer values from $-l$ to l, because the Legendre function is void for $|m| > l$. Then for each l values there are $2l+1$ functions with $m = -l,\ -l+1,\ -l+2,\ldots,\ l-2,\ l-1,\ l$ [112,118]. When $m = 0$ the *Associated Legendre functions* coincide with the *Associated Legendre polynomials.* Here we can understand why the mode number l must be an integer. In fact, if l is not an integer, the solution of eq. (A11) diverges for $\theta = 0$ or $\theta = \pi$. Generally we require the solution to be finite in these limits, and this is the reason why we write the separation constant in eq.(A10) as $l(l+1)$, with l an integer.

Radial Dependence

Finally, from the equations (A9) and (A10) it is possible to obtain the radial dependence as

$$\frac{d}{dr}\left(r^2\frac{dR}{dr}\right) + \left(k^2 r^2 - l(l+1)\right)R = 0 \tag{A13}$$

or equivalently

$$r^2\frac{d^2R}{dr^2} + 2r\frac{dR}{dr} + \left[k^2 r^2 - l(l+1)\right]R = 0 \tag{A14}$$

It turns out to be useful to define a new function *X(r)* defined as

$$R(r) = \frac{X(r)}{\sqrt{kr}} = \frac{X(\rho)}{\sqrt{\rho}}, \quad \text{where } \rho = kr \tag{A15}$$

Substituting this into eq.(A14) we find that *X* function satisfies

$$\frac{d^2 X}{d\rho^2} + \frac{1}{\rho}\frac{dX}{d\rho} + \left[1 - \frac{\left(l+\frac{1}{2}\right)^2}{\rho^2}\right] X = 0 \qquad (A16)$$

which is Bessel's equation of order $l + \frac{1}{2}$. The solution in $X(r)$ is represented by ordinary Bessel and Hankel functions, $J_{l+\frac{1}{2}}(k\,r)$ and $H_{l+\frac{1}{2}}(k\,r)$, which, together with the factor $(k\,r)^{-\frac{1}{2}}$ in the eq. (A15), means that the solution for $R(r)$ are the *spherical Bessel* and *Hankel functions*, $j_l(k\,r)$ and $h_l(k\,r)$.

In fact, the spherical Bessel functions are in close connection with ordinary Bessel function by the relationship reported below:

$$j_l(k\,r) = \sqrt{\frac{\pi}{2k\,r}}\, J_{l+\frac{1}{2}}(k\,r) = \sqrt{\frac{\pi}{2}}\,\frac{J_{l+\frac{1}{2}}}{\sqrt{k\,r}} \qquad (A17)$$

The eq. (A17) is also valid, with due differences, for $H^{(2)}{}_{l+\frac{1}{2}}(k\,r)$ but, since this function has infinite value at $r = 0$, the only acceptable solution to eq. (A16) is

$$X(r) = J_{l+\frac{1}{2}}(k\,r) \qquad (A18)$$

that, substituted in $R(r)$ expression and remembering the eq. (A17), gives

$R(r) = A_1\, j_l(k\,r)$, with A_l = constant.

Hence, the general solution of Helmholtz's equation is

$$A(r,\theta,\phi) = A_1\, j_l(k\,r)P_l^m(\cos\theta)\cos(m\varphi) \qquad (A19)$$

In particular, because usually the scalar potentials ψ are multiplied for r, as shown in eq. (4.17), it is convenient introduce a new kind of spherical Bessel function defined as it follows [109,111]:

$$\hat{j}_l(k\,r) = k\,r\,\sqrt{\frac{\pi}{2k\,r}}\, J_{l+\frac{1}{2}}(k\,r) = \sqrt{\frac{\pi k\,r}{2}}\, J_{l+\frac{1}{2}}(k\,r) \qquad (A20)$$

Now, we are able to write the radial solution of scalar Helmholtz equation as:

$$f(kr) = \begin{cases} A\sqrt{\dfrac{\pi k r}{2}}\, J_{l+\frac{1}{2}}(kr), & 0 \le r \le a; \\[3mm] B\sqrt{\dfrac{\pi k_0 r}{2}}\, H^{(2)}_{l+\frac{1}{2}}(k_0 r), & r > a \end{cases} \tag{A21}$$

where $H^{(2)}_{l+\frac{1}{2}}(k_0\, r)$ is the ordinary Hankel function of second kind (see Appendix C). This function describes the exponential decay of field outside the sphere in the radial direction (leaky wave). The coefficients *A* and *B* can be determined imposing the continuity conditions for *f* function and its derivate in case of *r = a*. Developing calculations, we get:

$A = 1$

$$\tag{A22}$$

$$B = \sqrt{\frac{k}{k_0}}\, \frac{J_{l+\frac{1}{2}}(k\,a)}{H^{(2)}_{l+\frac{1}{2}}(k_0\,a)}$$

These last ones, substituted in (A21), allow to write the expression of radial function *f* as:

$$f(kr) = \begin{cases} \sqrt{\dfrac{\pi k r}{2}}\, J_{l+\frac{1}{2}}(kr), & 0 \le r \le a; \\[3mm] \sqrt{\dfrac{\pi k r}{2}}\, \dfrac{J_{l+\frac{1}{2}}(k\,a)}{H^{(2)}_{l+\frac{1}{2}}(k_0\,a)}\, H^{(2)}_{l+\frac{1}{2}}(k_0\, r), & r > a \end{cases} \tag{A23}$$

Hence, once a value for the angular quantum number *l* is fixed, it is possible to select the number of maxima along the radial component or, in other words, determine the quantum number *n*.

In conclusion of this Appendix, we obtain the expression of the propagation constant β_l reported in eq. (4.7). In fact, the eq. (A14) can be written in the form:

$$\frac{d^2R}{dr^2} + \frac{2}{r}\frac{dR}{dr} + \left[k^2 - \frac{l(l+1)}{r^2}\right]R = 0 \qquad (A24)$$

The field behaviour very near to the surface can be examined by transforming to a local coordinate x, whose origin lies at the surface. The coordinate transformation is

$$r = a\left(1 + \frac{x}{a}\right)$$

$$\qquad (A25)$$

$$r^{-1} = a^{-1}\left(1 - \frac{x}{a}\right)$$

Substituting the (A25) in (A24), we obtain the Airy equation:

$$\frac{d^2R}{dx^2} + \left[k^2 - \frac{l(l+1)}{a^2} + \frac{2x(l(l+1)+2)}{a^3}\right]R = 0 \qquad (A26)$$

Further, if $x/a \ll 1$, the Airy equation itself reduces to

$$\frac{d^2R}{dx^2} + \left[k^2 - \frac{l(l+1)}{a^2}\right]R = 0 \qquad (A27)$$

This describes the bounded portion of the field. It is the transverse dependence of a local plane wave with propagation constant $\beta_l = \sqrt{l(l+1)}/a$.

APPENDIX B

Field determination from their radial components

Let us consider an electromagnetic field $\vec{E}\left(\vec{r},t\right)$ and $\vec{H}\left(\vec{r},t\right)$ in a space region comprised between two concentric spheres with rays a and b, respectively.
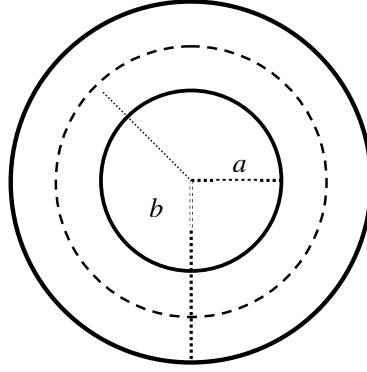

Fig.ApB.1: Planar representation of the problem.

It is possible to demonstrate that the fields present in this region are completely defined from the knowledge of their radial components. In fact a theorem exists [114] stating that if $\vec{E}\cdot\vec{r} = \vec{H}\cdot\vec{r} = 0$ in this region then $\vec{E} = \vec{H} = 0$. To understand this result, we consider fields $\vec{E}$ and $\vec{H}$ having no radial components and we take in account a spherical surface S (dot line in Fig. ApB.1) of radius r included between a and b, $a < r < b$. Because in the region R between the two spheres there are no sources, $\nabla\cdot\vec{E} = \nabla\cdot\vec{H} = 0$. Thus the fields $\vec{E}$ and $\vec{H}$ have flow lines which form closed loops on S. Applying the Stokes' theorem, we can write:

$$\oint \vec{E}\cdot dl = \int_S \nabla\times\vec{E}\cdot\hat{n}\, dS = \int_S -j\omega\mu\vec{H}\cdot\hat{n}\, dS \qquad (B1)$$

where we have used the Maxwell equation (3.1). In (B1) $\hat{n} = \hat{r}$ is the versor normal to the infinitesimal element of surface dS belonging to the surface S that has the closed

132

line l as boundary. Because the vector $\vec{H}$ has no radial components, then $\vec{H} \cdot dS = 0$.

The right-hand side of (B1) vanishes, while the left-hand side is not zero, since the $\vec{E}$

loops are closed. We therefore have a contradiction unless $\vec{E} = 0$. Similarly we can

procede for the magnetic field $\vec{H}$.

As a consequence we can conclude that it is enough to know the radial component of a field to determine, univocally, the same field. The other field components can be obtained from the Maxwell's equation.

APPENDIX C

Ordinary and spherical Bessel (Hankel) functions, Legendre functions and their related expressions

In this appendix we recall the definitions of the spherical Bessel (Hankel) and Legendre functions with their related expressions (for more details we refer to [115]):

$$j_l(kr) = \sqrt{\frac{\pi}{2kr}}\, J_{l+\frac{1}{2}}(kr) = \sqrt{\frac{\pi}{2}}\, \frac{J_{l+\frac{1}{2}}}{\sqrt{kr}} \tag{C1}$$

$$j_l'(kr) = -j_{l+1}(kr) + \frac{l}{kr}\, j_l(kr) \tag{C2}$$

$$j_l'(kr) = j_{l-1}(kr) - \frac{l+1}{kr}\, j_l(kr) \tag{C3}$$

$$j_{l-1}(kr) = -j_{l+1}(kr) + \frac{2l+1}{kr}\, j_l(kr) \tag{C4}$$

$$\int_0^a r\, J^2{}_\nu(kr)\, dr = \frac{a^2}{2}\left\{ J^2{}_\nu(ka) - J_{\nu-1}(ka) J_{\nu+1}(ka) \right\} \tag{C5}$$

$$h_l^{(2)}(k_0 r) = \sqrt{\frac{\pi}{2k_0 r}}\, H_{l+\frac{1}{2}}(k_0 r) = \sqrt{\frac{\pi}{2}}\, \frac{H^{(2)}{}_{l+\frac{1}{2}}}{\sqrt{k_0 r}} \tag{C6}$$

$$h_l^{(2)}(k_0\,r) = j_l(k_0\,r) - i\,y_l(k_0\,r) \tag{C7}$$

where *j(x), y(x)* and *h^{(2)} (x)* denote the spherical Bessel, Neumann and Hankel function, respectively, and *J* the ordinary Bessel function.

The *Associated Legendre functions* are related with *Legendre polynomials* by the relationship reported below

$$P_l^m(x) = \left(1-x^2\right)^{|m|/2} \frac{d^{|m|}}{d\,x^{|m|}} P_l(x) = \frac{1}{2^l\,l!}\left(1-x^2\right)^{|m|/2} \frac{d^{l+|m|}}{d\,x^{l+|m|}}\left(x^2-1\right)^l \tag{C8}$$

where *P_l(x)* are the *Legendre polynomials* defined, for different *l* values, as

$$P_l^0(x) = P_l(x),$$
$$P_1^0(x) = P_1(x) = x = \cos\theta$$
$$P_2^0(x) = P_2(x) = \frac{1}{2}\left(3x^2-1\right) = \frac{1}{2}\left(3\cos^2\theta-1\right) \tag{C9}$$
$$P_3^0(x) = P_3(x) = \frac{1}{2}\left(5x^2-3x\right) = \frac{1}{2}\left(5\cos^2\theta-3\cos\theta\right)$$

……………

Recurrence relations for some *Legendre polynomials* are expressed by

$$\left(1-x^2\right)^{1/2} P_l^{m'}(x) = \frac{1}{2}P_l^{m+1}(x) - \frac{1}{2}(l+m)(l-m+1)P_l^{m-1}(x) \tag{C10}$$

$$P_l^{m+1}(x) - \frac{2m\,x}{\left(1-x^2\right)^{1/2}} P_l^m(x) + \left\{l(l+1) - m(m-1)\right\} P_l^{m-1}(x) = 0 \tag{C11}$$

$$\frac{d\,P_l^m(\cos\theta)}{d\,\theta} = -sen\,\theta\,\frac{d\,P_l^m(\cos\theta)}{d(\cos\theta)} = -sen\,\theta\,P_l^{m'}(\cos\theta) \tag{C12}$$

$$\frac{d\,P_l^m(x)}{d\,x} = \frac{l\,x}{x^2-1}P_l^m(x) - \frac{l+m}{x^2-1}P_{l-1}^m(x) \tag{C13}$$

PUBLICATIONS

[P.I] S. Berneschi, G. Nunzi Conti, I. Bányász, A. Watterich, N. Q. Khanh, M. Fried, F. Pászti, M. Brenci, S. Pelli, G. C. Righini, "**Ion beam irradiated channel waveguides in Er^{3+} -doped tellurite glass**", accepted for publication in *Applied Physics Letters*, Vol. **90**, Issue 12, (21/02/2007).

[P.II] G. Nunzi Conti, S. Berneschi, M. Brenci, S. Pelli, S. Sebastiani, G. C. Righini, C. Tosello, A. Chiasera, M. Ferrari, "**UV photo-imprinting of channel waveguides on active SiO$_2$-GeO$_2$ sputtered thin films**", *Applied Physics Letters*, Vol. **89**, 121102, pp.1-3, (2006).

[P.III] S. Berneschi, M. Brenci, A. Chiasera, M. Ferrari, G. Nunzi Conti, S. Pelli, S. Sebastiani, C. Tosello, G. C. Righini, "**Characterization of highly photorefractive and active silica-germania sputtered thin films**", *Proceedings SPIE*, Vol. 6123, pp. 124-129, (2006).

[P.IV] S. Berneschi, M. Bettinelli, M. Brenci, R. Dall'Igna, G. Nunzi Conti, S. Pelli, B. Profilo, S. Sebastiani, G. C. Righini, "**Optical and spectroscopic properties of soda-lime alumino silicate glasses doped with Er^{3+} and/or Yb^{3+}**", *Optical Materials*, Vol. **28**, pp. 1271-1275, (2006).

[P.V] S. Berneschi, M. Bettinelli, M. Brenci, R. Calzolai, A. Chiasera, M. Ferrari, M. Matterelli, M. Montagna, G. Nunzi Conti, S. Pelli, S. Sebastiani, S. Siligardi, A. Speghini, G.C. Righini, "**Optical and spectroscopic properties of new erbium-doped soda-lime-alumino-silicate glass for integrated optical amplifiers**", *Proceedings SPIE*, Vol. **6025**, pp. 384-391, (2006).

[P.VI] G. Nunzi Conti, A. Chiasera, L. Ghisa, S. Berneschi, M. Brenci, Y. Dumeige, S. Pelli, S. Sebastiani, P. Feron, M. Ferrari, G. C. Righini, "**Spectroscopic and lasing properties of Er^{3+} -doped glass microspheres**", *Journal of Non-Crystalline Solids*, Vol. **352**, pp. 2360-2363, (2006).

[P.VII] S. Berneschi, M. Bettinelli, M. Brenci, G. Nunzi Conti, S. Pelli, S. Sebastiani, C. Siligardi, A. Speghini, G. C. Righini, "**Aluminum co-doping of soda-lime silicate glasses: Effect on optical and spectroscopic properties**", *Journal of Non-Crystalline Solids*, Vol. **351**, pp. 1747-1753, (2005).

[P.VIII] G. C. Righini, C. Arnaud, <u>S. Berneschi</u>, M. Bettinelli, M. Brenci, A. Chiasera, P. Feron, M. Ferrari, M. Montagna, G. Nunzi Conti, S. Pelli, H. Portales, C. Siligardi, A. Speghini, L. Zampedri, "**Integrated optical amplifiers and microspherical lasers based on erbium-doped oxide glasses**", *Optical Materials*, Vol. **27**, pp. 1711-1717, (2005).

[P.IX] S. Sebastiani, <u>S. Berneschi</u>, M. Brenci, G. Nunzi Conti, S. Pelli, G. C. Righini, "**Simple approach to calcolate the refractive index profile of ion-exchanged waveguides**", *Optical Engineering*, 054602, (2005).

REFERENCES

[1]   P. Bassi, G. Bellanca, G. Tartarini, "*Propagazione ottica libera e guidata*", CLUEB Editor, pp. 1-10, (1999).

[2]   W. J. Miniscalco, "*Erbium doped glasses for fiber amplifiers at 1500 nm*", Journal of Lightwave Technology, vol. **9**, No **2**, pp. 234-250, (1991).

[3]   E. Desurvire, "*Erbium doped Fiber Amplifiers, Principles and Applications*", John Wiley, New York, (1994).

[4]   B. Jacquier, L. Bigot, S. Guy, A. M. Jurdyc, "*Rare Earth Doped Confined Structures for Lasers and Amplifiers*", in Spectroscopic Properties of Rare Earths in Optical Materials, pp. 430-461, G. Liu & B. Jacquier Editors, Tsinghua University Press and Springer-Verlag Berlin Heidelberg, (2005).

[5]   Temel Bilici, "*Microsphere based channel dropping for optical communication*", Master of Science Thesis in Electrical and Electronics Engineering, p. 2, (2003).

[6]   H. Nishihara, M. Haruna, T. Suhara, "*Optical Integrated Circuits*", McGraw-Hill, (1989).

[7]   S. Iraj Najafi, "*Introduction to Glass Integrated Optics*", pp. 1-5, Artech-House (1992).

[8]   R. Moncorgé, "*Current Topics in Rare-earth Lasers*", in Spectroscopic Properties of Rare Earths in Optical Materials, pp. 320-378, G. Liu & B. Jacquier Editors, Tsinghua University Press and Springer-Verlag Berlin Heidelberg, (2005).

[9]   G. C. Righini, "*Rare-earth-doped glasses for integrated optical amplifiers*", in Photonic Glasses, Research Signpost, pp. 89-113, Rolindes Balda Editor, (2006).

[10]   P. Laporta, S. Taccheo, S. Longhi, O. Svelto, C. Svelto, "*Erbium-ytterbium microlasers: optical properties and lasing characteristics*", Optical Material, vol. **11**, pp. 269-288, (1999).

[11]   A. J. Kenyon, "*Recent development in rare-earth doped materials for optoelectronics*", Progress in Quantum Electronics, vol. **26**, pp. 225-284, (2002).

[12]   G. C. Righini, S. Pelli, "*Ion exchange in glass: a mature technology for photonic devices*", Proceedings SPIE, vol. **4453**, pp. 93-98, (2001).

[13]   J. Albert, "*Ion Exchange from Salt Melt*", in S. Iraj Najafi "*Introduction to Glass Integrated Optics*", pp. 7-38, Artech House, (1992).

[14]   W. Huang, R. R. Syms, "*Sol-Gel Silica Ion Silicon Buried-Channel EDWAs*", Journal of Ligthwave Technology, vol. **21**, No. **5**, pp. 1339-1349, (2003).

[15]   C. J. Brinker, G. W. Scherer, "*SOL-GEL Science-The Physics and Chemistry of Sol-Gel Processing*", Academic Press, INC. (1990).

[16]   G. R. J. Robertson, J. Jessop, "*Optical Waveguide Laser using an RF Sputtering Nd:Glass Film*", Applied Optics, vol. 30**,** pp. 276-278, (1991).

[17]   F. Zernike, "*Fabrication and Measurement of Passive Components*", in "*Integrated Optics*", pp. 201-241, Ed. T. Tamir, Springer-Verlag, Berlin Heidelberg New York, (1975).

[18]   M. Svalgaard, C. V. Poulsen, A. Bjarklev, O. Poulsen "*Direct UV writing of buried single mode channel waveguides in Ge-doped silica films*", Electronics Letters, vol. **30**, pp. 1401-1403, (1994).

[19]   R. Osellame, S. Taccheo, G. Cerullo, M. Marangoni, D. Polli, R. Ramponi, P. Laporta, S. De Silvestri, "*Optical gain in Er^{3+}-Yb^{3+} doped waveguides fabricated by femtosecond laser pulses*", Optics Letters, Vol. **38**, pp. 964-965, (2002).

[20]   C. Florea, K. A. Winick, "*Fabrication and Characterization of Photonic Devices Directly Written in Glass Using Femtosecond Laser Pulses*", Journal of Lightwave Technology, Vol. **21**, No. **1**, pp. 246-253, (2003).

[21]   A. Polman, "*Erbium implanted thin film photonic material*", Journal of Applied Physics (Applied Physics Reviews), vol. **82,** No. 1, pp. 1-39, (1997).

[22]   P. D. Townsend, P. J. Chandler, and L. Zhang, *Optical Effects of Ion Implantation*, Cambridge, U.K., Cambridge University Press, (1994)

[23]   V. S. Ilchenko, A. B. Matsko, "*Optical Resonator with Whispering-Gallery Modes – Part II: Applications*", IEEE Journal of Selected Topics in Quantum Electronics, Vol. **12**, No. 1, pp. 15-32, (2006).

[24]   K. J. Vahala, "*Optics Microcavities*", Nature, vol. **424**, pp. 839-846, (2003).

[25]   V. Sandoghdar, F. Treussart, J. Hare, V. Lefevre-Seguin, J. M. Raimond, S. Haroche, "*Very low threshold whispering-gallery mode microsphere laser*", Physical Review A, vol. **54**, No. 3, pp. R1777-R1780, (1996).

[26]   T. H. Maiman, "*Stimulated optical radiation in ruby*", Nature, Vol. **187**, p. 493, (1960).

[27]   J. P. Gordon, H. J. Zeiger, C. H. Townes, "*The Maser-New type of Microwave Amplifier, Frequency Standard, and Spectrometer*", Physical Review, Vol. **99**, pp. 1264-1274, (1955).

[28]   M. Bertolotti, "*Storia del* Laser", Bollati Boringhieri (1999)

[29]   A. Einstein, "*Zur Quantentheorie der Strahlung (On the Quantum Theory of Radiation)*", Mitteilungen Der Physikalische Gesellschaft Zurich, (1916).

[30]   O. Svelto, D. C. Hanna, "*Principles of Lasers*", Plenum Press, New York and London, (1998).

[31]   M. J. F. Digonnet, "*Rare-earth-doped fiber lasers and amplifiers*", 2nd Edition, Marcel Dekker Inc., New York, (2001).

[32]   M. Weber, "*Handbook of laser science and technology*", CRC, Boca Raton, USA, (1986-1987).

[33]   R. Reisfeld, C. K. Jorgensen, "*Lasers and excited states of rare-earth*", Springer, Berlin, (1977).

[34]   F. Gan, "*Laser Materials*", World Scientific, Singapore, (1995).

[35]   P. Urquhart, "*Review of Rare-Earth doped fibre lasers and amplifiers*", IEE Proceedings, vol. **135**, No. 6, pp. 385-407, (1988).

[36]   P. Bassi, G. Bellanca, G. Tartarini, "*Componenti e Circuiti Ottici*", CLUEB, (1999).

[37]   H. Azzouz, "*Liquid Droplet Dye Laser*", Master of Science Thesis in Micro e Nanotechnology, University of Copenhagen, (2005).

[38]   C. B. Layne, W. H. Lowdermilk, M. J. Weber, "*Multi-phonon relaxation of rare-earth ions in oxide glasses*", Physical Review B, vol. **16**, pp. 10-20, (1977).

[39]   P. M. Peters, D. S. Funk, A. P. Peskin, D. L. Veasey, N. A. Sanford, S. N. Houde-Walter, S. Hayden, "*Ion-exchanged waveguides lasers in Er^{3+}/Yb^{3+} co-doped silicate glass*", Applied Optics, vol. **38**, No 33, pp. 6879-6886, (1999).

[40]   P. Meshkinfam, "*Erbium Ytterbium co-doped ion-exchanged waveguide amplifier*", Master of Science Thesis, Montreal University, (1998).

[41] G. Liu, "*Electronic Energy Level Structure*", in "*Spectroscopic Properties of Rare Earths in Optical Materials*", pp.1-94, G. Liu and B. Jacquier Eds., Springer-Verlag Berlin Heidelberg, (2005)

[42] D. R. Sadonay, "*Introduction to Solid State Chemistry-Lectures No 7: Glasses*", pp. 1-19, [http://web.mit.edu/3.091/www/archives/Notes7.pdf].

[43] L. A. Riseberg, H. W. Moos, "*Multiphonon Orbit-Lattice Relaxation of Excited States of Rare-Earth Ions in Crystals*", Physical Review, vol. **174**, No. 2, pp. 429-438, (1968).

[44] B. R. Judd, "*Optical Absorption Intensities of Rare-Earth Ions*", Physical Review, vol. **127**, pp. 750-761, (1962).

[45] G. S. Ofelt, "*Intensities of Crystal Spectra of Rare-earth Ions*", Journal of Chemical Physics, vol. **37**, pp. 511-520, (1962).

[46] G. C. Righini, M. Ferrari, "*Photoluminescence of rare-earth-doped glasses*", La Rivista del Nuovo Cimento, vol. **28**, No. 12, pp. 1-53, (2005).

[47] C. Morrison, R. P. Leavitt, Journal of Chemical Physics, vol. **71**, pp. 2366-2374, (1979).

[48] D. E. McCumber, "*Theory of phonon-terminated optical maser*", Physical Review, vol. **134**, pp. A299-A306, (1964).

[49] G. Nunzi Conti, V. K. Tikhomirov, B. Chen, S. Berneschi, M. Brenci, S. Pelli, A. Seddon, M. Bettinelli, A. Speghini, G. C. Righini, "*Ion-exchange planar waveguides in different Er^{3+}-doped tellurite glasses*", Proceeding SPIE, Vol. **4990**, pp. 97-102, (2003).

[50] K. Arai, H. Namikawa, K. Kumata, T. Honda, Y. Ishii, T. Handa, Journal Applied Physics, vol. **59** (10), p. 3430, (1986).

[51] S. Tanabe, "*Optical Transitions of rare earth ions for amplifiers: how the local structure works in glass*", Journal of Non-Crystalline Solids, vol. **259**, p. 1-9, (1999).

[52] S. Pelli, M. Bettinelli, M. Brenci, R. Calzolai, A. Chiasera, M. Ferrari, G. Nunzi Conti, A. Speghini, L. Zampedri, J. Zheng, G. C. Righini, Journal of Non-Crystalline Solids, vol. **345**&**346**, p. 372, (2004).

[53] M. P. Hehlen, N. J. Cockroft, and T. R. Gosnell, *Physical Review B*, vol. **56**, p. 9302, (1997).

[54] Jiang S., Luo T., Hwang B. C., G. Nunzi Conti, M. Myers, D. Rhonehouse, S. Honkanen, N. Peyghambarian, "*New Er^{3+} -doped phosphate glass for ion-exchanged waveguide amplifiers*", Optical Engineering, Vol. **37**, pp. 3282-3286, (1998).

[55] F. D. Patel, S. Di Carolis, P. Lum, S. Venkatesh, J. N. Miller, "*A compact high-performance optical waveguide amplifier*", IEEE Photonics Technology Letters, Vol. **16**, pp. 2607-2609, (2004).

[56] D. L. Veasey, D. S. Funk, N. A. Sanford, J. S. Hayden, "*Array of distributed-Bragg-reflector waveguide lasers at 1536 nm in Yb/Er codoped phosphate glass*", Applied Physics Letters, Vol. **74**, pp. 789-791, (1999).

[57] G. Sorbello, S. Taccheo, P. Laporta, O. Svelto, E. Cianci, V. Foglietti, S. Jiang, N. Peyghambarian, "*Single mode Er:Yb waveguide laser array at 1.5μm*", Electronics Letters, Vol. **37**, No. 16, pp. 1014-1015, (2001).

[58] P. Madasamy, S. Honkanen, D. F. Geraghty, N. Peyghambarian, "*Single mode tapered waveguide laser in Er-doped glass with multimode-diode pumping*", Applied Physics Letters, Vol. **82**, pp. 1332-1334, (2003).

[59] A. Chiasera, C. Tosello, E. Moser, M. Montagna, R. Belli, R. R. Gonçalves, G. C. Righini, S. Pelli, A. Chiappini, L. Zampedri, M. Ferrari, "*Er^{3+}/Yb^{3+} -activated silica-titania planar waveguide for EDPWAs fabricated by rf-sputtering*", Journal of Non-Crystalline Solids, Vol. **322**, pp. 289-294, (2003).

[60] K. Shuto, K. Hattori, T. Kitagawa, Y. Ohmori, M. Horiguchi, "*Erbium-doped phosphosilicate glass waveguide amplifier fabricated by PECVD*", Electronics Letters, Vol. **29**, No. 2, pp. 139-141, (1993).

[61] X. Orignac, D. Barbier, M. X. Du, R. M. Almeida, "*Fabrication and characterization of Sol-Gel planar waveguides doped with rare-earth ions*", Applied Physics Letters, Vol. **69**, pp. 895-897, (1996).

[62] A. Martucci, G. Brusatin, M. Guglielmi, C. Strohhöfer, J. Fick, S. Pelli, G. C. Righini, "*Fabrication and characterization of Sol-Gel GeO$_2$-SiO$_2$ erbium doped planar waveguides*", Journal of Sol-Gel Science and Technology, Vol. **13**, No.1-3, pp. 535-539, (1998).

[63] R. R. Gonçalves, G. Carturan, L. Zampedri, M. Ferrari, A. Chiasera, M. Montagna, G. C. Righini, S. Pelli, S. J. L. Ribeiro, Y. Messaddeq, "*Infrared-to-*

visible frequency upconversion in erbium activated silica-hafnia waveguides prepared by sol-gel route", Journal of Non-Crystalline Solids, Vol. **322**, pp.306-310, (2003).

[64]   T. C. Sum, A. A. Bettiol, K. Liu, M. Q. Ren, E. Y. B. Pun, S. Venugopal Rao, J. A. van Kan, F. Watt, "*Proton beam writing of erbium-doped waveguide amplifiers*", Nuclear Instrument and Methods in Physics Research B, Vol. **231**, pp. 394-399, (2005).

[65]   K. Liu, E. Y. B. Pun, T. C. Sum, A. A. Bettiol, J. A. van Kann, F. Watt, "*Erbium-doped waveguide amplifiers fabricated using focused proton beam writing*", Applied Physics Letters, Vol. **84**, No. 5, pp. 684-686, (2004).

[66]   F. Chen, X. L. Wang, X. S. Li, L. L. Hu, Q. M. Lu, K. M. Wang, B. R. Shi, D. Y. Shen, "*Ion implanted waveguides in Nd^{3+} -doped silicate glass and Er^{3+}/Yb^{3+} co-doped phosphate glass*", Applied Surface Science, Vol. **193**, p. 92-101, (2002).

[67]   S. Taccheo, G. Della Valle, R. Osellame, G. Cerullo, N. Chiodo, P. Laporta, O. Svelto, A. Killi, U. Morgner, M. Lederer, D. Kopf, "*Er:Yb-doped waveguide laser fabricated by femtosecond laser pulses*",Optics Letters, Vol. **29**, No 22, pp. 2626-2628, (2004).

[68]   Y. Sikorski, A. A. Said, P. Bado, R. Maynard, C. Florea, K. A. Winick, "*Optical waveguide amplifier in Nd-doped glass written with near-IRfemtosecond laser pulses*", Electronics Letters, Vol. **36**, No.3, pp. 226-227, (2000).

[69]   H. Kogelnik, "*Theory of Dielectric Waveguide*", in "*Integrated Optics*", pp. 13-81, Ed. T. Tamir, Springer-Verlag, Berlin Heidelberg New York, (1975).

[70]   P. Bassi, L.Scolari, R. Zoli, "*Propagazione di onde elettromagnetiche*", CLUEB, Bologna, (2006).

[71]   R. V. Ramaswamy, R. Srivastava, "*Ion Exchanged Glass Waveguide: A Review*", Journal of Lightwave Technology, Vol. **6,** No.6, pp 984-1002, (1998).

[72]   G. Sorbello, S. Taccheo, M. Marano, M. Marangoni, R. Osellame, R. Ramponi, P. Laporta, "*Comparative study of Ag-Na thermal and field-assisted ion exchange on Er-doped phosphate glass*", Optical Materials, Vol. **17**, pp. 425-435, (2001)

[73]   P. Madasamy, G. Nunzi Conti, P. Pöyhönen, M. M. Morrell, D. F. Geraghty, S. Honkanen, N. Peyghambarian, "*Waveguide distributed Bragg reflector laser arrays in erbium doped glass made by dry Ag film ion exchange*", Optical Engineering, Vol. **41**, pp. 1084-1086, (2002).

[74]   P. Pöyhönen, S. Honkanen, A. Tervonen, "*Inverse ion-exchange method for glass waveguide fabrication*", Optics Letters, Vol. **15**, No. 21, pp. 1206-1208, (1990).

[75]   J. Saarinen, S. Honkanen, S. I. Najafi, J. Huttunen, "*Double-ion-exchange process in glass for the fabrication of computer-generated waveguide holograms*", Applied Optics, Vol. **33**, No. 16, pp. 3353-3359, (1994).

[76]   A. Tervonen, P. Pöyhönen, S. Honkanen, M. Tahkokorpi, S. Tammela, "*Examination of two-step fabrication method for single-mode fiber compatible ion-exchanged glass waveguides*", Applied Optics, Vol. **30**, No 3, pp. 338-343, (1991).

[77]   S. Yliniemi, B. R. West, S. Honkanen, "*Ion-exchanged glass waveguides with low birefringence for a broad range of waveguide widths*", Applied Optics, Vol. **44**, No. 16, pp. 3358-3363, (2005).

[78]   P. Madasamy, B. R. West, M. M. Morrell, D. F. Geraghty, S. Honkanen, N. Peyghambarian, "*Buried ion-exchanged glass waveguides: burial-depth dependence on waveguide width*", Optics Letters, Vol. **28**, No.13, pp. 1132-1134, (2003).

[79]   J. Albert, J. W.Y. Lit, "*Full modelling of field-assisted ion exchange for graded index buried channel optical waveguides*", Applied Optics, Vol. **29**, No. 18, pp. 2798-2804, (1990).

[80]   A. Tervonen, "*Theoretical analysis of ion-exchanged glass waveguides*", in "Introduction *to Glass Integrated Optics*", S. I. Najafi Ed., pp. 73-105, Artech-House, Boston, (1992).

[81]   K. S. Chiang, "*Construction of refractive-index profiles of planar dielectric waveguides from the distribution of effective indexes*", Journal of Lightwave Technology, Vol. **3**, pp. 385-391, (1985).

[82]   G. L. Yip, J. Albert, "*Characterization of planar optical waveguides by K^+-ion exchange in glass*", Optics Letters, Vol. **10**, No. 3, pp. 151-153, (1985).

[83] E. Anemogiannis, E. N. Glytsis, "*Multilayer Waveguides: Efficient Numerical Analysis of General Structures*", Journal of Lightwave Technology, Vol. **10**, pp. 1344-1351, (1992).

[84] S. Honkanen, S. I. Najafi, W. J. Wang, P. Lefebvre, M. J. Li, A. Tervonen, "*Single-mode glass channel waveguides by ion-exchange with ionic masking*", Optics Communications, Vol. **94**, pp.54-58, (1992).

[85] C. Ciminelli, A. D'Orazio, M. De Sario, C. Gerardi, V. Petruzzelli, F. Prudenzano, "*Effect of thermal annealing on the optical characteristics of K^+-Na^+ waveguides*", Applied Optics, Vol. **37**, No. 9, pp. 2346-2356, (1998).

[86] K. O. Hill, Y. Fujii, D. C. Johnson, B. S. Kawasaki, "*Photosensitivity in optical fiber waveguides: Application to reflection filter fabrication*", Applied Physics Letters, Vol. **32**, pp. 647-649, (1978).

[87] G. Meltz, W. W. Morey, W. H. Glenn, "*Formation of Bragg gratings in optical fibers by a transverse holographic method* ", Optics Letters, Vol. **14**, pp. 823-825, (1989).

[88] K. O. Hill, B. Malo, F. Bilodeau, D. C. Johnson, J. Albert, "*Bragg gratings fabricated in monomode photosensitive optical fiber by UV exposure through a phase mask*", Applied Physics Letters, Vol. **62**, pp. 1035-1037, (1993).

[89] S. Mailis, C. Riziotis, I. T. Wellington, P. G. R. Smith, C. B. E. Gawith, R. W. Eason, "*Direct ultraviolet writing of channel waveguides in congruent lithium niobate single crystals*", Optics Letters, Vol. **28**, No. 16, pp. 1433-1435, (2003).

[90] S. Yliniemi, J. Albert, Q. Wang, S. Honkanen, "*UV-exposed Bragg gratings for laser applications in silver-sodium ion-exchanged phosphate glass waveguides*", Optics Express, Vol. **14**, No. 7, pp. 2898-2903, (2006).

[91] H. Hosono, H. Kawazoe, J. Nishii, "*Defect formation in SiO_2:GeO_2 glasses studied by irradiation with excimer laser light*", Physical Review B, pp. R11 921- R11 923, (1996).

[92] L. Dong, J. L. Archambault, L. Reekie, P. S. J. Russell, D. N. Payne, "*Photoinduced absorption change in germanosilicate performs: evidence for the color-center model of photosensitivity*", Applied Optics, Vol. **34**, pp. 3436-3440, (1995).

[93]   B. Malo, J. Albert, F. Bilodeau,T. Kitagawa, D. C. Johnson, K. O. Hill, K. Hattori, Y. Hibino, S. Gujrathi, "*Photosensitivity in phosphorous-doped silica glass and optical waveguides*", Applied Physics Letters, Vol. **65**, pp. 394-396, (1994).

[94]   T. Uchino, M. Takahashi, K. Ichii, T. Yoko, "*Microscopic model of photoinduced and pressare-induced UV spectral changes in germanosilicate glass*", Physical Review B, Vol. **65**, pp. 172202 [1-3], (2002).

[95]   N. F. Borelli, D. C. Allan, R. A. Modavia, "*Direct measurement of 248- and 193-nm excimer-induced densification in silica-germania waveguide blanks*", Journal of Optical Society of America B, Vol. **16**, pp. 1672-1679, (1999).

[96]   A. Othonos, K. Kalli, "*Fiber Bragg Gratings-Fundamentals and Applications in Telecommunications and Sensing*", Artech House, Boston-London, (1999).

[97]   R. Kashyap, "*Fiber Bragg Gratings-Optics and Photonics*", Academic Press, (1999).

[98]   M. Olivero, M. Svalgaard, "*UV-written Integrated Optical 1xN Splitters*", Optics Express, Vol. **14**, No.1, pp. 162-170, (2006).

[99]   H. Hosono, J. Nishii, "*High photosensitivity and nanometer- scale phase separation in GeO_2-SiO_2 glass thin films*", Optics Letters, Vol. **24**, No.19, pp. 1352-1354, (1999).

[100]   M. Cremona, J. A. M. Pereira, S. Pelli, G. C. Righini, "*Optical Waveguides Produced in Li by MeV Ion Beam Bombardment*", Applied Physics Letters, Vol. **81**, pp. 4103-4105, (2002).

[101]   G. C. Bentini, M. Bianconi, M. Chiarini, L. Correra, C. Sada, P. Mazzoldi, N. Argiolas, M. Bazzan, R. Guzzi, "*Effect of low dose high energy O^{3+} implantation on refractive index and linear electro-optic properties in X-cut $LiNbO_3$: Planar optical waveguide formation and characterization*", Journal of Applied Physics, Vol. **92**, No. 11, pp. 6477-6483, (2002).

[102]   V. A. G. Rivera, E. F. Chillcce, E. Rodriguez, C. L. Cesar, L. C. Barbosa, "*Planar waveguides by ion exchange in Er^{3+}-doped tellurite glass*", Journal of Non-Crystalline Solids, Vol. **352**, pp. 363-367, (2006).

[103] P. G. Kik, A. Polman, "*Cooperative up-conversion as the gain-limiting factor in Er doped miniature Al$_2$O$_3$ optical waveguide amplifiers*", Journal of Applied Physics, Vol. **93**, No.9, pp.5008-5012, (2003).

[104] T. Baer, "*Continuous-wave laser oscillation in Nd:Yag sphere*", Optics Letters, Vol. **12**, pp. 386-388, (1986).

[105] Lord Rayleigh "*The problem of the whispering gallery*", Scientific Papers, Cambridge University, (1912).

[106] S. M. Spillane, T. J. Kippenberg, K. J. Vahalla, "*Ultralow threshold Raman laser using a spherical dielectric microcavity*", Nature, Vol. **415**, p. 621, (2002).

[107] A. C. T. Wu, "*Debye scalar potentials for the electromagnetic fields*", Physical Review D, Vol. **34**, No.10, pp. 3109-3110, (1986).

[108] R. Yang, "*Auxiliary Functions in Electromagnetic Theory*", High Education Press, Beijing, (1992).

[109] R. F. Harrington, "*Time-Harmonic Electromagnetic Fields*", McGraw-Hill, New York, (1960).

[110] C. G. Gray, "*Multipole expansions of electromagnetic fields using Debye potentials*", American Journal of Physics, Vol. **46**, pp.169-179, (1978).

[111] M. Born, E. Wolf, "*Principles of Optics*", pp. 633-647, Pergamon Press, 6th Edition.

[112] B. Little, J. P. Laine, H. A. Haus, "*Analytic Theory of Coupling from Tapered Fibers and Half-Blocks into Microsphere Resonators*", Journal of Lightwave Technology, Vol. **17,** No. 4, (1999).

[113] J. R. Buck, H. J. Kimble, "*Optimal sizes of dielectric microspheres for cavity QED with strong coupling*", Physical Review A, Vol. **67**, 033806[1-11], (2003).

[114] C. J. Bouwkamp, H. B. G. Casimir, "*On multiple expansions in the theory of electromagnetic radiation*", Physica, Vol. **20**, p. 539, (1954).

[115] A. Abramowitz, I. A. Stegun, "*Handbook of mathematical functions*", NBS-Washington DC (1972).

[116] R. A. Yadiv, I. D. Singh, "*Normal modes and quality factors of spherical dielectric resonators: I- Shielded dielectric sphere*", Pramana Journal of Physics, Vol. **62**, No.6, pp. 1255-1271, (2004).

[117] I. Teraoka, S. Arnold, F.Vollmer "*Perturbation approach to resonance shifts of whispering-gallery modes ina dielectric microsphere as a probe of a surrounding medium*", J. Opt. Soc. Am. B, Vol. **20**, No.9, 1937-1946 (2003).

[118] X. Peng, F. Song, M. Kuwata-Gonokami, S. Jiang, N. peyghambarian, "*Er^{3+}-doped tellurite glass microsphere laser: optical properties, coupling scheme, and lasing characteristics*", Optical Engineering, Vol. **44**, No.3, 034202 [1-8], (2005).

[119] J. C. Knight, G. Cheung, F. Jacques, T. A. Birks, "*Phase-Matched excitation of whispering-gallery-mode resonances by a fiber taper*", Optics Letters, Vol. **22**, pp. 1129-1131, (1997).

ACKNOWLEDGEMENTS